TECHNISCHE UNIVERSITÄT WIEN

MEDIZINISCHE UNIVERSITÄT WIEN

Diplomarbeit

Design and Dosimetric Validation of an Irradiation Setup for Preclinical Research with X-rays and Protons

zur Erlangung des akademischen Grades

Diplom-Ingenieur

im Rahmen des Studiums

Technische Physik

eingereicht von

Lorenz Langgartner

Matrikelnummer 01426580

ausgeführt am
Atominstitut der Fakultät für Physik
Technische Universität Wien

in Zusammenarbeit mit der
Universitätsklinik für Radioonkologie
Medizinische Universität Wien

Betreuung
Univ.-Prof. Dr. DI Dietmar Georg
Mag. Barbara Knäusl, PhD

Wien, 12.5.2022

Unterschrift Verfasser

Unterschrift Betreuer

Abstract

Cancer poses one of the mayor challenges of modern medicine, with radiation therapy (RT) being one of the most common treatment options. Ion beam therapy (IBT) may be a favourable treatment modality for tumors in close proximity of organs at risk (OARs) and radiosensitive tissue, due to fundamentally different interaction processes as encountered in conventional photon therapy.

Despite a rapidly growing number of IBT centers in recent years, our understanding of the fundamental radiobiological aspects for ion beams still lacks behind compared to conventional RT. Pre-clinical in vivo studies are a key tool to investigate open questions in this field and close the gap from in-vitro cell experiments to clinical implementation. Most commonly small animals, such as mice and rats, are used in pre-clinical irradiation experiments. Irradiation of small animals is however particularly challenging, as it necessitates highest positional and dosimetric accuracy.

The Department of Radiation Oncology of the Medical University of Vienna currently makes efforts to implement the technological basis for image-guided irradiation of small animals with ion beams and X-rays at the MedAustron Ion Therapy Center (MedAustron) (Wiener Neustadt, Austria), a synchrotron-based IBT facility. As the facility was not designed for small animal irradiation, the available infrastructure has to be adapted and supplemented. Furthermore, a dedicated workflow, similar to the one for patient treatment, has to be developed and established for small animals.

The purpose of this work was to contribute to the technological development for pre-clinical in vivo studies at the facility in the future. The first aspect was the design of a beam collimation system for the 200 keV X-ray irradiation unit (YXLON Maxishot, YXLON GmbH, Hamburg, Germany), which will be used for reference irradiation in the future. To overcome the device's limitation of an uncollimated, 120 mm broad beam, a collimation setup was implemented to achieve variable diameters of 1–35 mm, while also providing accurate positioning, adequate beam characteristics and practicality. To investigate relevant beam parameters, dimensions and suitable materials, a prototype was built. Depth doses curves and lateral dose profiles (LDPs) were measured in air for the prototype using a microDiamond detector (PTW-Freiburg, Germany) and Gafchromic^{TM} EBT3 films (Ashland Inc., Wayne, NJ, USA). The encountered limitations of the prototype were taken into account for the construction of the final system, which was manufactured from brass.

The key components of the final collimation system were a $130 \times 130 \times 20\,\mathrm{mm}^3$ primary collimator, combined with a 140 mm long tube, which reduced scatter radiation and served as a mount for interchangeable, 20 mm thick, cylindrical secondary collimators with an outer diameter of 46 mm. Depth dose curves and dose rates in air and water-equivalent material, as well as LDPs were measured for the final setup, using

cylindrical secondary apertures of 5 mm, 10 mm and 15 mm diameter for a first dosimetric assessment with 200 keV X-rays. Dose rates were calculated at depths of 0–100 mm in air and 0–50 mm in water-equivalent material (with an additional 50 mm air gap). At a distance of 50 mm from the secondary collimator, which represents a potential arrangement for pre-clinical experiments, a dose rate of (2.300 ± 0.003) Gy min^{-1} was found using a 15 mm aperture. Hence it was shown, that the setup provides suitable dose rates for irradiation of small animals under anaesthesia. LDPs measured with EBT3 films directly mounted to the secondary collimator showed that no transmission occurs through the secondary collimator, however a transmission of 5 % at a distance of 50 mm from the central beam axis was revealed. The issue regarding transmission calls for further investigation regarding its origin, relevance and potential technical adaptions. Furthermore, LDPs at multiple depths of water-equivalent material were measured to evaluate the field in terms of full width at half maximum (FWHM), flatness and homogeneity index (HI) for multiple secondary apertures. A linear increase of the FWHM of 3.9 %/10mm was found at depths of 0–70 mm for all apertures together with maximum flatness values of 3.3 % at the surface and 5.1 % at a depth of 70 mm. Profiles measured at the surface exhibited increased dose fluctuations within the central region, which was also reflected by the HIs. The highest HI of 1.12 was found for the 5 mm aperture measured at the surface and reduced to 1.08 at 70 mm depth.

The second aspect revolved around the design of a small field dosimetry phantom (SFDP), suitable for beam commissioning and verification measurements in X-ray as well as ion beams. A phantom holding 60 mm × 60 mm slabs of up to 150 mm water-equivalent thickness, including additionally designed holders for the microDiamond detector and Advanced Markus Chamber (PTW-Freiburg, Germany), was developed. The SFDP was constructed using additive manufacturing technology. Dose verification measurements in proton beams were conducted as a proof of concept for the SFDP. Maximum relative deviations of 0.4 % and 1.2 % from the dose predicted by the treatment planning system (TPS) were found in the plateau region of a spread-out Bragg peak (SOBP) for the microDiamond detector and Advanced Markus Chamber, respectively. Thus, it was demonstrated that the SFDP is a viable alternative for commercially available water and water-equivalent phantoms. Additionally, the SFDP offers the possibility of dose measurements on the surface and within the first millimeters, which was previously not possible with the available solutions. Furthermore, the SFDP was used for the experimental setup regarding the final collimation system and proofed equally viable for X-ray beams.

In conclusion, an X-ray collimation system and a small field dosimetry phantom were developed and manufactured. The X-ray collimation system provided suitable field sizes and beam characteristics for the irradiation of small animals. Further investigation regarding transmission through the collimator is necessary. The small field dosimetry phantom was proofed to be a viable option for beam commissioning and verification in X-ray and ion beams.

Kurzfassung

Krebserkrankungen sind eine der zentralen Herausforderungen der modernen Medizin, wobei die Strahlentherapie eine der häufigsten Behandlungsoptionen darstellt. Ionentherapie ist auf Grund fundamental anderer Wechselwirkungsprozesse im Vergleich zur Therapie mit hochenergetischer Photonenstrahlung, eine mögliche vorteilhafte Therapieform für Tumore in der Nähe von Risikoorganen.

Präklinische in-vivo Studien sind ein wichtiges Werkzeug zur Untersuchung der fundamentalen radiobiologischen Aspekte der Ionentherapie und schließen die Lücke von in-vitro Zellexperimenten zur klinischen Anwendung. Meist werden Kleintiere, wie Mäuse und Ratten, in präklinischen Experimenten herangezogen. Die Bestrahlung von Kleintieren geht mit der Notwendigkeit von hoher Genauigkeit bezüglich Positionierung und Dosimetrie einher.

Die Universitätsklinik für Radioonkologie der Medizinischen Universität Wien schafft aktuell die technologische Basis für die bildgeführte Bestrahlung von Kleintieren mit Ionen- und Röntgenstrahlen am Ionentherapiezentrum MedAustron (Wiener Neustadt, Österreich). Da das synchrotron-basierende Zentrum nicht auf die Bestrahlung von Kleintieren ausgelegt wurde, muss die bestehende Infrastruktur entsprechend angepasst und ergänzt werden. Weiters muss ein dedizierter Arbeitsablauf, ähnlich jenem für die Behandlung von Patienten, für Kleintiere entwickelt werden.

Ziel dieser Arbeit war es, Beiträge zur technologischen Basis für die künftige Bestrahlung von Kleintieren im Zuge von präklinischen Studien zu leisten. Der erste Teil fokussierte sich auf die Entwicklung eines Kollimators für jene Röntgenanlage, die künftig für Referenzbestrahlungen verwendet werden soll. Die 200 keV Röntgenanlage liefert einen unkollimierten Strahl von 120 mm Durchmesser und ist somit in dieser Form für die präzise Bestrahlung von Kleintieren ungeeignet. Es wurde ein Kollimatorsystem entwickelt, um den Strahl von den ursprünglichen 120 mm, auf variable Durchmesser zwischen 1–35 mm zu kollimieren. Gleichzeitig sollten präzise Positionierung und angemessene Strahlcharakteristik gewährleistet werden. Um relevante Parameter wie Maße und geeignete Materialien zu untersuchen, wurde ein Prototyp konstruiert. Tiefendosiskurven und Querprofile für diesen Prototypen wurden mit Hilfe eines microDiamond Detektors (PTW-Freiburg, Deutschland) und von Gafchromic^{TM} EBT3 Filmen (Ashland Inc., USA) gemessen. Die dadurch gewonnenen Erkenntnisse wurden in der Entwicklung des finalen Kollimatorsystems berücksichtigt, welches aus Messing gefertigt wurde.

Die Hauptkomponenten des Systems waren ein $130 \times 130 \times 20\,\text{mm}^3$ Primärkollimator und ein 140 mm langes Rohr, das zur Befestigung von auswechselbaren, 20 mm dicken, zylindrischen Sekundärkollimatoren mit 46 mm Durchmesser diente und weiters Streustrahlung reduzierte. Für eine erste dosimetrische Evaluierung des Systems wurden Tiefendosiskurven und Dosisraten in Luft und wasseräquivalenten Material, als

auch Querprofile für sekundär Öffnungen von 5 mm, 10 mm und 15 mm gemessen. Dosisraten wurden in Tiefen von 0–100 mm in Luft und 0–50 mm in wasseräquivalenten Material ermittelt. In einem Aufbau der jenem in künftigen Kleintierbestrahlungen ähnelt, wurde in einer Entfernung von 50 mm vom Sekundärkollimator eine Dosisrate von $(2.300 \pm 0.003)\,\mathrm{Gy\,min^{-1}}$ mit einer 15 mm sekundär Öffnung festgestellt. Somit konnte gezeigt werden, dass das entwickelte System hinreichende Dosisraten für die Bestrahlung von anästhesierten Kleintieren liefert. Querprofile die direkt hinter dem Sekundärkollimator gemessen wurden zeigten, dass es keine Transmission durch den Sekundärkollimator gab. Allerdings wurde eine nennenswerte Transmission von 5 % in einem Abstand von 50 mm von der Strahlachse gefunden. Hinsichtlich der gefundenen Transmission sind weitere Untersuchungen bezüglich der Relevanz, Herkunft und technischer Anpassungen nötig. Weitere Querprofile wurden in verschiedenen Tiefen von wasseräquivalentem Material gemessen, um die Halbwertsbreite (FWHM), flatness und den Homogenitätsindex (HI) des Strahlenfeldes für verschieden Sekundärkollimatoren zu ermitteln. Ein linearer Anstieg der FWHM von 3.9 %/10mm und maximale flatness-Werte von 3.3 % an der Oberfläche und 5.1 % in einer Tiefe von 70 mm wurden für alle untersuchten Sekundärkollimatoren gefunden. Die Querprofile, die an der Oberfläche gemessen wurden, wiesen erhöhte Dosisfluktuationen auf, was sich auch in den HIs widerspiegelte. Der maximale HI wurde für die kleinste Sekundäröffnung von 5 mm mit einem Wert von 1.12 an der Oberfläche gefunden und reduzierte sich zu 1.08 in einer Tiefe von 70 mm.

Der zweite Teil der Arbeit fokussierte sich auf die Entwicklung eines Phantoms für die Dosimetrie in kleinen Feldern, die für die Strahlkommissionierung und -verifizierung in Röntgen- als auch Ionenstrahlen essentiell ist. Es wurde ein Phantom konzipiert und per 3D-Druck gefertigt, das aus 60 mm × 60 mm wasseräquivalenten Platten besteht und Messungen bis zu einer Tiefe von 150 mm ermöglicht. Zusätzlich wurden Halterungen entwickelt, die zur Positionierung eines microDiamond Detektors und einer Advanced Markus Chamber (PTW-Freiburg, Deutschland) in dem Phantom dienen. Messungen zur Dosisverifizierung in Protonenstrahlen wurden durchgeführt, um die Praktikabilität des Phantoms zu zeigen. Maximale Abweichungen zu simulierten Werten von 0.4 % für den microDiamond Detektor und 1.2 % für die Advanced Markus Chamber wurden im Plateau eines spread-out Bragg peak (SOBP) festgestellt. Somit konnte gezeigt werden, dass das entwickelte Phantom eine praktikable Alternative zu kommerziell erhältlichen Wasser- und wasseräquivalenten Phantomen ist. Darüber hinaus bietet das Phantom die Möglichkeit, Messungen an der Oberfläche bzw. innerhalb der ersten Millimeter durchzuführen, was mit den bisher verfügbaren Lösungen nicht möglich war. Zusätzlich wurde das Phantom für Messungen mit dem entwickelten Kollimatorsystem in Röntgenstrahlen verwendet und erwies sich dort ebenfalls als bestens geeignet.

Im Zuge dieser Arbeit wurden ein Kollimator und ein Phantom zur Dosimetrie in kleinen Feldern entwickelt und gefertigt. Das Kollimatorsystem lieferte die für Kleintierbestrahlungen nötigen Feldgrößen und Strahlcharakteristiken. Weitere Untersuchungen hinsichtlich der Transmission durch den Kollimator sind nötig. Das entwickelte Phantom erwies sich als eine geeignete Option für die Strahlkommissionierung und -verifizierung in Röntgen- als auch Ionenstrahlen.

Contents

1. Introduction

1.1. Cancer

Cancer is defined as cells growing in an uncontrolled and abnormal manner. These mutated cells are able to invade nearby tissue or spread to distant parts of the body (metastasis) and thereby negatively interfere with normal function of cells and tissue [1]. As reported by the Institute of Health Metrics (IHME), cancer poses the second leading cause of death in the world, only surpassed by cardiovascular diseases [2, 3]. According to the International Agency for Research on Cancer (IARC) GLOBOCAN cancer statistics, there were 19.3 million new cases of cancer and 10 million deaths from cancer estimated worldwide in 2020. By 2040, an increase in cancer incidence and mortality rates by 56.7 % and 63.7 % respectively are forecast, emphasizing the need for a broad access to cancer treatment as well as the development of novel treatment approaches [4–6].

Radiation therapy (RT) is an indispensable tool in cancer treatment, either alone or in combination with surgery or systemic approaches such as chemotherapy. RT aims at treating cancer with ionizing radiation. High energy radiation is used to irradiate malign cells, causing cell damage and ultimately cell death to stop uncontrolled proliferation of the tumor [7]. It is estimated that 40 % of cancer patients who are cured received RT over the course of their treatment, either alone or as an adjuvant treatment modality [8].

1.2. Radiation Therapy

The first medical application of ionizing radiation was reported shortly after the discovery of X-rays by Röntgen in 1895 [9]. Only six months after Röntgen's discovery, first cancer patients were treated with radiation. Treatment success was however very limited. In the years of 1900-1940, RT employing X-rays rose to be a revolution in oncology, as the fundamental principles that still remain the basis for modern RT were developed. First important milestones were technical advances in X-ray technology (Coolidge tubes) and the introduction of fractionated therapy [10–13]. Further developments were driven by the invention of particle accelerators such as linear accelerators, the cyclotron and the synchrotron and their usage for radiotherapy treatments [14, 15].

The field of RT is divided into two main categories: External Beam Radiotherapy (EBRT) and Brachytherapy. In EBRT, radiation is delivered to the target externally via a beam generated by the treatment machine (e.g. linear accelerator for photons or cyclotron/synchrotron for charged particles), while in Brachytherapy temporary or permanent radiation sources are inserted into or in close proximity to the target [7, 16]. The main objective of all RT approaches is local control and eradication of the tumor,

while maintaining a balance between tumor control and potential side effects caused by exposure of healthy tissue and organs to radiation [17]. Conventional EBRT employs megavoltage photon beams (X-rays) as primary radiation.

The application of accelerated protons (and heavier ions) was first suggested by R. R. Wilson in 1946 [18], as he observed the finite range of protons in matter and recognized the potential of his findings for 'radiological treatment'. In 1958, the first clinical use of accelerated protons was reported by the Lawrence Radiation Laboratory in Berkeley, where patients were treated in a physics laboratory [19]. It took thirty years from then, until the first dedicated medical treatment facilities providing proton beam therapy were constructed at the Clatterbridge Oncology Center in 1989 and at Loma Linda University in 1990. The first facility using carbon ions, HIMAC, was initiated in 1994 in Japan [20]. The number of treatment facilities has steadily increased ever since, with currently over 100 facilities worldwide providing ion beam therapy (IBT) [21].

In principle, therapy modalities employing charged particles (such as protons or carbon ions) offer substantial clinical advantages over conventional photon therapy, due to the fundamentally different interactions of photons and ions with matter (described in more detail in chapter 2). As seen in Figure 1.2.1, photons deposit dose continuously along their path. After an initial build-up, the highest dose deposition is found close to the entrance surface (skin), followed by an exponentially decreasing deposition throughout the tissue. This behavior typically implies that healthy tissue and organs at risk (OARs) proximal and distal to the target volume receive significant levels of dose. Ion beams in contrast show lower dose deposition in the entry region followed by a strongly pronounced maximum (the Bragg peak) and a rapid dose fall-off at the distal end. The depth of the maximum dose deposition is defined by the initial energy of the ion beam, with typical therapeutic energies ranging from 70–250 MeV for protons. By combining multiple beams with different energies, the dose distribution can be modulated such that a target volume shows uniform coverage, while the surrounding tissue is spared. This is referred to as a spread-out Bragg peak (SOBP) and is shown in figure 1.2.1. Thereby therapy modalities employing charged particles are capable of producing highly conformal dose distributions, while minimizing dose to healthy tissue and consequently reducing potential side effects compared to conventional RT [22–24].

Despite the potential physical advantages, adaption of IBT has been slow compared to conventional photon RT. Several reasons may be higher technical difficulty, higher costs and limited availability of necessary infrastructure and the advancement of intensity modulated radiation therapy (IMRT) and image guided radiation therapy (IGRT) in conventional RT [26]. However the number of treatment facilities has rapidly increased in recent years. As reported by the Particle Therapy Co-Operative Group (PTCOG), over 290000 patients have been treated with IBT by the end of 2020 [21].

1.3. Pre-Clinical Research

Even though the number of IBT centers and treated patients is steadily increasing worldwide, there is still a variety of open questions regarding the basic radiobiology and phys-

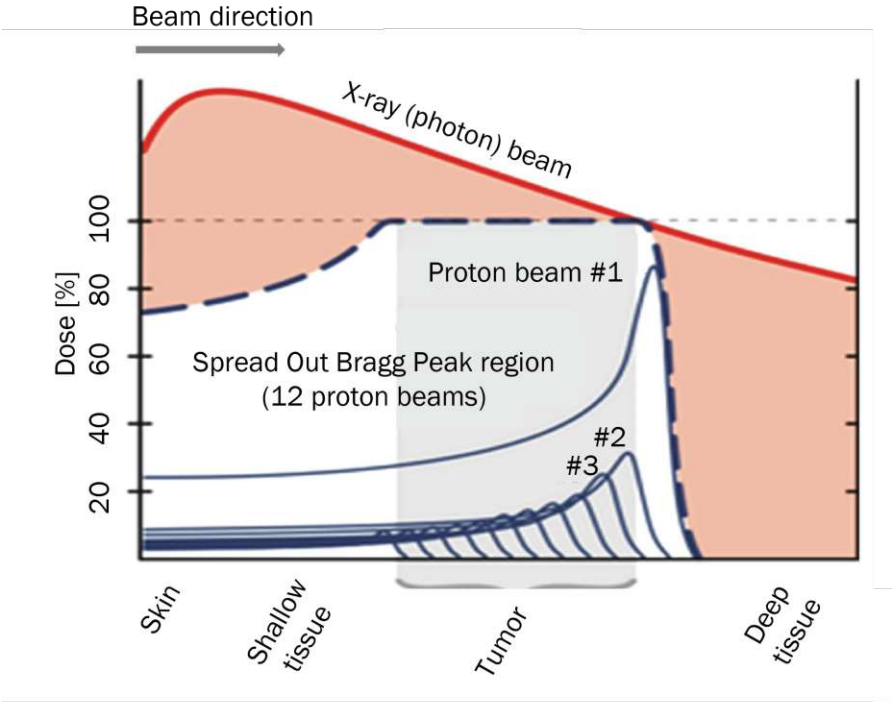

Figure 1.2.1.: Comparison of photon and proton depth dose distribution. Multiple proton beams of different energies can be combined to create an approximately uniform dose distribution within the target (indicated as the grey area), while sparing the surrounding tissue. Figure adapted from [25].

ical effects in IBT [27]. One of the most prominent and extensively discussed open questions is the relative radiobiological effectiveness (RBE) (further described in section 2.2) for protons and heavy charged particles like carbon ions. While for clinical routine purposes, the RBE for protons is assumed to be a constant factor of 1.1, pre-clinical in-vitro and in-vivo studies and first clinical data would suggest a variable RBE, with a pronounced increase at the distal end of the proton range. However, due to a lack of data and considerable variations in the limited available experimental data, clinical facilities still implement a constant RBE for proton therapy. A better understanding of the RBE and its relation to other relevant physical, as well as biological, factors is therefore crucial for the optimization of treatment planning and subsequently beam delivery [28–32].

Among many others, aspects which are still subject of investigations are: fundamental characteristics of cancer as tumor formation and growth, physiological effects as hypoxia, differences in tumor response between photon and proton irradiation, as well as potentially differing interplay for combined treatment modalities such as chemoradiotherapy for IBT [27, 33–35]. Besides an improved understanding of the radiobiological effects, novel techniques and approaches are essential for the advancement of IBT, however they require extensive research and studies before they are suitable for clinical application.

Pre-clinical in-vivo studies have a high potential to improve our knowledge of aspects mentioned above and thereby fuel technological advances. They are an important tool to bridge the gap from in-vitro cell experiments to clinical implementation. Animal experiments and appropriate tumor models have a central role for the development of radiobiology and thereby RT. Most commonly small animals, such as mice and rats, are used for pre-clinical experiments due to their small size, easy handling, low costs compared to other animals and their versatility. Furthermore, there is a variety of immunosuppressed strains and there are methods to transplant human tumor tissue into the animals [33, 36].

Irradiation of small animals is particularly challenging from a medical physics point of view, as it demands accurate dose delivery to tiny structures. Target volumes in the brain for example are downsized approximately by a factor of 10 from humans to mice. This necessitates small beam diameters and high accuracy in the submillimeter range for the alignment of the beam as well as the positioning of the animals [37]. While dedicated image-guided radiation research platforms are available for photons [33, 38], pre-clinical experiments with ion beams are typically still carried out in experimental rooms of clinical facilities, without dedicated beamlines and image-guidance [39]. To yet fulfill the high requirements regarding beam delivery and positioning accuracy, a dedicated workflow, optimally mimicking clinical practice, has to be developed [37].

1.4. MedAustron Center for Ion Beam Therapy and Research

MedAustron Ion Therapy Center (MedAustron) is a facility for proton and carbon ion therapy, which is located in Wiener Neustadt (Austria) and started its operation in 2016. Besides cancer treatment, the facility provides beam time for advanced particle beam research in physics and radiobiological research projects. The core piece of the facility is a synchrotron-based accelerator system, which supplies four irradiation rooms (IRs), one of which is dedicated for non-clinical research purposes. A robotic patient positioning system (Exacure, BEC GmbH, Reutlingen, Germany), in combination with an on-line x-ray based verification system (ImagingRing^{TM}, medPhoton GmbH, Salzburg, Austria) ensures precise positioning for patients as well as experiments in all irradiation rooms [40].

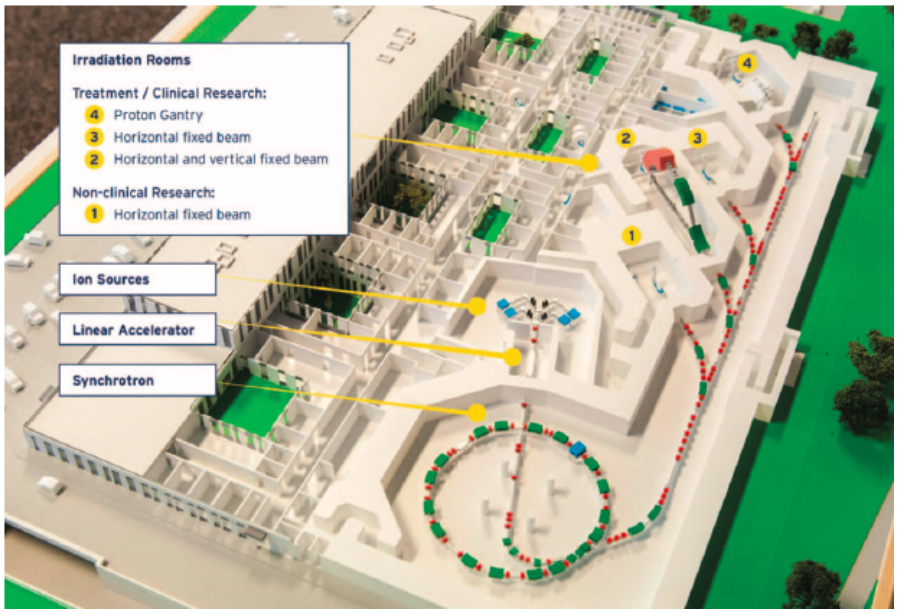

Figure 1.4.1.: Schematic of the MedAustron facility. Ions generated in the ion sources are pre-accelerated in a linear accelerator, before they are injected into the synchrotron. The synchrotron provides beams to the IRs. IR 1 is dedicated for research and is equipped with a horizontal beamline, similar to that of the clinical irradiation room 3. IR 2 features a horizontal as well as vertical beamline. Room 4 is equipped with a proton gantry and is not used for clinical purposes yet. Figure taken from [40].

1.5. Infrastructure for Pre-Clinical Animal Research

In a collaboration of the Medical University of Vienna and the University of Applied Sciences Wiener Neustadt, efforts are currently made to lay the technological basis for future image-guided irradiation of small animals (mice) for pre-clinical in-vivo studies using ion beams. Since the MedAustron facility was originally not designed to enable irradiation of small animals, a dedicated workflow similar to the clinical one has to be developed and established. If possible, available infrastructure and equipment is upgraded and adapted to the requirements of high precision small animal irradiation. Additional equipment, as for example dedicated imaging devices and treatment planning modules, was and will further be acquired. A schematic of the necessary workflow is shown in Figure 1.5.1 and a short overview of the workflow, available infrastructure (and posing challenges) will be given in the following.

- **Imaging:** To asses the anatomy of the animal prior to irradiation for treatment planning, as well as post irradiation for response evaluation, imaging is an important factor in the workflow. Dedicated micro computed tomography (CT), positron emission tomography (PET) and single-photon emission computed to-

mography (SPECT) imaging devices (MOLECUBES, Belgium), as well as a micro magnetic resonance imaging (MRI) device (BioSpec 152/11, Bruker Corporation, USA) were acquired for this purpose. All systems need to be commissioned and imaging sequences suitable for highest resolution images have to be developed.

- **Beam modification:** Small animal irradiation with X-rays, protons and carbon ions shall be established. The modalities employing ions will be conducted in the non-clinical irradiation room, where an additional element to the beam nozzle - the passive beam modifier - was recently developed in order to achieve the necessary small beam diameters using additional collimators. For X-ray irradiation, which will serve as reference irradiation for ion beam studies, an YXLON Maxishot (YXLON GmbH, Hamburg, Germany) cabinet unit (described in further detail in section 3) is available. However the X-ray unit was not designed for high precision irradiation of animals and therefore additional equipment and adaptions, such as an adequate beam collimation system, have to be developed.

- **Mouse positioning:** An irradiation couch dedicated for irradiation of mice was designed and constructed using additive manufacturing technology. The couch provides fixation for the animals and holds the possibility to add cables for anaesthesia, as well as breathing and temperature monitoring. Furthermore the couch is compatible with the above mentioned micro CT scanner, enabling consistent positioning for imaging and irradiation. For the X-ray irradiation unit a positioning table was additionally designed. The table provides adjustable positions with three translational and one rotational degrees of freedom [41].

- **Treatment planning and delivery:** For treatment planning, the treatment planning system (TPS) µ-RayStation (RaySearch Laboratories, Stockholm, Sweden) will be used. Currently µ-RayStation only supports planning for X-ray irradiation, however it will be expanded for protons and ion beams in the future. During the transition phase a research version of the clinical TPS with dedicated features and beam models for small field irradiations will be used for protons and carbon ions. To ensure precise treatment planning and delivery, beam models of the used beamlines have to be commissioned for the TPS. Once established, the beam models need to undergo dosimetric validation and verification to assure agreement between the predicted dose distribution in the TPS and the physically delivered dose during irradiation.

- **Evaluation:** Lastly the effects of irradiation have to be quantified in order to improve our knowledge of the underlying physical and radiobiological effects. Besides imaging, tissue histology will be used to asses tissue response to radiation. To develop qualitative as well as quantitative models of the radiobiological effects, methods to correlate physical parameters as absorbed dose and linear energy transfer (LET) to biological parameters as cell damage will be developed.

Figure 1.5.1.: Schematic of the necessary workflow for small animal irradiation at MedAustron. Figure by courtesy of Peter Kuess, Medical University of Vienna

1.6. Purpose

The goal of this thesis was to contribute to the technological development of the above described workflow for pre-clinical irradiation of small animals. The two main tasks for this work were the development of a collimation system for the X-ray unit used for reference irradiation and the development of a phantom suitable for small field dosimetry in X-ray as well as ion beams. A short summary of the tasks and challenges is given in the following.

Design of an X-ray Collimation System

As described in section 1.4, the available X-ray irradiation unit, shown in figure 3.1.1, is not suitable for high precision irradiation of small animals in its current state. The major limitation of the device is the uncollimated broad beam with a diameter of 120 mm.

Furthermore no devices can be mounted onto the cabinet wall due to radiation protection, since the X-ray source is located directly behind the beam exit window.

Over the course of this thesis, a collimation system providing sufficiently narrow beams for small animal irradiation was designed and experimentally validated. The key requirements for the design were:

- **Collimation** of the initial 120 mm beam opening diameter to variable diameters between 1–35 mm, the typical size of irradiation targets in mice. A mechanism for interchangeable collimator diameters should be integrated.
- **Mounting:** A 'free standing' design was needed, since mounting onto the cabinet wall was not possible due to radiation protection.
- **Positioning:** Submillimeter positioning accuracy was necessary, to provide reliable dose delivery to organs and (sub) structures of the animals.
- **Beam characteristics:** Sufficient dose rates were needed, to ensure reasonable irradiation times of the animals. Irradiation time is a crucial aspect, since the animals are anaesthetized during treatment for immobilisation and necessary anesthetics should be minimized.
- **Practicality:** The handling of the system should be designed as conveniently as possible, since animal handling during irradiation already poses additional challenges by itself.

Before the final setup was designed, a prototype setup was built as a proof of concept and to gain fist insight in beam parameters, suitable material selection and dimensions. Depth dose curves and lateral dose profiles were measured for both setups using a diamond detector, an ionization chamber and radiochromic films.

Design of a Small Field Dosimetry Phantom

The reference material for measurements of absorbed dose in RT is water. Commercially available water and water-equivalent phantoms are typically designed for conventional fields and therefore may proof sub optimal for small field dosimetry due to their size and challenging positioning with the necessary submillimeter accuracy.

As an alternative, a small field dosimetry phantom (SFDP) using water-equivalent slabs was specifically developed for the upcoming rigorous dosimetric measurements during workflow development. The design of the SFDP focused on practicality and precise positioning, while ensuring compatibility with the existing X-ray and ion beam infrastructure. A 3D computer-aided design (CAD) model was created and the SFDP was subsequently constructed using additive manufacturing technology ('3D printing'). It offers the possibility to hold water-equivalent slabs for a depth of up to 150 mm, including additionally developed holders for a diamond detector and ionisation chambers. Furthermore, radiochromic films of sizes up to 60 mm × 60 mm can be inserted between the water-equivalent slabs to measure lateral dose profiles.

In order to proof the usability of the designed SFDP, initial proton and X-ray measurements were conducted. For proton measurements, various detectors were used within the SFDP to measure doses at, or close to the surface to compare their performance in small proton fields. Furthermore, the SFDP played a crucial role for the commissioning measurements within the newly developed collimation system for X-rays, as it enabled straightforward measurements of depth dose curves and lateral dose profiles within the X-ray irradiation unit.

2. Physical and Technological Background

2.1. Ionizing Radiation

Ionizing radiation is defined as radiation carrying sufficient energy to eject electrons from their atomic orbital in an absorbing medium (ionization). Typical ionization energies are in the range of a few eV up to 24.6 eV for helium. Furthermore, ionizing radiation is categorized by its mode of ionization [16, 42]:

- **directly ionizing radiation** consists of charged particles such as protons, electrons or heavy ions, which deposit energy in the absorber directly through Coulomb interactions of the charged particle and orbital electrons of the absorber atoms;
- **indirectly ionizing radiation** consists of electrically neutral particles such as photons or neutrons. Since neutral particles don't participate in Coulomb interactions, ionization is only possible via alternative interaction processes. First a charged particle is released by a conversion process (such as the photoelectric effect for photons or inelastic scattering for neutrons), which then deposits energy in the absorber through direct Coulomb interactions.

The most relevant interaction processes of photons and charged particles with matter will be described in further detail in the following sections.

2.1.1. Interactions of Photons with Matter

Photon interactions are stochastic by nature, they may undergo no or multiple interactions as they pass through matter. Each interaction results in secondary ionizing particles, which may be charged (usually electrons) or uncharged (usually photons). Secondary charged particles deposit their energy close to the interaction site, while secondary photons may travel some distance before interacting. The relative importance of secondary photons strongly depends on the energy of the primary photons. In megavoltage photon beams, as used in EBRT, the main contribution to the absorbed dose is due to primary photons. In the intermediate photon energy range of 50–200 keV, as typically used in pre-clinical research [43–45], a considerable fraction of the absorbed dose may be due to scattered photons [46].

Photons may interact with atomic electrons, nuclei or atoms/molecules as a whole. The probability of interaction with a target in an absorbing medium is typically expressed in

terms of the cross-section per atom σ. Most frequently, the cross-section is expressed in the unit barn:

$$1\,\text{barn} = 10^{-24}\,\text{cm}^2 = 10^{-28}\,\text{m}^2\,.$$

Photon interactions can be categorized into absorption and scattering processes. In absorption processes, the incoming photon loses its entire energy, which is transferred to the target. Secondary particles may be emitted during or subsequent to an absorption. In a scattering process, the incoming photon may change its direction, energy and momentum according to the laws of relativistic kinematics. The main absorption processes relevant[1] for RT and pre-clinical research are photoelectric absorption (pe) and pair production, while the relevant scattering processes are coherent (coh) and incoherent (incoh) scattering. The total interaction cross-section is given by the sum of all individual processes [46]:

$$\sigma = \sigma_{\text{pe}} + \sigma_{\text{pair}} + \sigma_{\text{coh}} + \sigma_{\text{incoh}}\,. \tag{2.1.1}$$

Photoelectric Absorption

As illustrated in Figure 2.1.1, during photoelectric absorption, an incoming photon of energy $h\nu$ interacts with an atom and is absorbed, while an atomic electron is ejected with kinetic energy T. The kinetic energy is given by

$$T = h\nu - E_{\text{B}}\,,$$

where E_{B} denotes the binding energy of the electron.

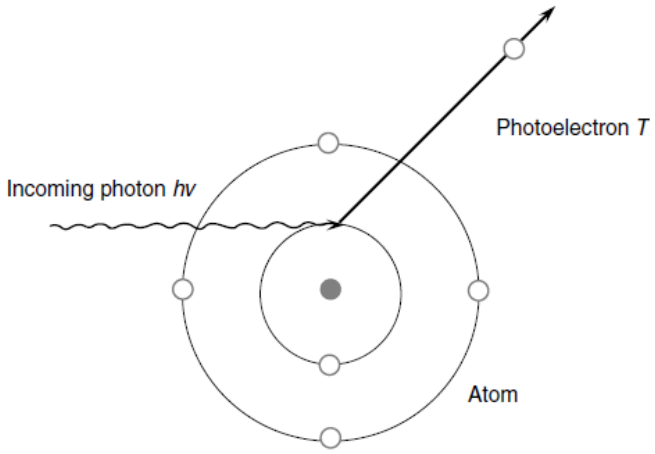

Figure 2.1.1.: An incoming photon with energy $h\nu$ interacts with the atom and ejects a photoelectron with kinetic energy T. Figure taken from [46].

As shown in Figure 2.1.2, the cross section or the photoelectric absorption σ_{pe} displays discontinuities ('absorption edges') at energies corresponding to the binding energies of

[1] Processes as triplet production and the nuclear photoeffect are not described in the scope of this thesis and can be found in literature as [46].

the electron in the atomic shells. At energies below the absorption edge, the photon does not have sufficient energy to eject an electron from the corresponding shell. At energies just above the edge, the photon is able to eject the electron from the shell and therefore the cross-section is increased abruptly, since the number of electrons that can take part in the interaction increases. At energies above the K-edge, the cross section per atom as a function of photon energy and atomic number is proportional to

$$\sigma_{\mathrm{pe}} \propto Z^4/(h\nu)^3\,,$$

showing a strong increase with atomic number Z and a strong suppression with increasing photon energies $h\nu$ [46].

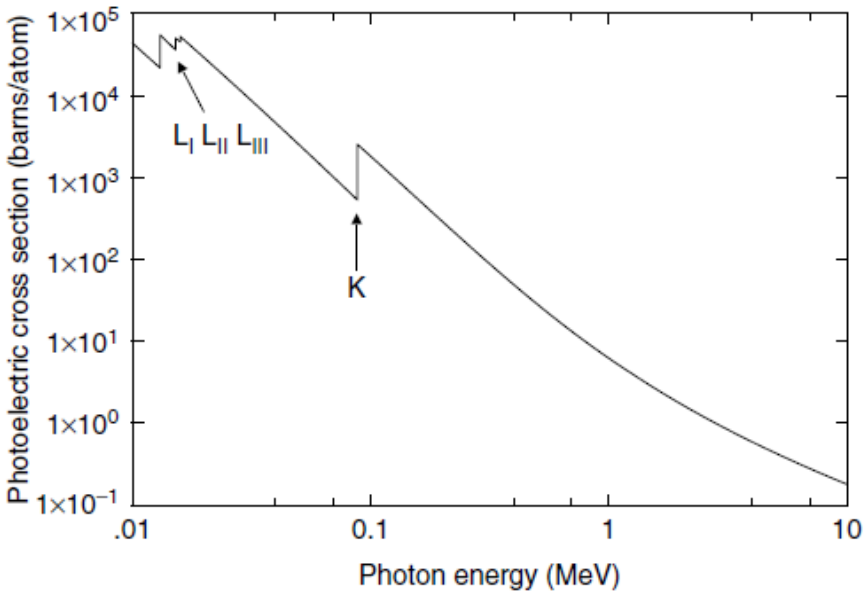

Figure 2.1.2.: The total photoelectric absorption cross-section for lead as a function of photon energy. Figure taken from [46].

As a result of photoelectric absorption, a vacancy is left in the atomic shell. Subsequently, this vacancy is filled by an electron of an outer shell, releasing energy equal to the difference in binding energies of the two involved shells (e.g. $E_{\mathrm{K}} - E_{\mathrm{L}}$ for a transition from the L- to K-shell). There are two competing processes which may carry the released energy:

- Characteristic X-rays describe the emission of photons subsequent to emission of an electron during photoelectric absorption. The released energy (and thereby the energy of the emitted photon) is soley dependent of the involved atomic shells and is thus 'characteristic' for the absorbing atom/material.
- If the released energy is not emitted in form of a photon, but is transferred to another outer shell electron, said electron will be ejected. This is referred to as the

Auger effect. The kinetic energy of the Auger electron is given by the difference of the released energy from photoelectric absorption and the binding energy of the ejected electron [46].

Pair Production

Pair production occurs for photon energies larger than two times the resting energy of an electron (or a positron). If a photon of energy $h\nu > 1022\,\text{keV}$ interacts with an atom, the photon can be converted into an electron-positron-pair via Coulomb interactions in the vicinity of a nucleus. The excess energy of the incident photon is converted into kinetic energy of the electron-positron pair: $E^+_{\text{kin}} + E^-_{\text{kin}} = h\nu - 1022\,\text{keV}$. The electron and positron are emitted in opposite directions and interact with the absorbing material as secondary charged particles, causing further ionizations and excitations. The positron eventually recombines with a free electron into two photons of 511 keV each. The cross-section for pair production above the threshold energy is approximately proportional to the square root of nuclear charge Z [46, 47]:

$$\sigma_{\text{pair}} \propto Z^2\,.$$

Compton (Incoherent) Scattering

Compton scattering describes the interaction of an incoming photon with an atomic electron that is assumed as free and stationary. This assumption holds for photon energies significantly larger than the binding energy of the electron $h\nu >> E_{\text{B}}$. The photon transfers part of its energy to the electron and is scattered with an energy $h\nu'$ through a scatter angle θ. The electron is ejected and the atom thereby ionized. The angle between the scattered photon and ejected electron is denoted as ϕ. The loss in photon energy is typically expresses as a shift in wavelength

$$\Delta\lambda = \lambda_{\text{C}}(1 - \cos\theta)\,,$$

where $\lambda_{\text{C}} = h/(m_e c) = 0.024\,\text{Å}$ is the Compton wavelength with the electron mass m_e. The scattering angle θ and recoil angle ϕ are connected by the relationship

$$\cot\phi = \left(1 + \frac{h\nu}{m_e c^2}\right)\tan\frac{\theta}{2}\,, \tag{2.1.2}$$

revealing that higher incident photon energies result in smaller electron recoil angles ϕ. Furthermore equation 2.1.2 shows that the electron recoil angle ϕ ranges from 0 for photon backscattering ($\theta = \pi$) to $\pi/2$ for photon forward scattering ($\theta = 0$). The cross-section per atom is given by

$$\sigma_{\text{incoh}} = Z\sigma_{\text{KN}}\,, \tag{2.1.3}$$

where σ_{KN} denotes the Klein-Nishina cross-section per electron, which is further described in literature [16, 46].

Rayleigh (Coherent) Scattering

In coherent scattering, a photon is collectively scattered by the atomic electrons (as compared to a single 'free' electron in incoherent scattering). The photon is scattered through the angle θ, while it transfers momentum to the atom and essentially no energy is lost by the photon. The scattering from all electrons is in phase and the angular deflection can be obtained by an interference pattern, which is characteristic for a given atomic number Z of the target. For sufficient energies, the cross-section decreases with increasing energy approximately as

$$\sigma_{\text{coh}} = \frac{Z}{(h\nu)^2} \,. \tag{2.1.4}$$

As coherent scattering is an essentially elastic process, it plays no role in energy transfer, however it contributes to attenuation due to scattering.

Total Cross-Section and Beam Attenuation

As shown in equation 2.1.1, the total atomic cross section is given by the sum of cross-sections of the individual interaction processes. Figure 2.1.3 shows the total and partial atomic cross-sections for carbon, which is relevant for biological media, and lead, which is relevant for irradiation devices and apertures.

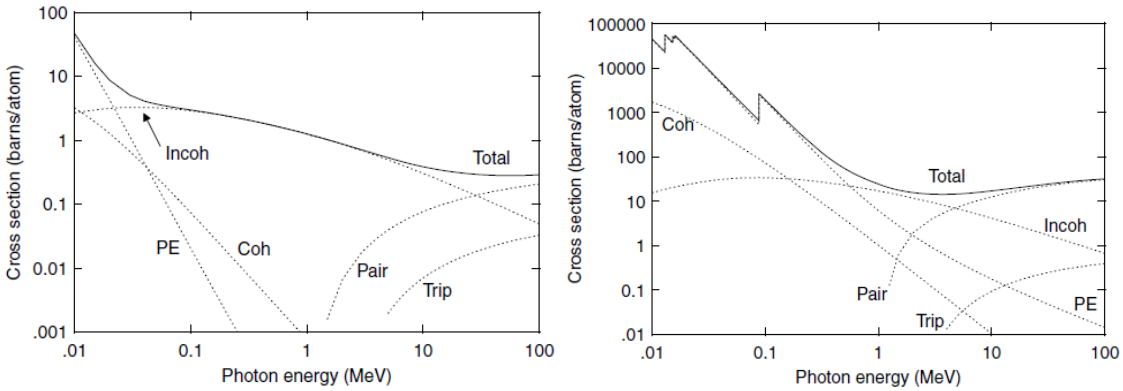

(a) Carbon Z=6 **(b)** Lead Z=82

Figure 2.1.3.: Total and partial cross-sections for carbon (a) and lead (b) for photon energies from 10 keV to 100 MeV. Figure taken from [46].

For both elements, the dominating interaction at low energies ($<$ 50 keV in carbon, $<$ 800 keV in lead) is photoelectric absorption. With increasing energies, incoherent scattering supersedes as dominant interaction. For media with low atomic numbers, such as carbon, incoherent scattering remains dominant over a wide range of energy from approximately 100 keV to 20 MeV. In media with high atomic number, the predominance of incoherent scattering is limited to a smaller range of 800 keV to 5 MeV (in lead), due to stronger dependence to the atomic number of σ_{pair} as compared to σ_{incoh} [46].

The photons of an incoming (monoenergetic) beam may interact in the target medium (causing secondary electrons or scattered photons) or may pass through it without interacting. The probability per unit length for interaction is given by the linear attenuation coefficient, which is related to the total atomic cross-section by

$$\mu = N\sigma_{\text{tot}} = \frac{N_{\text{A}}}{A}\rho\sigma_{\text{tot}}\,, \tag{2.1.5}$$

where N is the number of target entities (e.g. atoms), $N_{\text{A}} = 6.022 \times 10^{23}\,\text{atoms/mol}$ Avogadro's number, A the relative atomic mass of the target and ρ its density [46].

The intensity $I(x)$ of a narrow monoenergetic photon beam, attenuated by a medium of thickness x is thereby given as

$$I(x) = I(0)e^{-\mu x}\,, \tag{2.1.6}$$

where $I(0)$ denotes the intensity of the unattenuated beam. The probability for a photon to interact with an absorber, and therefore the cross-section and linear attenuation coefficient, depends on the energy of the photon $h\nu$ and the atomic number Z. Figure 2.1.4 illustrates the relative predominance of the most important interactions as a function of $h\nu$ and Z [16].

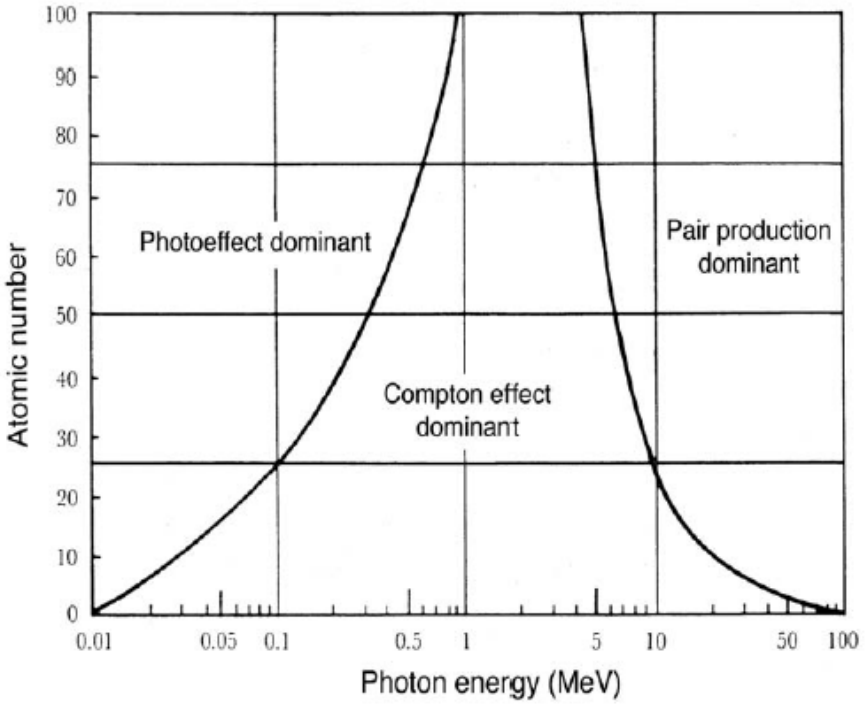

Figure 2.1.4.: Regions of relative predominance of the three main interaction processes for photons in matter. Figure taken from [16].

2.1.2. Interactions of Charged Particles with Matter

A charged particle is surrounded by its electric Coulomb field, which interacts with orbital electrons and nuclei of all atoms it encounters as the particle penetrates into matter. Each individual interaction of the charged particle with the absorber's atoms results in a (small) loss of energy, until the primary particle's energy is spent after a large number of interactions. The parameter used to describe this gradual energy loss along a particles trajectory is the *stopping power*

$$S = S_{\text{col}} + S_{\text{rad}} = -\frac{\mathrm{d}E}{\mathrm{d}x} \quad , \tag{2.1.7}$$

where $\mathrm{d}E$ is the mean energy loss and $\mathrm{d}x$ is the distance. Stopping power is devided into classes: radiation (nuclear) stopping power S_{rad}, resulting from charged particle interaction with the nuclei of the absorber and soft/hard (electronic) collision stopping power S_{col}, which results from interactions with the orbital electrons of the absorber. The classes are typically differentiated depending on the relative size of the impact parameter b and classical atomic radius a (Figure 2.1.5) of the absorber atoms [26, 42]:

- Soft collision ($b >> a$): With an impact parameter b much larger than the radius a of the absorber atom, the charged particle interacts with the entire atomic shell of bound electrons. These interactions may cause atomic polarization, excitation and ionization. In the range of soft collisions, individual energy transfer from the charged particle to bound electrons is small, however the number of such interactions is large, such that approximately 50 % of energy loss is accounted to soft collisions.

- Hard collision ($b \approx a$): When the impact parameter of the charged particles trajectory is of the order of the radius of the absorber atom, the charged particle may interact directly with a single orbital electron and transfer a significant amount of energy via Coulomb processes. The electron may leave the atom (ionization) and successively transfers its kinetic energy to the absorber via collision processes as well. The number of hard collisions experienced by a charged particle is typically small, however the transferred energies are relatively large, resulting in a contribution of approximately 50 % to the total energy loss for ions.

- Radiation collision ($b << a$): When the impact parameter is much smaller than the radius of the absorber atom, the charged particle interacts mainly with the nucleus and may undergo elastic or inelastic scattering. The majority of these interactions are elastic, resulting in scattering of the charged particle and an insignificant loss of kinetic energy. However a small percentage of the interactions are inelastic and result in significant energy loss of the charged particle and the emission of X-rays. This emission of photons is referred to as 'bremsstrahlung'. The probability of this interaction is inversely proportional to the square of mass of the charged particle, which renders bremsstrahlung essentially negligible for charged particles other than electrons.

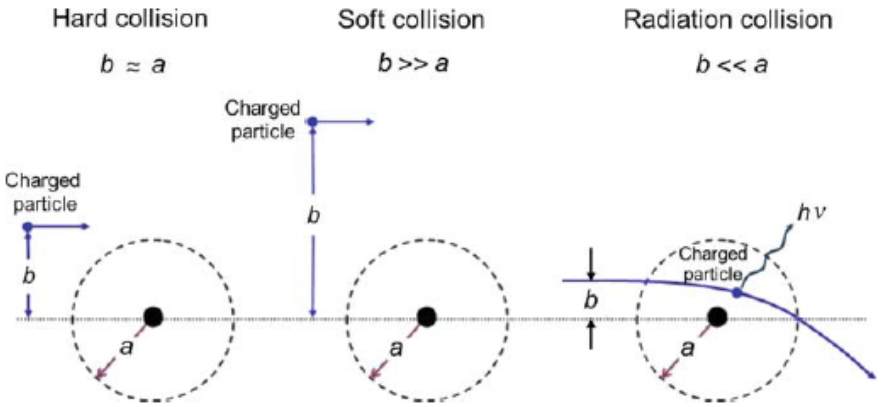

Figure 2.1.5.: Types of collisions of a charged particle with an atom, depending on the size of the impact parameter b and atomic radius a. Figure taken from [42].

The stopping power is frequently expressed in a form that is independent of the mass density of the absorbing material ρ - the mass stopping power defined as

$$\frac{S}{\rho} = -\frac{1}{\rho}\frac{\mathrm{d}E}{\mathrm{d}x}\,. \tag{2.1.8}$$

For light ions, as protons, at clinical energies, the stopping power is predominantly governed by electronic contributions. A first complete theory describing the electronic stopping power is attributed to Bohr [48] and was based on a classical approach, utilizing the impact parameter and assuming the orbital electrons as unbound and stationary collision partners. A more accurate formula describing the electronic stopping power accounting for quantum mechanical effects was developed by Bethe [49] and Bloch [50] and is given by

$$\frac{S_{\mathrm{col}}}{\rho} = -\frac{\mathrm{d}E}{\rho \mathrm{d}x} = 4\pi N_{\mathrm{A}} r_{\mathrm{e}}^2 m_{\mathrm{e}} c^2 \frac{Z}{A}\frac{z^2}{\beta^2}\left[\ln\frac{2m_{\mathrm{e}}c^2\gamma^2\beta^2}{I} - \beta^2 - \frac{\delta}{2} - \frac{C}{Z}\right], \tag{2.1.9}$$

where N_{A} is Avogadro's number, r_{e} is the classical electron radius, m_{e} is the mass of an electron, z is the charge of the projectile, Z is the atomic number of the absorbing material, A is the atomic weight of the absorbing material, c is speed of light, $\beta = v/c$ where v is the velocity of the projectile, $\gamma = \left(1-\beta^2\right)^{-1/2}$ and I is the mean excitation potential of the absorbing material. Equation 2.1.9 also includes two correction terms (Fano correction). $\delta/2$, which represents the density corrections arising from the shielding of remote electrons by close electrons, resulting in a reduction of energy loss at higher energies, and C/Z representing a shell correction, which is important only for low energies where the particle velocity is near the velocity of the atomic electrons. The two correction terms in the Bethe–Bloch equation need to be considered when very high or very low proton energies are used in calculations [26].

Figure 2.1.6 illustrates the qualitative behavior of the collision stopping power in dependence of the kinetic energy of a charged particle. The $1/E_K \propto 1/v^2$ behavior in

the intermediate energy region illustrates the desirable characteristics of ion beams for RT: an ion penetrating matter suffers a continuous loss of kinetic energy, resulting in an increased stopping power, effectively limiting the particles range. The depth dose distribution as a result of this behavior is shown in figure 1.2.1. The depth dose curve for a monoenergetic beam shows low dose deposition in the entrance region, a strongly pronounced maximum - the so called Bragg peak - and essentially no dose beyond this maximum.

If however particles heavier than protons are used, fragmentation of the projectiles can occur, producing fast fragments with a mean velocity similar to that of the primary ion. The fragments have lower mass and therefore higher range than the primary ions and thus generate a 'tail' in the Bragg curve.

IBT exploits the concept of the Bragg peak by modulating a beam (see section 2.4.2), such that the resulting dose distribution is uniform within a target volume and the surrounding tissue is essentially spared.

The collision stopping power obtained in 2.1.9 depends on z^2, the atomic number of the charged particle, implying that, for example, the collision stopping power of an absorbing medium will differ by a factor of 4, comparing protons and alpha particles of same velocities. Furthermore S_{col} shows only weak dependence of the medium specific quantities Z, A and I. The ratio Z/A only varies about 16 %, from biologic relevant elements as carbon and oxygen to high Z elements as lead. The mean excitation potential I shows a diminishing $\ln(1/I)$ contribution. However, a directly proportional relationship of S_{col} to the mass density ρ was found, highlighting that the energy loss in matter most strongly depends on mass density, which can vary by about three orders of magnitude in the human body, from air in the lungs to cortical bone [26, 42, 51].

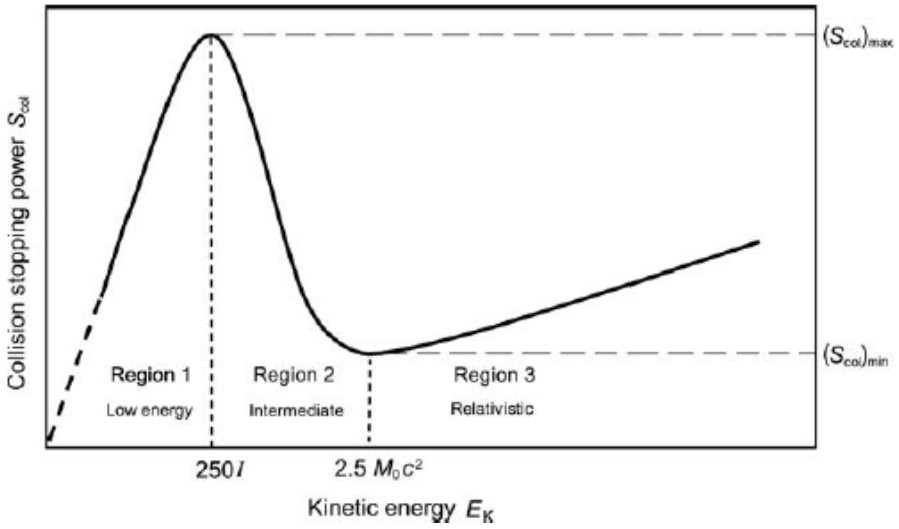

Figure 2.1.6.: Schematic representation of the shape of the collision stopping power S_{col} as a function of the charged particle kinetic energy E_{K}. In the low energy region (1), S_{col} rises almost linearly and reaches a maximum at about $250I$, where I is the mean ionization potential of the absorber. In the intermediate energy region (2), S_{col} decreases as $1/v^2$ or $1/E_{\mathrm{K}}$ where v is the velocity of the charged particle to reach a broad minimum at $\sim 2.5M_0c^2$ where M_0c^2 is the rest energy of the charged particle. In the relativistic region (3), S_{col} rises slowly with increasing E_K because of relativistic effects. Figure taken from [42].

The range R of a charged particle in an absorbing medium is a concept providing the thickness of an absorber the particle can just penetrate. As a charged particle traverses through matter, it loses energy through collisions and scattering, which may result in significant deflections from the original trajectory. These scattering effects are much more pronounced for light charged particles than for heavier particles. Heavy charged particles, as protons, mainly suffer many small angle deflections in elastic collisions, thus their path through an absorbing medium is nearly a straight line (as seen in figure 2.1.7). Light charged particles, as electrons, however may experience large scattering angles and their path is thus tortuous.

Due to the stochastic nature of the underlying interaction processes, there are small variations in the energy loss of individual particles ('straggling'). Hence, the range is an inherently stochastic quantity. Furthermore, range straggling is the reason for the finite width of the Bragg peak. Various definitions of range are in use. The average range $\bar{R}$ is defined as the depth at which half of the particles in the medium have come to rest. A common representation of range is the continuous slowing down approximation (CSDA),

defined as

$$R_{\mathrm{CSDA}}\left(E_0\right) = \int_0^{E_0} \left(\frac{\mathrm{d}E}{\mathrm{d}x}\right)^{-1} \mathrm{d}E = \int_0^{E_0} \frac{\mathrm{d}E}{S(E)}\,, \tag{2.1.10}$$

where E_0 is the initial kinetic energy of the charged particle. For heavy charged particles the R_{CSDA} is a very good approximation of the average range $\bar{R}$, for light charged particles however, the R_{CSDA} can differ up to a factor of 2 by the average range $\bar{R}$ [26, 42].

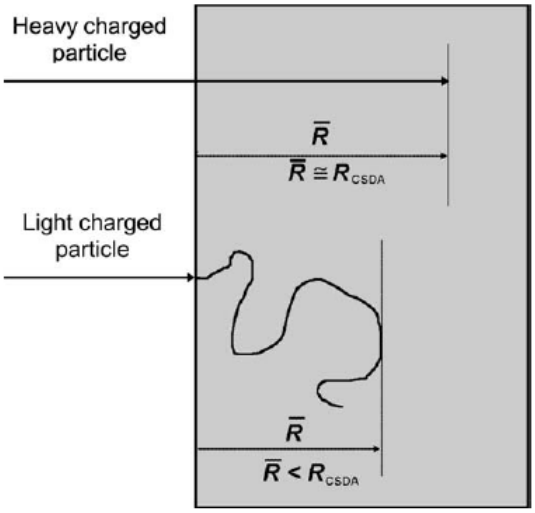

Figure 2.1.7.: Schematic representation of a charged particle penetrating into an absorbing medium. While heavy charged particles can be approximated by a straight path, light charged particles exhibit tortuous paths. Figure taken from [42].

2.2. Quantities

The quantity most commonly used in RT is the absorbed dose D, defined as the mean energy $\bar{\epsilon}$ imparted by ionizing radiation to matter of mass m.

$$D = \frac{\mathrm{d}\bar{\epsilon}}{\mathrm{d}m} \tag{2.2.1}$$

The unit of absorbed dose is the Gray (Gy): $1\,\mathrm{Gy} = 1\,\mathrm{J\,kg^{-1}}$. The imparted energy $\bar{\epsilon}$ takes all energy entering and leaving the volume into account, including any mass-energy conversion (e.g. pair production). As the imparted energy is dependent of the underlying interaction processes, which are highly material dependent, absorbed dose is specific for an absorbing material. Most commonly, in RT, water is established as reference medium [16, 52].

The effectiveness of radiation in terms of a biological endpoint may heavily depend on the 'beam quality'. As charged particles impart energy in tissue, resulting ionization processes may cause a response, such as cell damage. The magnitude of the response

depends on the ionization density, or in other words, whether the energy is imparted 'locally' or over a larger region. A quantity to describe this principle is the LET, which is defined as

$$L_\Delta = \frac{\mathrm{d}E_\Delta}{\mathrm{d}l}\,, \tag{2.2.2}$$

where $\mathrm{d}E_\Delta$ is the mean energy lost by the charged particles due to electronic interactions in traversing a distance $\mathrm{d}l$, subtracted by the total kinetic energy of the secondary charged particles released with kinetic energies larger than Δ. Thus, the LET is often referred to as the 'restricted' stopping power, as it describes the energy locally imparted by charged particles, without considering secondary particles with energies larger than Δ [16, 53].

In clinical practice, the potential difference in biological effect for ions as compared to photons of the same dose is considered by applying a weighting factor, the RBE. The RBE is defined as the ratio of the absorbed doses of a reference radiation (e.g. MV) X-rays) and an ion beam irradiation under otherwise same conditions, that produce the same biological effect or clinical endpoint, i.e.

$$RBE(X) = \frac{D_{\mathrm{reference}}(X)}{D_{\mathrm{ion}}(X)}\,. \tag{2.2.3}$$

The RBE is an implicit function of many physical, biological and treatment parameters, as fractionation, dose rate and beam properties. RBE-weighted doses are reported in terms of the unit Gy(RBE) [28, 54, 55]. Biophysical models were established to parameterize the RBE. Prominent examples are the linear-quadratic model (LQM), microdosimetric-kinetic model (MKM) and local effect model (LEM). An overview of commonly used models is found in [55].

2.3. Dosimetry

It is common practice in dosimetry, to calibrate detectors (e.g. ionization chambers) in standard laboratories under reference conditions and beam quality. As a detector is exposed to radiation, a calibration factor (or function) is used to relate the signal, generated by the detector, to the dose it received. Following the International Atomic Energy Agency (IAEA) TRS 398 protocol [52], the absorbed dose to water D_{w,Q_0} at reference conditions and reference beam quality Q_0 is given by

$$D_{\mathrm{w,Q_0}} = M_{\mathrm{Q_0}} N_{\mathrm{D,w,Q_0}}\,, \tag{2.3.1}$$

where $M_{\mathrm{Q_0}}$is the reading of the dosimeter and $N_{\mathrm{D,w,Q_0}}$ is the calibration factor to convert charge to dose, obtained under reference conditions and reference beam quality Q_0 in terms of absorbed dose to water. However, standard laboratory conditions cannot be easily achieved outside such facilities. Hence, appropriate correction factors must be applied. Typical corrections are related to radiation quality, ambient temperature and pressure and polarity. The absorbed dose $D_{\mathrm{w},Q}$, measured at a non-reference beam quality can thus be expressed as

$$D_{\mathrm{w},Q} = M_Q N_{\mathrm{D,w,Q_0}} k_{Q,\mathrm{Q_0}} \,, \tag{2.3.2}$$

where the factor $k_{Q,\mathrm{Q_0}}$ accounts for differences in beam quality Q from the reference $\mathrm{Q_0}$ and M_Q is the reading corrected for all quantities independent from beam quality

$$M_Q = M'_Q \prod_i k_i \,. \tag{2.3.3}$$

The factors k_i may represent any correction due to conditions differing from the reference and may be determined experimentally, analytically or numerically. A correction factor commonly encountered with air vented ionization chambers k_{TP}, accounts for changes in air density due to differing ambient temperature and pressure is given by

$$k_{TP} = \frac{(273.2 + T)}{(273.2 + \mathrm{T_0})} \frac{\mathrm{P_0}}{P} \,, \tag{2.3.4}$$

where T denotes the temperature [°C] in the sensitive volume, P the atmospheric pressure [hPa], $\mathrm{T_0}$ temperature for calibration (20 °C) and $\mathrm{P_0}$ the atmospheric pressure for calibration (1013.25 hPa).

Since calibration in standard laboratories raises logistic and financial expenses, cross calibration of detectors is a convenient alternative to trace a detector's calibration coefficient back to a standard laboratory. For cross calibration, a detector calibrated in a standard laboratory ('ref') and the uncalibrated detector ('cross') are brought into a radiation field of quality Q consecutively or side by side. As long as it can be guaranteed that both detectors are exposed to the same dose, the calibration factor of the cross calibrated detector follows as [52, 56]

$$N^{\mathrm{cross}}_{\mathrm{D,w},Q} = \frac{M_{\mathrm{ref}}}{M_{\mathrm{cross}}} N^{\mathrm{ref}}_{\mathrm{D,w},Q_0} k_{Q,Q_0} \,. \tag{2.3.5}$$

In the following subsections, an overview of the detector types relevant for this work will be given.

2.3.1. Ionization Chambers

Ionization chambers are widely used in RT for dose determination. Various shapes and sizes are available depending on the requirements, however the basic concept holds for all types. An ionization chamber is essentially a gas (typically air) filled cavity in which an electric field is applied by the electrodes, which are connected to an external voltage, typically provided by an electrometer. Figure 2.3.1a shows a schematic representation of a parallel plate ionization chamber. As radiation passes through the cavity, it may ionize gas molecules. The resulting positive ion and free electron, called an ion pair, are accelerated towards the corresponding electrodes by the applied electric field. The accelerated ion and electron may further ionize the gas as they reach sufficient kinetic energies, before the charges are picked up by the electrodes and measured by the electrometer.

The collected charge is a measure for the absorbed dose, hence ionization chambers are a tool for reference (and absolute) dosimetry if calibrated accordingly [16, 56].

The response of an ionization chamber is mainly characterized by the applied voltage, as shown in figure 2.3.1b. For low voltages, ion pairs may recombine before reaching the electrodes. Ionization chambers used in RT typically operate in the ion chamber ('saturation') region, where ion pairs are collected with near absolute efficiency. In the proportional region, initial ion pairs gain enough kinetic energy to create secondary ionizations, leading to an increased signal. As the voltage is further increased, each ionization event leads to a complete discharge of the chamber due to ionization cascades (Geiger-Mueller region). This yields a strong signal, however proportionality to the initial ionization event caused by radiation is lost, rendering this region unsuitable for absolute dosimetry [56].

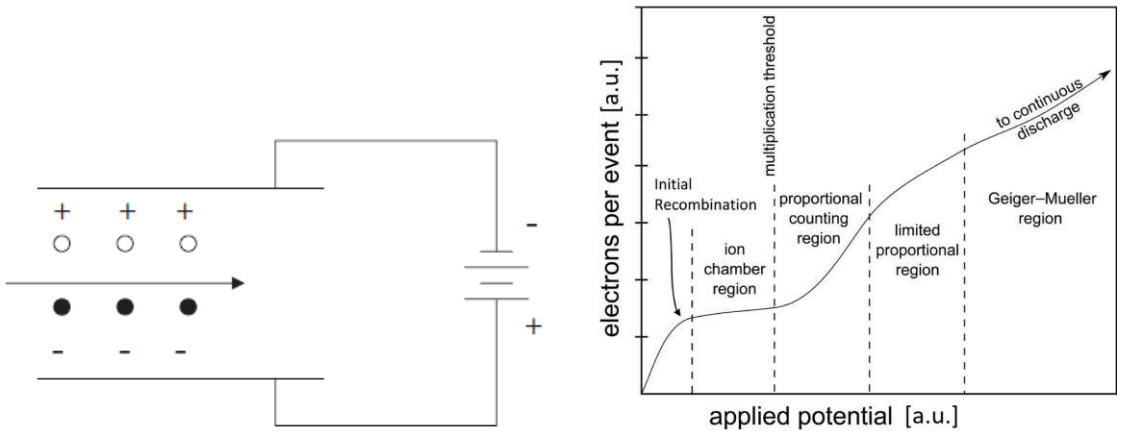

(a) Schematic drawing of a parallel plate ionization chamber. Figure taken from [57].

(b) Qualitative response of ionization chambers. Figure taken from [56].

Figure 2.3.1.: Basic principle of ionization chambers.

2.3.2. Diamond Detectors

Diamond detectors are solid-state detectors. Diamond is an attractive material for dosimetry due to its quasi-equivalence to human soft tissue ($Z = 6$ for diamond and $Z \approx 7.4$ for tissue). Furthermore its sensitivity does not depend on the angle of incidence and energy of radiation. Diamond detectors can be produced with small active volumes, enabling dosimetry with high spatial resolution. The crystal of a diamond has an energy gap of 5.47 eV and resistivity in the range of 10^{13}–$10^{16}\,\Omega\,\mathrm{cm}$, hence it is possible to generate an electric field across the crystal without generating a current by applying an external voltage. As ionizing radiation passes through the crystal, it can create ion pairs. The average energy needed to create an ion pair in diamond is approximately 13 eV. The applied electric field inhibits ion pair recombination and promotes conductivity by accelerating the ion pair towards the corresponding electrode. The crystal is

essentially operated as a resistor, in which the current is proportional to the number of created ion pairs and thereby the received dose rate.

Modern diamond detectors, such as the microDiamond PTW-60019 (PTW, Freiburg, Germany), utilize artificially grown diamonds using chemical vapor deposition (CVD). If layers of doped and intrinsic synthetic diamond are combined with a metallic layer, the diamond can be operated as a Schottky diode. Due to the intrinsic potential of the Schottky diode between the metal contact and layer of diamond, the diamond detector can be operated without an external voltage [56].

2.3.3. Radiochromic Films

Radiochromic films are widely used in RT and preclinical research [58–60]. They provide two-dimensional measurements with high spatial resolution, are near water-equivalent and show small dose rate and energy dependence. The most frequently used model is the GAFchromic^{TM} EBT3 film (Ashland Inc., Bridgewater, NJ).

Radiochromic films contain a special dye (monomere) that is polymerized when exposed to ionizing radiation, resulting in an observable change of color. The film's response to radiation, i.e. the coloration, can be quantified, for example in terms of optical density or absorbance. Radiochromic films can be used to measure absolute dose. The basis for absolute dose measurements is a conversion of the film's response to the dose deposited within a reference medium (usually water), that caused the measured coloration. Films therefore rely on a calibration curve, describing the response of the film for a given dose.

Radiochromic films show negligible energy dependence over a large energy range, however a significant LET dependence is found for for high LET beams as encountered in IBT. In regions of high LET, such as the Bragg peak and especially at the peaks distal end, films show decreased response. This is refered to as LET quenching and renders reference film dosimetry in ion beams particularly challenging, since a dose and LET dependency has to be taken into account [56, 61].

A reference radiochromic film dosimetry system consists of three essential parts: the particular film model used, the scanner used to measure the film's response to radiation and the protocol used for procedures as handling and post-processing of the film [56, 58, 62, 63]. The protocol used over the scope of this thesis and the concept of optical density are described in more detail in section 3.

2.4. Radiation Sources

2.4.1. X-ray Tubes

The basic components of an x-ray tube (illustrated in figure 2.4.1) are a filament and a 'target' within a vacuum tube. A voltage is applied between the filament (serving as cathode) and the target serving as anode. The filament (typically tungsten) is heated by a current, resulting in thermal emission of electrons. The electrons are accelerated away from the cathode, towards the anode by the electric field generated by the voltage. As the electrons are directed onto the target, they interact with the absorbing medium,

resulting in the production of characteristic x-rays and bremsstrahlung (as described in section 2.1.2). The resulting energy spectrum of x-rays is adjustable by the tube current, voltage and optional filters. Higher filament current results in increased heating and thus increased thermal emission of electrons. The current is thereby used to control the fluence of the generated x-rays. The tube voltage defines the maximum kinetic energy the electrons receive as they are accelerated towards the target and hence characterizes the bremsstrahlung spectrum. Furthermore, filters absorbing certain parts of the spectrum can be added to the exit window in order to optimize the beam for a specific application [64, 65].

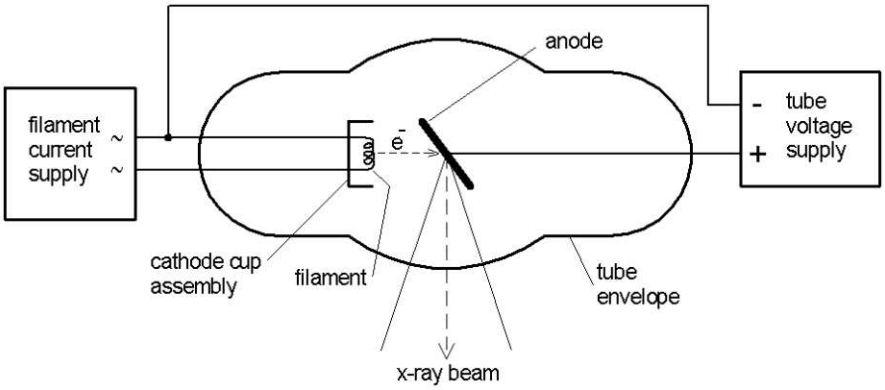

Figure 2.4.1.: Basic components of an x-ray tube. Figure taken from [65].

2.4.2. Synchrotrons in IBT

In a synchrotron, charged particles are accelerated within a closed vacuum chamber loop with a fixed radius. The accelerating (RF) field is provided by resonant cavities placed within the loop. Each time a particle passes a cavity, it gains a small amount of kinetic energy. The particles are forced on a quasi-circular trajectory by dipole (bending) magnets. As the kinetic energy (and momentum) of the particles increases, the magnetic field has to increase synchronously in order to keep the particles within the loop. The maximum kinetic energy the particles may reach is thus limited by the strength of the magnetic field. Typical clinical energies for proton beams are in the range of 70–250 MeV [23]. Quadrupole magnets are used for beam focusing. The particles extracted from a source are typically pre-accelerated by a linear accelerator before they are injected into the synchrotron. The acceleration process in a synchrotron operates within cycles ('spills'), starting with the filling of the ring with particles, acceleration up to the desired energy, extraction of the particles over several seconds and finally followed by ramping down the system to initial conditions before the accelerator is populated again [42, 66–68].

After acceleration to the desired energy and extraction, the charged particles are guided to the beam delivery system in the treatment room, where the beam is modified for the clinical needs. There are multiple approaches on how to deliver the beam to a clinical target, two basic concepts are described in the following [66, 67].

- **Passive scattering**: In passively scattered beams, a monoenergetic beam (typically of a few millimeters width) is scattered and collimated such that the whole target is irradiated at once. To achieve range modulation, absorbers such as rotating range modulator wheels are placed in the beam path, essentially stacking beamlets of different energies. Scatterers are used to spread the beam and achieve a (uniform) lateral dose distribution. Patient specific compensators are then used to confine the beam to the target volume and to spare healthy tissue.

- **Pencil beam scanning** utilizes deflection magnets to continously scan the narrow beam laterally along a 'slice' of the target volume, in a depth that is defined by the beam energy. By reducing the beam energy step wise and repeating the lateral scanning for every slice within the target, a tumor of arbitrary shape can be irradiated.

  By using multiple beams of different energies, depth modulation can be achieved and thus the target volume can be scanned in three dimension. An illustration of pencil beam scanning is shown in figure

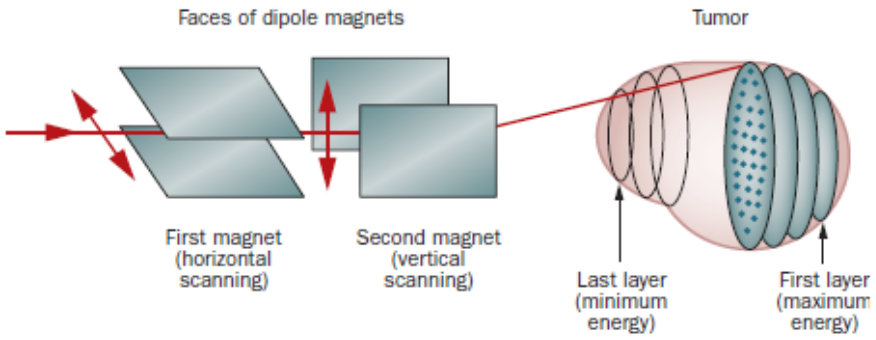

Figure 2.4.2.: Pencil beam scanning of a narrow beam. Lateral position is controlled by deflection magnets and penetration depth is adjusted by variation of the beam's energy. Figure taken from [69].

3. Materials and Methods

3.1. X-ray Unit

The collimation system developed in the framework of this thesis was custom made for the commercially available XYLON Maxishot (YXLON International GmbH, Hamburg, Germany) X-ray cabinet unit, shown in figure 3.1.1. The device is equipped with an oil cooled type Comet Y.TU/320-D03 X-ray tube, providing a horizontal beam. Thus, the geometry of the experimental particle beam line can be mimicked. The target material of the X-ray tube is tungsten, the target angle is 20° and the focus size can be switched between 5.5 mm and 3.0 mm. The accelerating voltage is limited to the range of 15–200 keV, with a maximal tube current of 21 mA. Filtration is provided by 3.0 mm Be, 3.0 mm Al and 0.5 mm Cu filters. This filtration is used to harden the x-ray spectrum (i.e. photons below approx. 30 keV are omitted). Irradiation timer settings are adjustable in increments of 1 s. Voltage, current, time and focus is adjusted via an external control unit. The beam exit window (and uncollimated beam) has a diameter of 120 mm and the device is equipped with rails which are used to mount experimental setups and are height adjustable in increments of 20 mm [44].

All measurements were conducted using a tube voltage of 200 kV, current of 20 mA, focus of 5.5 mm and the above described filtration. These settings provide conditions typical for many pre-clinical experiments [44, 70–72]. The spectrum resulting from the described parameters was calculated using the software SpekCalc (version 1.1) and is shown in figure 3.1.2 [73–75]. The obtained spectrum corresponds to a half value layer (HVL) of 1.14 mm and an effective energy of 84.2 keV in Cu.

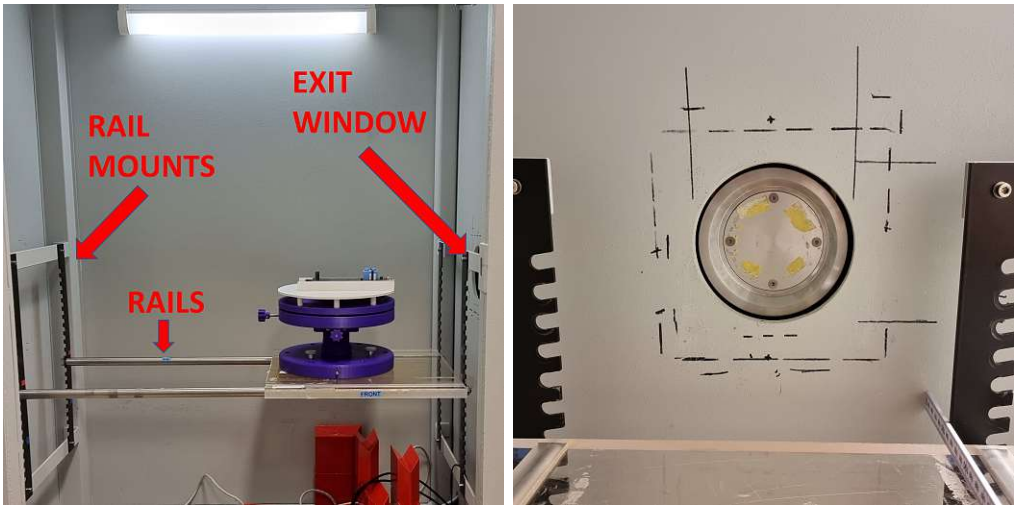

(a) Irradiation cabinet with the mouse positioning table and couch.

(b) Beam exit window with $12\,\mathrm{cm}$ diameter.

Figure 3.1.1.: View into the YXLON Maxishot X-ray unit. The beam exit window is located on the right hand side of the cabinet. A newly developed setup may only be mounted into the cabinet using height adjustable rails.

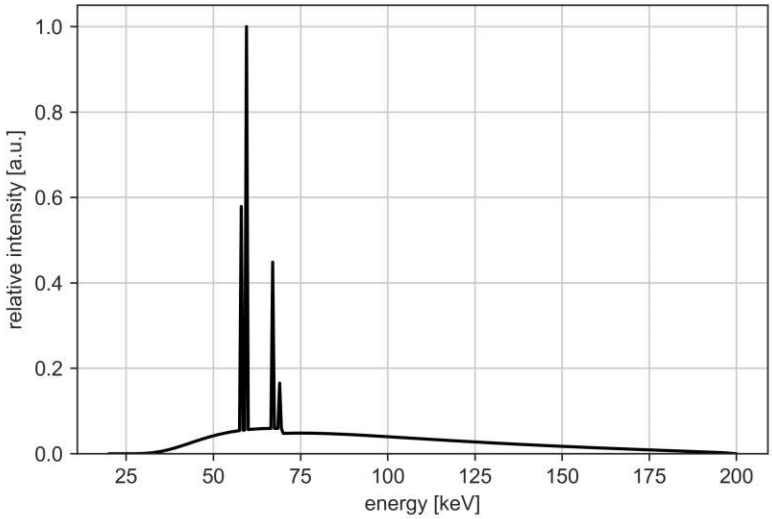

Figure 3.1.2.: Simulated X-ray spectrum for a tungsten target, $20°$ target angle, $200\,\mathrm{keV}$ tube voltage, $20\,\mathrm{mA}$ current and 3.0 mm Be, 3.0 mm Al, 0.5 mm Cu inherent filtration. The peaks are a result of characteristic X-ray transitions, namely KL2 (52.98 keV), KL3 (59.32 keV), KM2+KM3 (66.95 keV and 67.25 keV) and KN2+KN3 (69.03 keV and 69.10 keV) [76]

3.2. Active Detectors

A diamond detector and an ionization chamber were used for reference dosimetry. Doses were acquired in accordance with the IAEA TRS 398 protocol [52], as outlined in section 2.3.

microDiamond Detector

A microDiamond type 60019 detector (PTW-Freiburg, Germany) was used for reference dosimetry in X-ray as well as proton beams. A technical drawing of the detector is shown in figure 3.2.1. Due to its small sensitive volume of 0.004 mm^3, the microDiamond detector is especially suited for small field dosimetry. The cylindrical sensitive volume (1.1 mm radius, 1 µm thickness) is located in 1 mm water equivalent depth (WED). The manufacturer states a temperature dependence of the detector's response of $(0.05 \pm 0.03)\,\%\,K^{-1}$ and temperature correction was thus neglected. The detector was operated at 0 V bias voltage and pre-irradiated with at least 5 Gy before any measurement, as recommended in the user manual [77]. The charge was measured in combination with a PTW UNIDOS^{webline} electrometer.

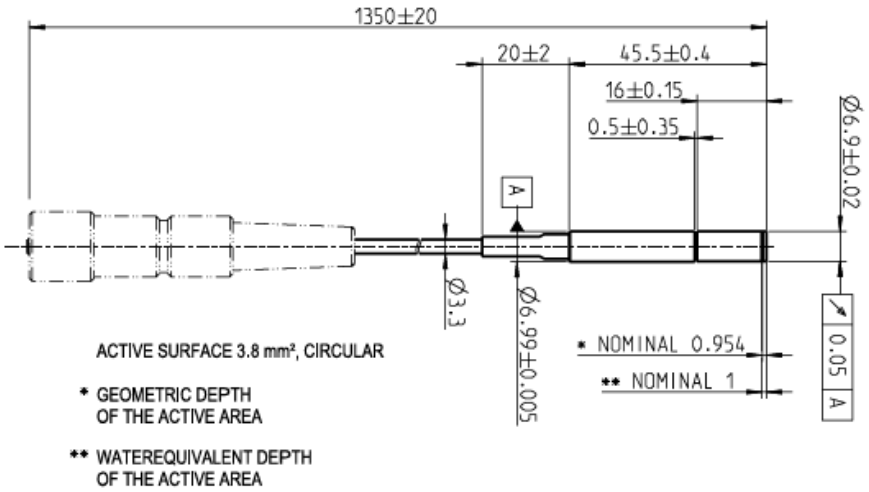

Figure 3.2.1.: Technical drawing of the PTW type 60019 microDiamond detector. Dimensions are given in mm. Figure adapted from [77].

Advanced Markus Chamber

For proton beams, a type 34045 Advanced Markus Chamber (PTW-Freiburg, Germany) was used additionally. The nominal chamber voltage of 300 V was provided by a PTW UNIDOS^{webline}, which was also used for charge measurement. The chamber's dimensions are shown in figure 3.2.2. The sensitive volume of 0.02 cm^3 (2.5 mm radius, 1 mm thickness) is notably larger than that of the microDiamond detector, however the Advanced

Markus Chamber is equipped with a removable protection cap. Without the protection cap, it is possible to measure surface doses, which is not possible with the microDiamond detector. If the protection cap is used, the sensitive volume is located in a WED of 1.3 mm. The chamber is air vented, thus temperature and pressure correction according to equation 2.3.4 is crucial for reference dosimetry. As recommended, the chamber was pre-irradiated with at least 1 Gy [78].

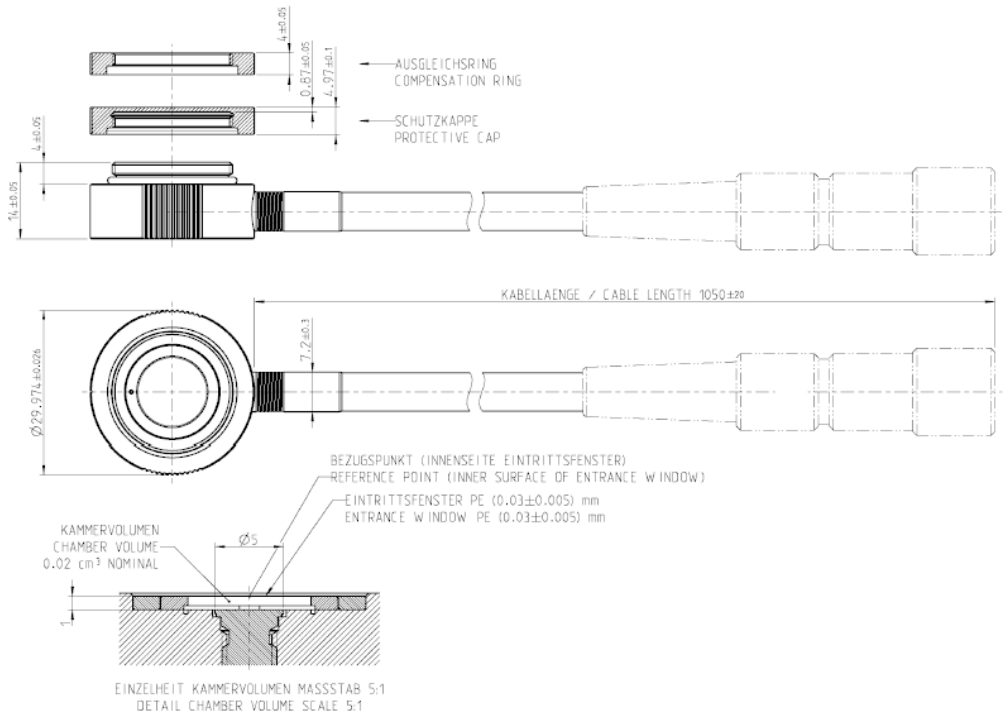

Figure 3.2.2.: Technical drawing of the PTW Advanced Markus chamber type 34045. Dimensions are given in mm. Figure taken from [78].

3.3. EBT3 Radiochromic Films

Gafchromic^{TM} EBT3 films (Ashland, Wayne, NJ, USA), of lot # 03122003, were used for the evaluation of lateral dose profiles and transmission measurements through the collimator setup. EBT3 films consist of a sensitive monomer layer of 28 µm thickness, sandwiched between two symmetric matte polyester layers of 125 µm thickness. When a film is exposed to ionizing radiation, the monomers within the active layer polymerize, resulting in darkening of the film [63]. The report of American Association of Physicists in Medicine (AAPM) Task Group 235 [79] recommends a dose range of 0.01–20 Gy for EBT3 films, while the manufacturer states an optimum dose range of 0.2–10 Gy.

An EBT3 film calibration curve for 200 keV X-rays using the presented X-ray unit was determined in a previous study [80]. Over the course of the previous study, protocols

according to international recommendations [62, 63, 79] were established and maintained and subsequently used for this thesis. The used protocols are outlined in the following.

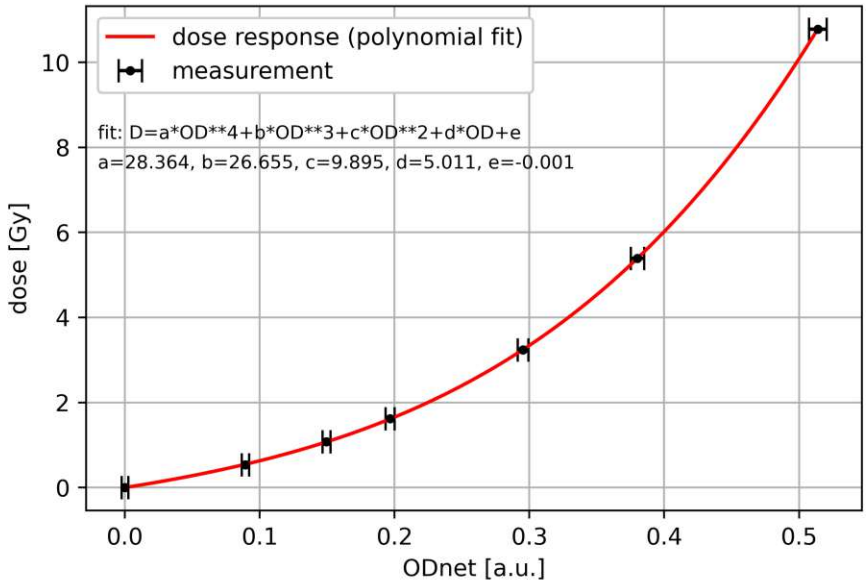

Figure 3.3.1.: EBT3 (lot #: 03122003) calibration curve for 200 keV X-rays. Figure taken from [80].

Scanning Protocol

An Epson Expression 11000XL flatbed scanner (Seiko Epson Corporation, Nagano, Japan) was used for image acquisition. Scanning was performed before irradiation (i.e. background scan) and 24 hours after irradiation. EBT3 films show polarizing characteristics due to the needle-like structure of the polymeres formed after irradiation. Deviations of at least 4 % in optical density were reported between scans in portrait and landscape orientation, therefore scanning orientation was maintained at all times [81]. Consistent portrait orientation (long side of the film parallel to scanning direction) was ensured by marking the films accordingly. Prior to scanning, five scans without films were performed, to account for warm-up effects of the scanner. Film pieces were aligned with the central reference point of the scanner using a template. Scans were acquired using the Epson Scan software in professional mode with all imaging adjustments and color corrections turned off. A resolution of 150 dpi was used and images were saved in 48 bit RGB uncompressed tagged image file format (TIFF).

Data Processing and Analysis

All evaluation was conducted using the Python programming language (version 3.9.7) [82]. The raw signal of the film's response was obtained in terms of pixel values (PVs) from the scanned film. The scanned image consists of three color channels of each 16 bit color depth. For all evaluations, only the red color channel was analyzed [62, 63, 83]. Dose response was evaluated in terms of net optical density (OD_{net}). The optical density OD describes the opacity of a film as

$$OD = \log \frac{I_0}{I}\,, \tag{3.3.1}$$

where I_0 denotes the intensity of incident light and I is the intensity of the light transmitted through the film. For a transmission scan with 16 bit color depth per color channel, the optical density follows as

$$OD = \log \frac{2^{16}}{PV + 1}\,, \tag{3.3.2}$$

where 2^{16} is the maximal pixel value for an image with 16 bit color depth and PV is the pixel value extracted from the image. The change in optical density of a film before (OD_{back}) and after irradiation with a dose D (OD_D) is described by the net optical density

$$OD_{\text{net}}(D) = OD_D - OD_{\text{back}} = \log \frac{PV_{\text{back}}}{PV_D}\,, \tag{3.3.3}$$

and is used to relate the film's response to the received dose D [56, 63].

To enable determination of unknown doses via a measured net optical density (reference dosimetry), a calibration curve has to be established. The calibration taken from [80] was obtained by exposing films to well defined dose levels in the range of 0–11 Gy and subsequent evaluation of the net optical density. The calibration curve was generated by fitting a fourth order polynomial to the dose response curve and is shown in figure 3.3.1.

To characterize dose variations away from the central beam axis, lateral dose profiles (LDPs) were determined by converting the pixel values of a scanned film to absorbed dose with the calibration curve and subsequent evaluation of a line dose through the film's center. Assuming a lateral dose distribution $D(n, m)$, where n and m are discrete values denoting a pixels position, the values of the line dose along n through the center at m_{center} were calculated as

$$L(n) = \frac{1}{W} \sum_{i=-W/2}^{W/2} D(n, m_{\text{center}} + i)\,, \tag{3.3.4}$$

effectively describing $L(n)$ as an average of W values symmetric around m_{center}. W therefore corresponds to the 'width' of the line dose and was chosen as 7 pixels, corresponding to approximately 1 mm at a resolution of 150 dpi.

The flatness F of the resulting LDPs was calculated as a percentage difference of the maxiumum ($D_{\max}$) and minimum ($D_{\min}$) values across the profile within the central

region of the beam.

$$F = \frac{D_{\max} - D_{\min}}{D_{\max} + D_{\min}} \times 100 \tag{3.3.5}$$

The central region region of the field was defined as the inner 80 % of the full width at half maximum (FWHM) [56].

Additionally, the homogeneity index (HI) was computed as a measure of dose fluctuations within the central region. Multiple definitions of the HI are used in RT. For the evaluations in this study, the HI was calculated as

$$HI = \frac{D_5}{D_{95}}, \tag{3.3.6}$$

where D_5 and D_{95} are the minimum dose in 5 % and 95 % of the region of interest (ROI) respectively. The ideal value is 1 and it increases as the dose becomes less homogeneous. To determine D_5 and D_{95}, a cumulative dose volume histogram (DVH) of the region of interest (i.e. the area within a diameter of $0.8 * FWHM$ around the central beam axis) was generated [84].

3.4. 3D Modelling and Additive Manufacturing

Autodesk® Inventor® Professional 2022 (Autodesk Inc., San Rafael, USA) was used for 3D CAD modelling of the developed SFDP and to create technical drawings of the X-ray collimation system. A CAD model of the SFDP was neccessary for additive manufacturing, which was done using a FUNMAT PRO 410 (Intamsys, Shanghai, China) 3D printer. Acrylonitrile butadiene styrene (ABS) was used as printing material.

4. Small Field Dosimetry Phantom

The following chapter describes the design of a small field dosimetry phantom (SFDP) and first dosimetric measurements in proton beams, which served as a proof of concept for the use of the designed phantom for highly accurate dosimetry in small fields.

4.1. Design

The design of the SFDP focused on practicality and accurate positioning in the sub-millimeter region. It should act as a convenient alternative to commercially available water or water-equivalent dosimetry phantoms such as the RW3 Slab Phantom (PTW-Freibug, Germany), which holds 30 cm × 30 cm RW3 ('Goettingen White Water') slabs in thicknesses of 1 mm, 2 mm, 5 mm and 10 mm. In water-equivalent phantoms, water is substituted by solid slabs with a comparable chemical composition. Thereby a similar stopping power as found for water can be achieved, while the handling of solid slabs is typically more straightforward as compared to water phantoms.

Detailed technical drawings are attached in appendix A. The SFDP (figure 4.1.1) can hold 60 mm × 60 mm slabs of up to 160 mm thickness. A holder slab with screw knobs inserted through two 150 mm long slots is used to fix the inserted slabs and to avoid air gaps between the slabs. PTW RW3 slabs of 1 mm and 5 mm thickness were cut into 60 mm × 60 mm pieces such that they can be used within the phantom. Thus, water-equivalent depths ranging from 0–160 mm can be adjusted with increments of 1 mm. Markers, essentially engraved lines, were placed on all sides of the SFDP to indicate the isocenter of the phantom, to support straightforward adjustment with in-room laser alignment systems. Dedicated holders to mount the PTW microDiamond detector and Advanced Markus Chamber in the SFDP were designed and constructed from RW3 material and PMMA. The base of the SFDP was planned analogously to that of the couch designed for the irradiation of mice (described in section 1.5), such that the phantom is compatible with the X-ray positioning table as well. The SFDP was 3D printed from ABS.

Additionally, a pedestal to mount the SFDP on the robotic positioning table for ion beam experiments was designed and 3D printed. The future irradiation of small animals in the experimental ion beam irradiation room will be assisted by image guidance via the onboard X-ray imaging system of the robotic table, therefore geometrical factors regarding the optimal imaging setup were taken into account. Optimal magnification of small structures is reached by a height of 80 mm above the robotic table, hence the height of the pedestal was chosen accordingly.

The SFDP was used for measurements in proton and X-ray beams. The measurements

regarding the newly developed X-ray collimation system are described in section 5.2.2, while the proton measurements are outlined in the following section.

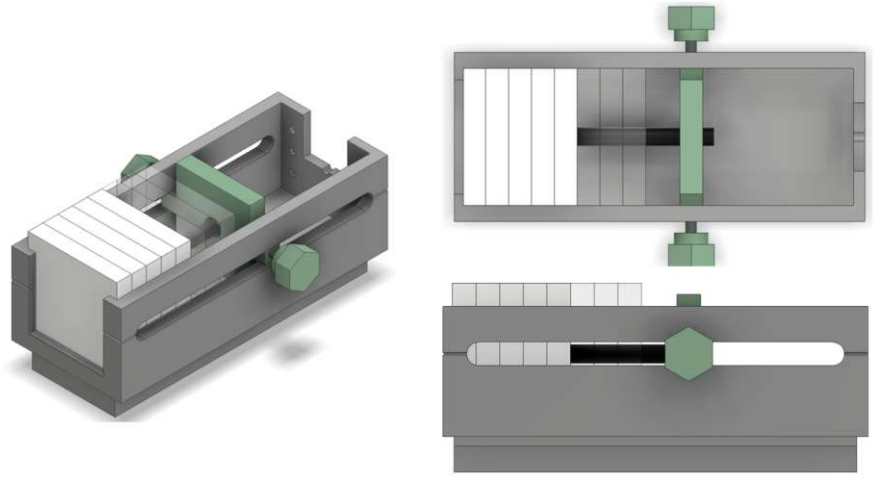

Figure 4.1.1.: Small field dosimetry phantom. RW3 slabs (white) are placed in the phantom (gray). The slabs are fixed by a holder slab (green), such that air gaps between the slabs are avoided. Dedicated holders (transparent) were designed to support measurements with detectors such as the microDiamond detector (black).

4.2. Proton Beam Measurements

All measurements were conducted in the non-clinical irradiation room at the MedAustron facility and served as a proof of concept for the newly developed SFDP. An in-house developed passive beam modifier (PBM) was previously introduced to allow for collimation of the actively scanned proton beam, in order to achieve small field sizes suitable for eye treatment as well as irradiation of small animals. The PBM was mounted directly to the beam nozzle (figure 4.2.1a). For precise positioning, the SFDP was mounted to the dedicated pedestal and placed on the robotic positioning system. A distance of 50 mm between the passive beam modifier's collimator (15 mm aperture opening) and the surface of the SFDP was set. The in-room laser system was used for alignment of the SFDP with the isocenter.

The proton irradiation plan was created in the TPS RayStation 11B (RaySearch Laboratories, Stockholm, Sweden), employing dedicated research features for the irradiation of small fields, namely a dose grid calculation size of 2 mm, an aperture resolution of 5 mm and a lower threshold for active coulomb scattering of 15 MeV. The plan was designed such that a target region of 10 mm width, located in a depth from 20–30 mm in water was covered by a SOBP consisting of 10 energy layers with one collimated proton spot each, resulting in a quasi-homogeneous dose of 0.5 Gy in the target region. Previous

measurements in a water phantom (MP3-P, PTW) at multiple positions in this SOBP originally served for the validation of the beam model for small field irradiations with the PBM. In the frame of this thesis, analogous measurements in RW3 were conducted to demonstrate the suitability of the designed SFDP for such measurements and were therefore compared with the measurements in the water phantom that were performed earlier.

Absorbed doses were measured using both a PTW microDiamond detector and Advanced Markus Chamber, as outlined in section 2.3. The detectors were mounted in the SFDP with the dedicated holders. The depth of measurement was adjusted by inserting RW3 slabs in front of the detector, thereby the depth could be modified in increments of 1 mm. For all measurements, the depth of the sensitive volumes within the detectors had to be taken into account. The sensitive volumes of the microDiamond detector and Advanced Markus Chamber are located in a WED of 1 mm and 1.3 mm, respectively (see section 3.2). Furthermore, the SFDP enabled measurements with no additional material in front of the detectors, which was previously not possible with the available phantoms.

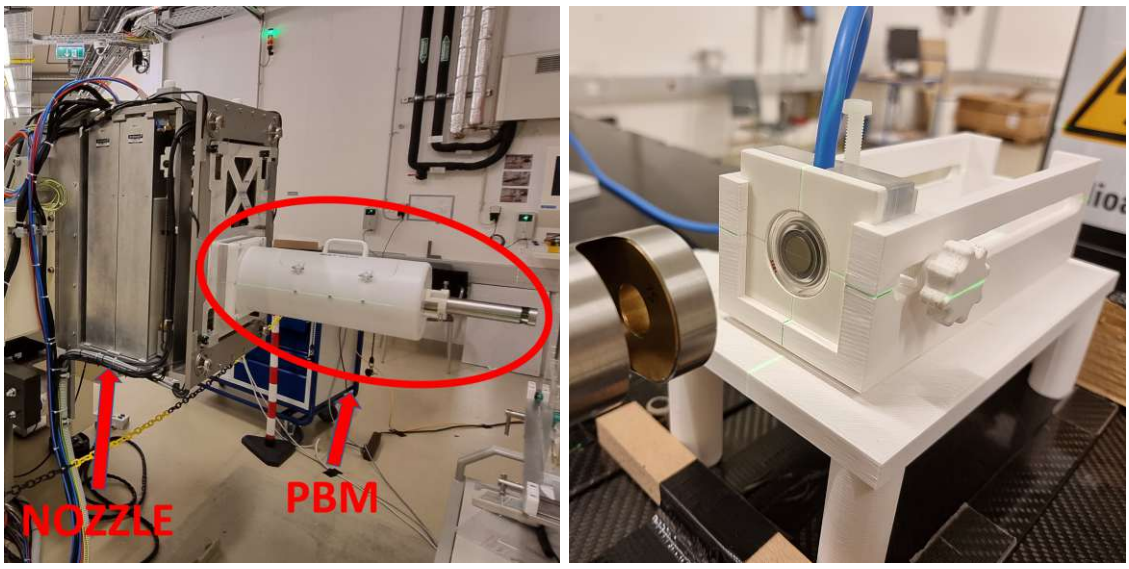

(a) Passive beam modifier

(b) SFDP mounted to the pedestal and equipped with the Advanced Markus Chamber

Figure 4.2.1.: Experimental proton beam measurement setup. A distance of $50\,\mathrm{mm}$ is set between the collimator of the PBM and the phantom's surface. The detectors were mounted within the phantom using the dedicated designed holders.

4.3. Results and Discussion

Figure 4.3.1 shows the results of the proton beam measurements conducted in RW3 using the SFDP and for comparison the dose values predicted by the TPS and data from previous measurements with the microDiamond detector within a water phantom. The doses determined with both detectors in RW3 showed very good agreement with the TPS and the previously measured values in water within the plateau region of the SOBP. The maximal relative deviations from the values predicted by the TPS within the plateau were 0.4 % and 1.2 % for the microDiamond detector and Advanced Markus Chamber respectively. This demonstrated that measurements in RW3 using the SFDP are a suitable and straightforward alternative for the validation of the beam model in water.

Measurements within the first 8 mm were previously not possible due to the entrance window of the water phantom and the effective point of measurement of the detectors, thus the beam model could not be verified in this region so far. The measurements with the SFDP showed relative deviations to the TPS of up to 4.6 % and 5.0 % for the microDiamond detector and Advanced Markus Chamber in this region. This indicates that the established beam model leads to an underestimation of the dose in proximity of the surface, which is especially relevant for future eye treatments, as the lens is particularly radiosensitive. Hence, the beam model may need further tuning.

A measurement with the Advanced Markus Chamber in the distal fall-off region of the SOBP (at a depth of approximately 31 mm) showed a relative deviation from the TPS of 4.6 %. This may be a result of alignment uncertainties and geometric effects. The distal fall-off region exhibits a strong dose gradient, thus small deviations in position may result in significant deviations in terms of the measured dose. Furthermore, the sensitive volume of the Advanced Markus Chamber has a thickness of 1 mm and may be prone to geometric effects when placed in strong gradients.

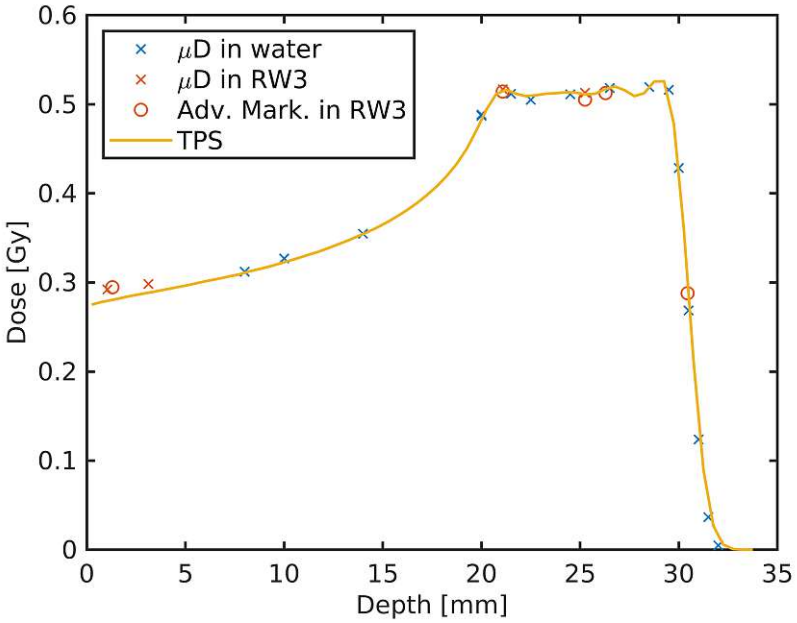

Figure 4.3.1.: Results of proton beam measurements in RW3 compared to the predicted dose by the TPS and previous measurements conducted in water. A microDiamond detector (μD) and Advanced Markus Chamber (Adv. Mark.) were used. Data by courtesy of Andreas Resch, Medical University of Vienna.

5. X-Ray Beam Collimation

The following chapter describes the development of an X-ray collimation system, including a prototype and the final system. Dosimetric measurements with the prototype were conducted and the revealed limitations were considered for the final system. The final system was evaluated dosimetrically.

5.1. Prototype

5.1.1. Design

As outlined in section 1.6, the main requirement for the collimation system for the X-ray unit was a reduction of the beam diameter from 120 mm to variable circular diameters of 1–35 mm and at a later stage also towards other field shapes. To facilitate variable diameters and shapes, a combination of a primary collimator (PC) and interchangeable secondary collimators (SCs) was established. For a practical design, the PC needs to be complemented with a mechanism that can mount the SCs, while guaranteeing fast and straightforward exchange for variable diameters. Similar to commercially available systems [1] as the small animal radiation research platform (SARRP) (Xstrahl Ltd., Camberley, UK), a design with a tube connected to a PC was chosen [60, 85]. The tube would then serve as a mount for the SCs and additionally reduces scatter radiation. In addition to adequate field sizes, a sufficient dose rate to achieve reasonable irradiation times for animal experiments was crucial. An approximate benchmark was a minimum dose rate of $1\,\mathrm{Gy\,min^{-1}}$ at a potential point of irradiation, such that fractionation doses of up to 10 Gy could be provided within approximately 10 minutes. This lower bound for the dose rate ensures that no prolonged anaesthesia of the animals will be necessary.

Suitable lengths of the tube, the diameter of the primary aperture and potential transmission through the collimators were subject of investigation for the design of the prototype. Therefore, an arrangement allowing for interchangeable PCs and adjustable distance between primary and secondary collimator was constructed and is shown in figure 5.1.1. Two 200 mm × 200 mm cast lead collimators of 10 mm thickness, with circular openings of 21 mm and 41 mm were used to evaluate the influence of the opening diameter on the dose rate at distances of 0–84 mm behind the SC. Distances of 50 mm, 100 mm and 150 mm between primary and secondary collimator were investigated. For this purpose a total of six cast steel tubes, with the three respective lengths and outer diameters of 21 mm and 41 mm, matching the openings of the PCs, were used. To enable quick adjustment for different configurations, the tubes were inserted into the opening of

[1] an overview of commercially available systems is found in Tillner et al. [33]

the PC with the corresponding primary opening and fixed with a clamp just before the SC. The inner diameters of the tubes and thus the openings of the primary apertures were 16 mm and 36 mm. The 80 mm × 80 mm secondary brass collimator had a circular opening of 8 mm diameter, a thickness of 10 mm and was used for all measurements in the prototype phase. The SC was not yet mounted using the tubes in the prototype setup, however the tubes were still used in order to mimic the final setup. Both collimators were mounted with steel angles and could be adjusted laterally and vertically by adjustment screws. To assure reproducible positioning of the detector during measurements, an iron 'distancing plate' with holes was placed behind the SC. Smaller plates could be mounted in the desired position using screws and the holder for the detector was placed adjacent to the smaller plates.

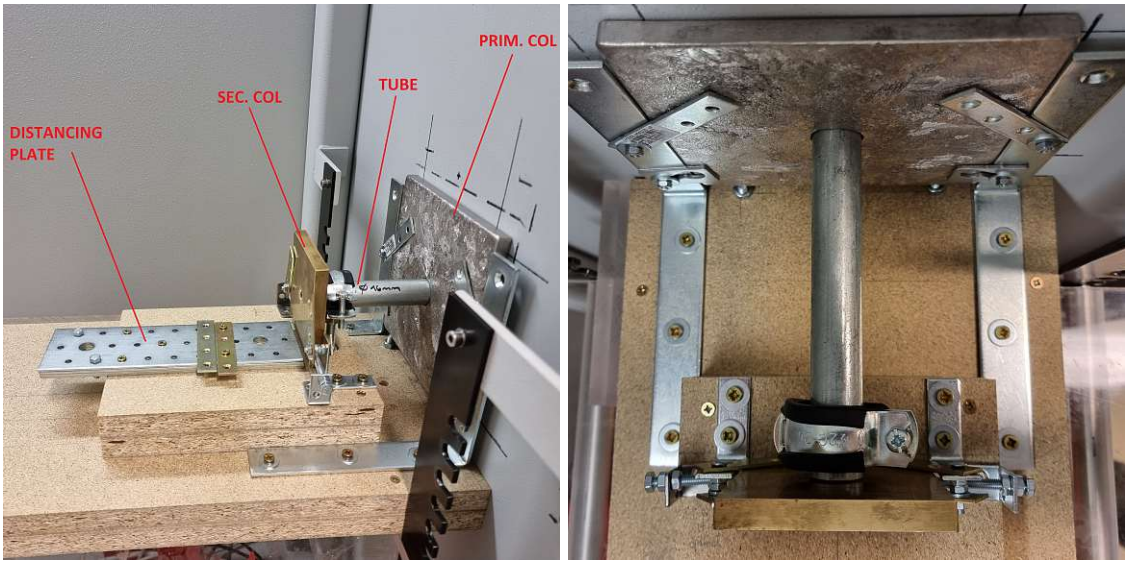

(a) Side view of the prototype setup **(b)** Top view of the prototype setup.

Figure 5.1.1.: The cast steel tubes are inserted into the PCs with openings of ⌀16 mm and ⌀36 mm. The SC from brass is placed adjacent to the far end of the tube. An iron plate was placed behind the SC, to support reproducible distancing of the detector.

5.1.2. Measurements

To evaluate the influence of the distance between the collimators and the diameter of the primary aperture on the dose rate at potential points of irradiation, depth dose profiles (DDPs) were measured in air. The PC was arranged flush with the inner wall of the irradiation cabinet, covering the entire beam exit window. All measurements were conducted using a tube voltage of 200 kV, current of 20 mA and a 5.5 mm focus. DDPs were measured for all six configurations combining the 50 mm, 100 mm and 150 mm tubes and 16 mm and 36 mm PCs. A PTW microDiamond detector (described in section 3.2)

was mounted to an in-house custom made PMMA holder and placed in five distances ranging from 0–84 mm behind the SC (see figure 5.1.2). The PMMA holder was placed on the distancing plate and allowed for consistent positioning. The detector was connected to a PTW UNIDOS$^{\text{webline}}$ electrometer outside of the irradiation cabinet and readout of the measured charge was done manually. Absorbed doses were calculated from the measured charge as outlined in section 2.3. Dose rates $\dot{D}$ were determined from the absorbed dose D and irradiation time t as $\dot{D} = D/t$. To account for variations in output of the X-ray unit, five individual measurements with an irradiation time of 15 s were performed for each distance. The mean value and standard deviation were calculated for each point.

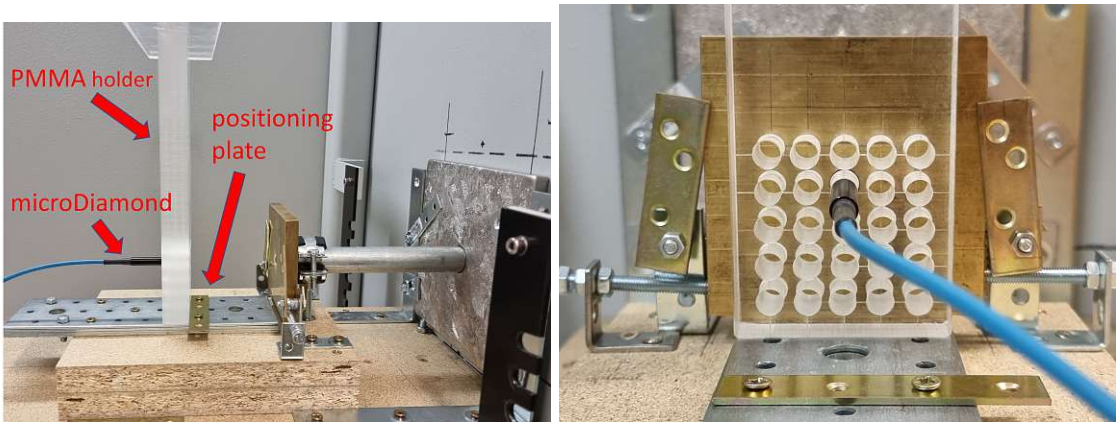

(a) Side view of the experimental setup.

(b) microDiamond detector inserted in the PMMA holder.

Figure 5.1.2.: Experimental setup for measurement of depth dose profiles using a microDiamond detector mounted to a PMMA holder. The PMMA holder was positioned in a reproducible fashion using the distancing plate.

EBT3 films, described in section 3.3, were used to investigate potential transmission through the secondary brass collimator. A 50 mm × 50 mm film piece was placed directly to the SC and irradiated for 120 s in a configuration with a 150 mm tube of 36 mm inner diameter. After irradiation, transmission was visible on the film in an area approximately the size of the primary opening (figure 5.1.3). A lateral dose profile was calculated as described in section 3.3. To calculate the transmission through the collimator, a fit was applied using the Python package LMFIT (version 1.0.3) [86]. A rectangle-like function R describing the peak structure combined with a constant function C to describe the transmission was used and optimized by a least squares method. The following fit function f is given in equation 5.1.1

$$f\left(x; A, \mu, \sigma, C\right) = R + C = A\left[\arctan\left(\frac{x-\mu_1}{\sigma_1}\right) + \arctan\left(-\frac{x-\mu_2}{\sigma_2}\right)\right]/\pi + C\,, \quad (5.1.1)$$

where x denotes the lateral position, A the amplitude of R, μ_1 and μ_2 the positions

where R takes values of $A/2$, σ_1 and σ_2 the characteristic width and C the constant offset caused by the transmission. The transmission T was calculated as the ratio of the minimum and maximum of the fit function, where $\max(f)$ originates from radiation passing through the secondary opening and $\min(f)$ stems from radiation passing through the 10 mm thick brass SC.

$$T = \frac{\min(f)}{\max(f)} \tag{5.1.2}$$

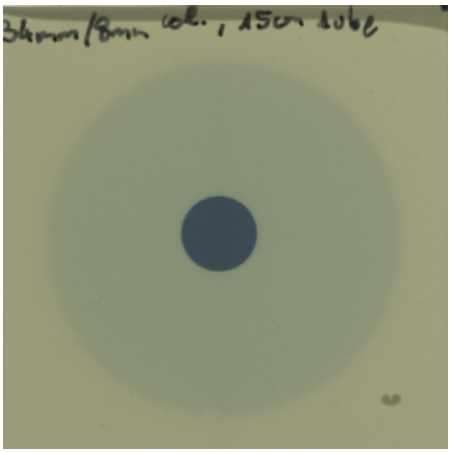

Figure 5.1.3.: EBT3 film taped directly to the SC, to evaluate potential transmission. The central dark spot corresponds to the secondary collimator opening, while the surrounding lighter dark circle shows transmission through the SC. The diameter of the transmission approximately matches that of the primary opening.

5.1.3. Results and Discussion

Figure 5.1.4a and 5.1.4b show the dose rates calculated from the measured DDPs for primary apertures of 16 mm and 36 mm, respectively. Each point corresponds to a mean value of five individual measurements. Relative standard deviations for all points were <0.2 % and are therefore not shown in the figures. The dose rates for primary apertures of 16 mm and 36 mm were in agreement, with slightly increased dose rates for the larger opening, as seen in figure 5.1.5. For the 36 mm primary opening, increased dose rates of up to 5.6 % were found compared to 16 mm. Figure 5.1.5 also demonstrated that the differences are more pronounced for larger distances between the collimators (i.e. lengths of the tubes). The differences were decreasing, as the beams diverged with increasing distances from the SC. No significant influence of the primary opening on the dose rates was found.

As seen in figure 5.1.4, especially figure 5.1.4b, measurements at equal distance from the beam exit window showed slight deviations for different tubes (i.e. distances between the

collimators). This is a result of geometric effects, as different tube lengths are associated with different positions of the SC. For example, a distance of 134 mm from the exit window corresponds to air gaps of 84 mm and 34 mm from the SC for 50 mm and 100 mm tubes, respectively. Due to the larger air gap between the point of measurement and the SC in the 50 mm tube configuration, the beam is more divergent compared to that of the 100 mm tube configuration at this exemplary point, explaining the lower dose rate for the 50 mm tube configuration. Differences may also have been influenced by slight misalignments, as submillimeter positioning accuracy could not be achieved within this setup.

An important implication of the measured dose rates was, that even for the largest distance between the primary and secondary collimator of 150 mm, a dose rate well above 1 Gy min^{-1} was determined, thus small animals can be irradiated without prolonged anaesthesia time even for larger fractionation doses. For a configuration with a 36 mm primary aperture and a 150 mm tube, a dose rate of (2.470 ± 0.003) Gy min^{-1} was measured at a distance of 184 mm from the beam exit window (corresponding to a distance of 34 mm from the SC). The air gap of approximately 30 mm between the SC and detector is representative of a potential arrangement of the SC and the animals in pre-clinical experiments, thus the design of the final collimation system is not limited by the achievable dose rates.

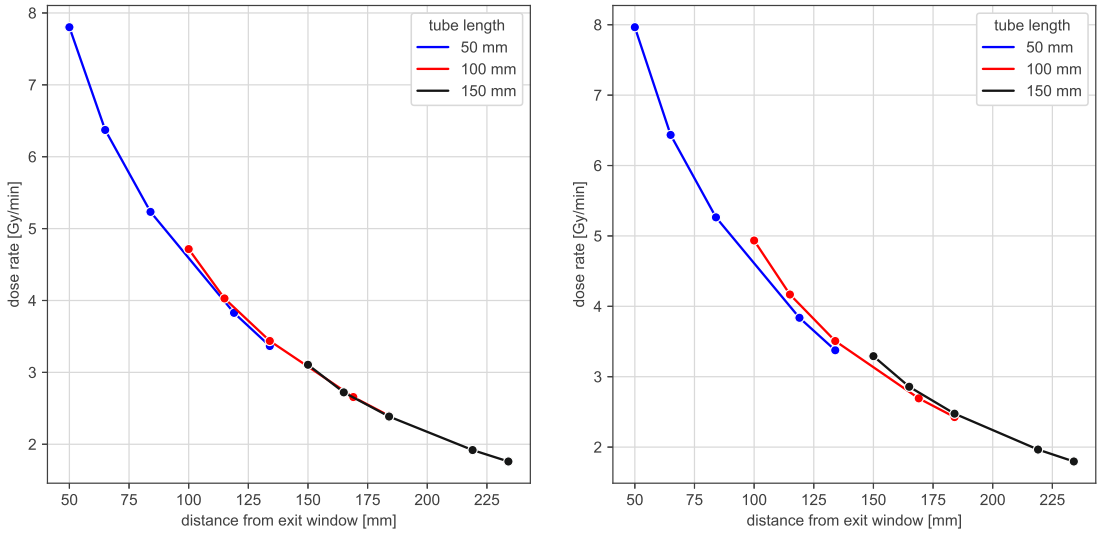

(a) 16 mm primary aperture **(b)** 36 mm primary aperture

Figure 5.1.4.: Dose rates calculated from the DDPs measured in air using different primary apertures.

The lateral dose profile behind the 10 mm thick secondary brass collimator showed a significant transmission of 4.6 % (figure 5.1.6). The transmission decreased rapidly at distances from the central beam axis larger than approximately 18 mm, as in this region

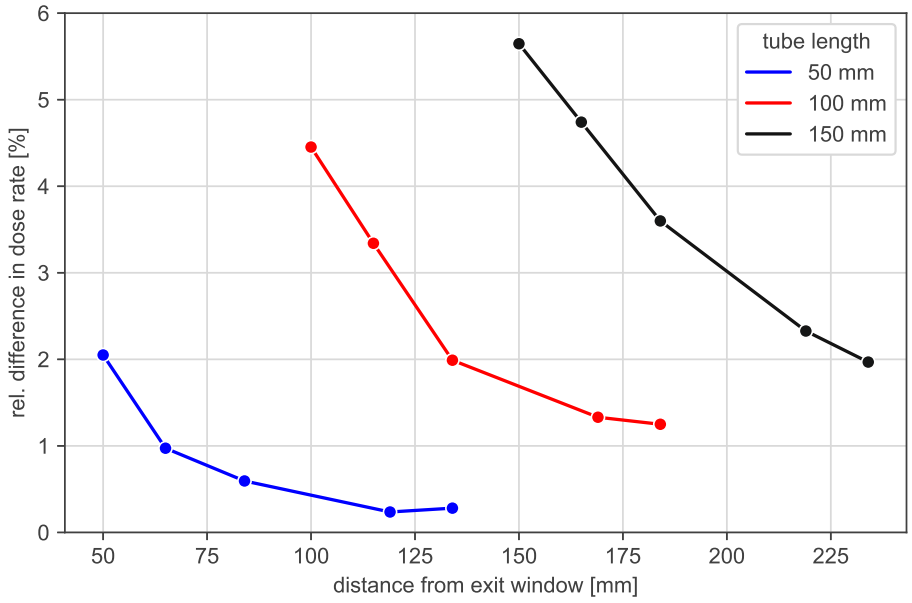

Figure 5.1.5.: Relative difference of dose rates found for primary apertures of 16 mm and 36 mm diameter.

most radiation is absorbed by the PC with a primary aperture of 36 mm diameter. To prevent dose deposition in non target regions in small animal experiments, further adaptations were necessary to reduce the transmission in the final setup, which is described in section 5.2.

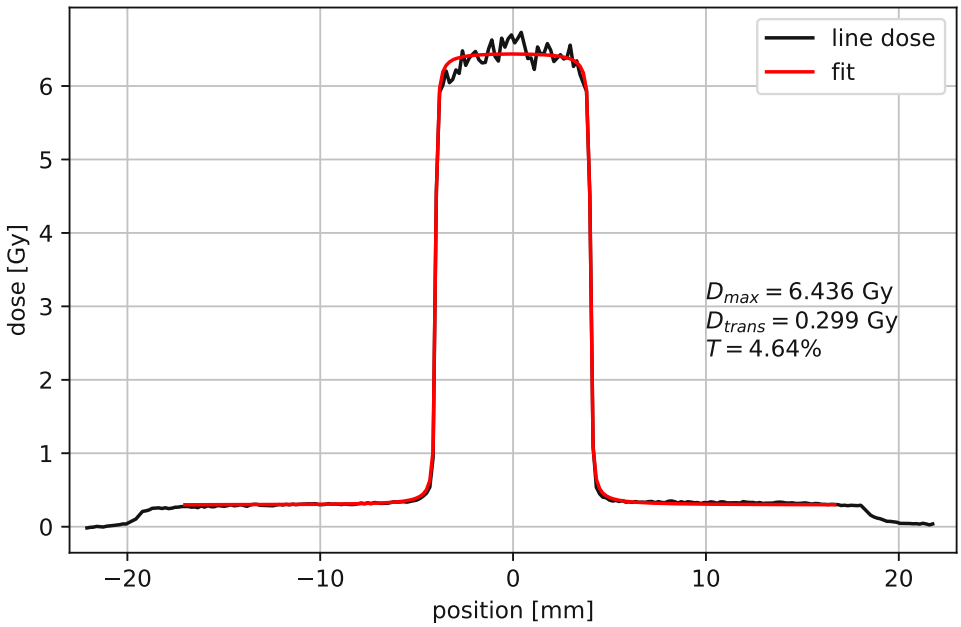

Figure 5.1.6.: LDP showing a transmission of $4.6\,\%$ through the SC in a configuration with a $36\,\mathrm{mm}$ primary aperture and a $150\,\mathrm{mm}$ tube. The evaluated film was irradiated for $120\,\mathrm{s}$.

5.2. Final Collimation System

5.2.1. Design

As motivated in section 5.1, a design combining a PC with a tube to mount variable SCs was chosen. Even though a setup from lead would be beneficial in terms of absorption, the collimation system was manufactured from brass for practical reasons. As compared to lead, brass shows excellent machinability. To guarantee straightforward adjustments and to avoid leakage between the tube and PC, as well as the adjustable SCs, all parts had to be crafted with highest precision, rendering brass the preferred option. Additionally, a setup from brass could be manufactured in house. Furthermore, lead is toxic to humans and can be absorbed through the skin. As the setup would be handled and adjusted frequently, safety precautions would have been necessary, potentially restricting the practicality of the setup during experiments. To account for the transmission found during the measurements regarding the prototype, the primary as well as the secondary collimators were constructed from $20\,\mathrm{mm}$ thick brass plates.

The final setup is shown in figure 5.2.1, technical drawings are attached in appendix B. A $140\,\mathrm{mm}$ long brass tube is attached to the $130\,\mathrm{mm} \times 130\,\mathrm{mm}$ PC. The diameter of the primary aperture is $46\,\mathrm{mm}$. For the first tests, three SCs with circular apertures of $5\,\mathrm{mm}$, $10\,\mathrm{mm}$ and $15\,\mathrm{mm}$ diameter were manufactured. The SC is inserted into the tube from

the front. A circular stopper inside the tube prevents the SC from being inserted further than 20 mm. A screw on top of the tube is used to fix the SC in position and guarantees reproducible positioning, which is especially relevant for potentially asymmetric aperture shapes. The X-ray unit will be equipped with line lasers for precise positioning in the future. To simplify collimator adjustment with the lasers, horizontal markers were engraved at the front end of the tube. To enable hight adjustments, the collimator is mounted vertically using two steel angles of 10 mm thickness. Slots were milled into the steel angles and four internal threads were cut into the PC, such that the system can be fixed in a suitable height using screws.

The entire system is mounted into the X-ray unit using two acrylic glass (Plexiglas®) plates. A 'baseplate' is placed on the height adjustable rails of the X-ray unit and provides space for the irradiation setup and potential additional equipment. The baseplate is equipped with guides, which are fit to the rails, such that accurate and reliable positioning is guaranteed. The collimation system is mounted onto an additional, smaller plate, which can be fixed on the baseplate using screws. Two separate plates were used, as the robust baseplate and the collimation system are notably heavy on their own. Therefore the collimator is mounted on a smaller, lighter plate, such that the entire system can be easily lifted into the X-ray unit and setup step wise by a single person. Additionally, the system is thus more modular and potential adaptions of the collimator or irradiation setup would only require changes of the smaller mounting plate.

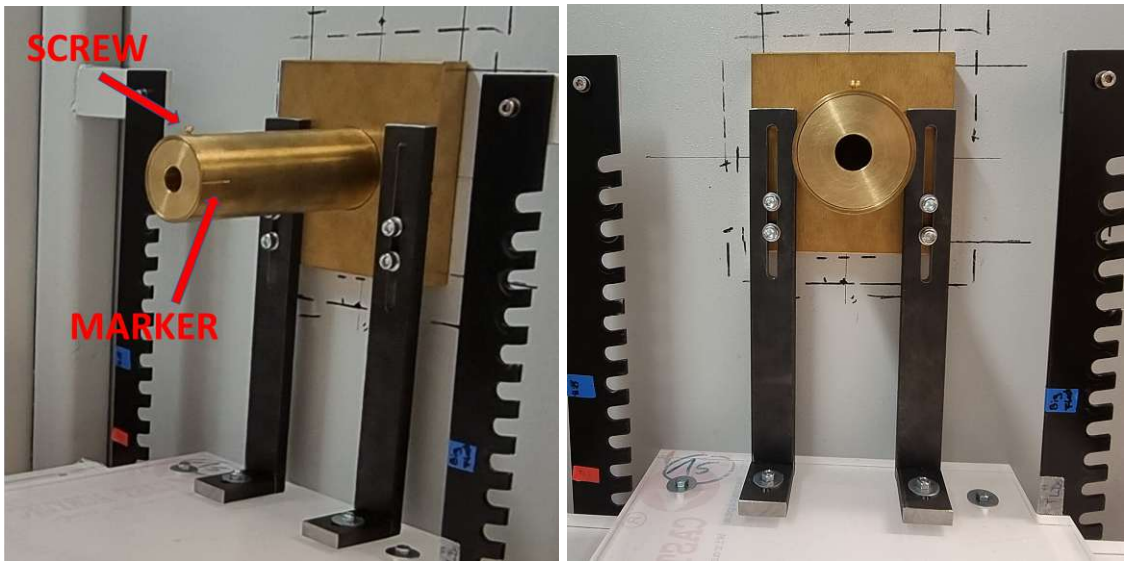

(a) Side view **(b)** Front view

Figure 5.2.1.: The final collimation system mounted into the X-ray unit.

5.2.2. Measurements

First dosimetric evaluation of the collimation setup was conducted. Dose rate, depth dose and beam divergence measurements were carried out using the small field dosimetry phantom (SFDP) in combination with the microDiamond detector and EBT3 films. The SFDP was mounted to the X-ray positioning table (described in section 1.5). The air gap between the SFDP and SC was adjusted by moving the SFDP within the guides of the positioning table. A stripe of millimeter paper was taped to the guides, to simplify accurate positioning. The depth within the SFDP was adjusted by the number of inserted RW3 slabs. All doses measured with the microDiamond detector were calculated as mean values of three equivalent, consecutive measurements. In the following, an overview of the conducted measurements and their corresponding configurations is given.

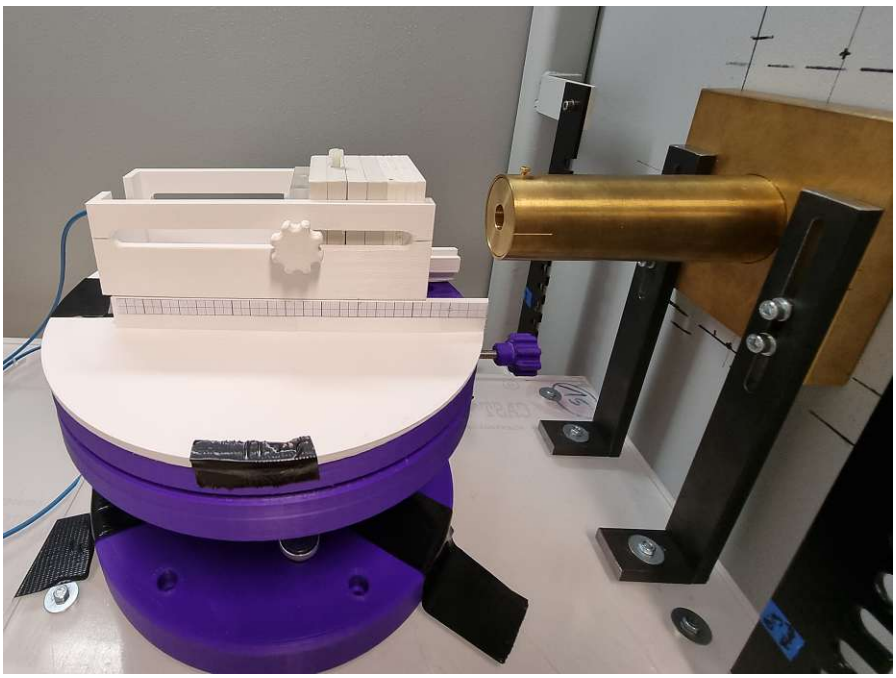

Figure 5.2.2.: Experimental setup for dosimetric evaluation of the collimation system with the SFDP (including the microDiamond detector).

X-ray unit output: The dose animals will be exposed to in pre-clinical experiments will be adjusted via the irradiation time. For short irradiation times, effects regarding beam turn on/off could influence the output dose. To evaluate this effect, dose output was measured for seven irradiation time settings in the range of 5–600 s and compared in terms of dose rate. Each time setting was irradiated three times consecutively and a mean value was calculated. All measurements were carried out within the same configuration. A 15 mm secondary aperture was used. The microDiamond detector was positioned directly behind the SC (no air gap) and no RW3 slabs were placed in front of the detector.

Depth-dose profiles in air were measured to evaluate the dose output with increasing distances in air. DDPs using 5 mm and 15 mm secondary apertures were measured in increments of 10 mm ranging from 0–100 mm. Irradiation times of 30 s were used and no additional RW3 slabs were placed in front of the detector. The corresponding dose rates were calculated from the DDPs and the irradiation time.

Depth-dose profiles in RW3 were measured to assess the dose rates at different depths of water-equivalent material. To mimic a potential configuration for the irradiation of small animals, a 50 mm air gap was used. Doses at depths of RW3 ranging from 0–50 mm were determined in increments of 5 mm for 5 mm and 15 mm secondary apertures. The corresponding dose rates were calculated from the DDP.

Lateral dose profiles: The beam's increasing field size behind the SC was investigated with EBT3 films (figure 5.2.3). For all available secondary apertures, four 60 mm × 60 mm film pieces were placed at depths of 0 mm, 20 mm, 50 mm and 70 mm RW3 and irradiated for 180 s with no air gap. LDPs of the scanned films were generated as described in section 3.3. The FWHM, flatness and HI of the resulting profiles was calculated.

Transmission and leakage: To evaluate potential transmission though the collimation system, two film sheets (200 mm × 250 mm) were mounted to the SC with no absorbing material behind the films and irradiated for 180 s and 600 s, respectively (figure 5.2.4). For film analysis, LDPs were computed and analyzed.

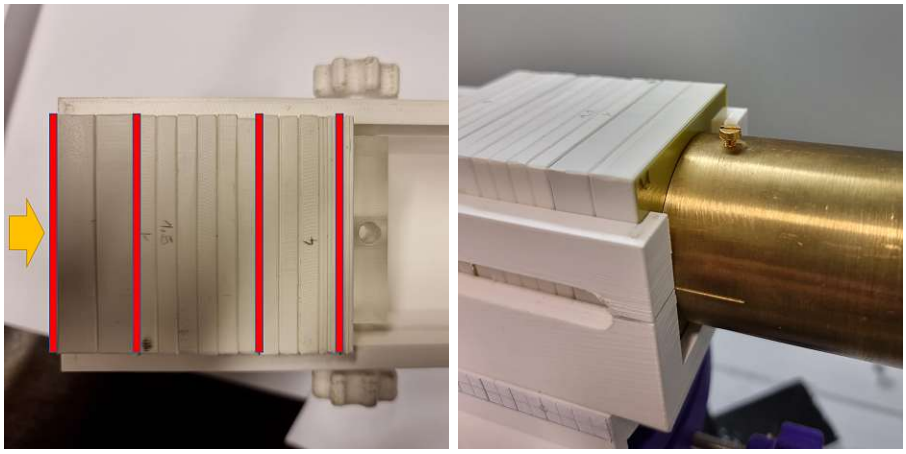

(a) Film position within phantom. **(b)** First film directly behind SC.

Figure 5.2.3.: EBT3 films placed in the SFDP to investigate the beam divergence behind the SC. Films are indicated in red, beam direction in yellow.

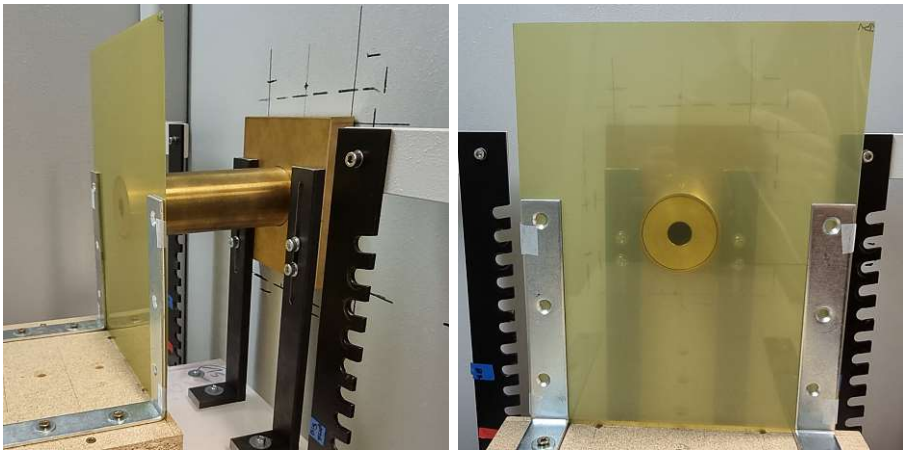

(a) Side view **(b)** Front view

Figure 5.2.4.: EBT3 film setup for measurement of potential transmission and leakage radiation.

5.2.3. Results and Discussion

As shown in figure 5.2.5, the X-ray unit's dose output rises linearly with irradiation time, as could be expected. However, comparing the measured output in terms of dose rate demonstrated higher values for short irradiation times of 5 s and 10 s, as seen in figure 5.2.5b. For 5 s irradiation time, an increased dose rate of 3.5 % was found compared to 600 s. This behavior is notable and requires further investigation, as X-ray tubes typically exhibit a dose build-up rather than a fall-off within the first seconds, as the tube voltage is ramping up to the maximum value. The mean value for irradiation times in the range of 30–600 s was calculated as $(3.349 \pm 0.005)\,\mathrm{Gy\,min^{-1}}$ (0.2 % relative standard deviation). As irradiation of small animals will typically involve doses >1 Gy, deviations in dose rate for short irradiation times are negligible. Thus, expected doses at a point of interest can be linearly estimated by a previously determined dose rate for irradiation times ≥30 s. Should a situation however necessitate irradiation times <30 s, dedicated reference measurements are recommended.

The measured dose rate curves in air (figure 5.2.6a) and RW3 (figure 5.2.7a) both showed elevated dose rates for the 15 mm secondary aperture as compared to the 5 mm. Relative differences in dose rate between the apertures ranged from 9.7–11.5 % in air and 9.9–21.5 % in RW3 and increased with increasing depth, as seen in figure 5.2.6b and 5.2.7b. Once a beam model for the collimation setup is established, verification measurements will be necessary to confirm that the TPS is able to correctly predict the required irradiation times depending on the dose rate as well as the different aperture geometries.

The LDPs shown in figure 5.2.8 were used to determine the increasing field size with increasing penetration depth in RW3. The resulting FWHMs are presented in 5.2.8d and show a linear relationship between field size and penetration depth. Slopes of 0.02, 0.04

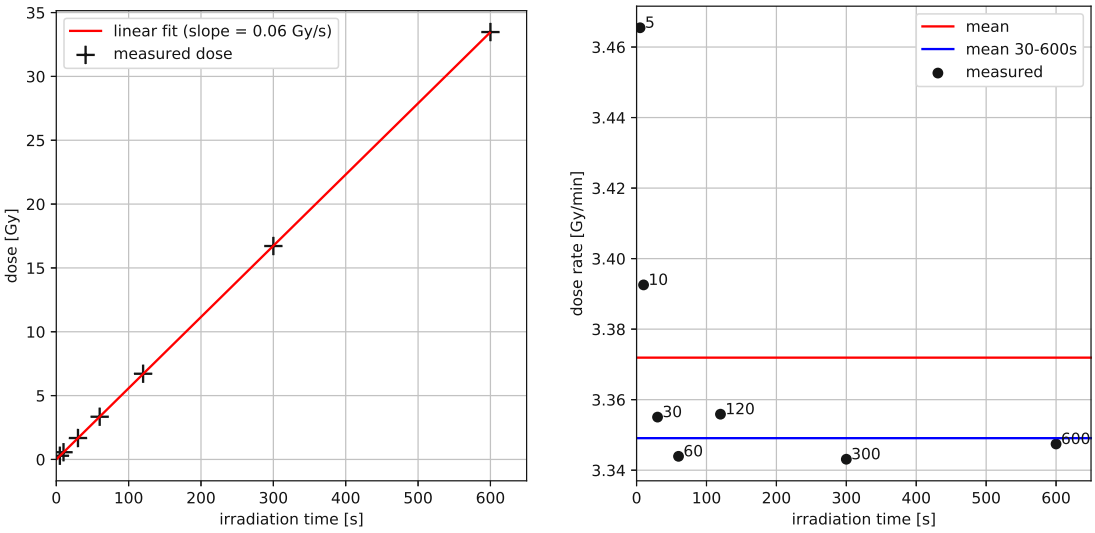

(a) Absolute dose **(b)** Dose rate

Figure 5.2.5.: Dose output for irradiation times of $5\,\mathrm{s}$, $10\,\mathrm{s}$, $30\,\mathrm{s}$, $60\,\mathrm{s}$, $130\,\mathrm{s}$, $300\,\mathrm{s}$ and $600\,\mathrm{s}$ directly behind a $15\,\mathrm{mm}$ SC. Relative standard deviations for all measurements were $<0.25\,\%$.

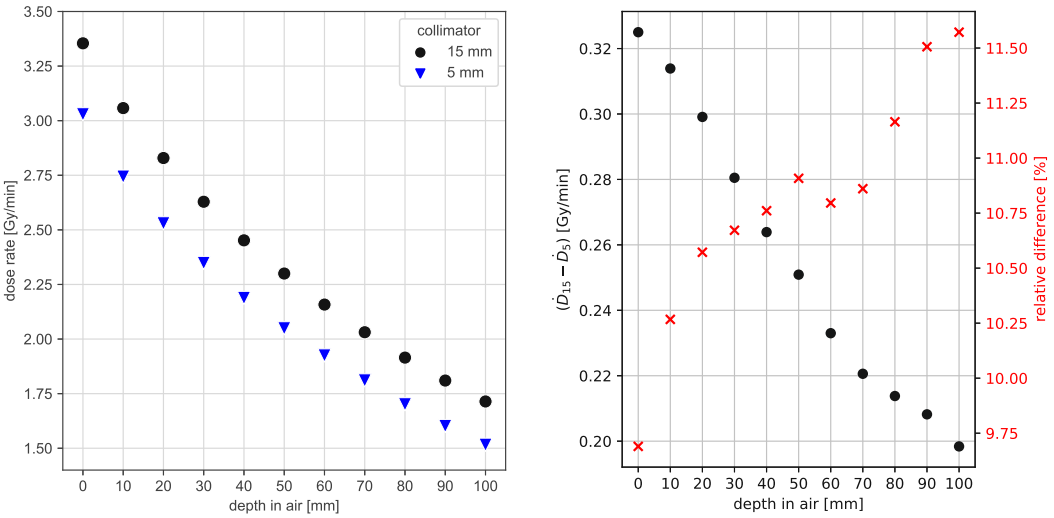

(a) dose rates **(b)** differences between apertures

Figure 5.2.6.: Dose rates measured in air using $5\,\mathrm{mm}$ and $15\,\mathrm{mm}$ secondary apertures (a) and differences between the secondary apertures (b). Relative standard deviations were $\leq 0.15\,\%$.

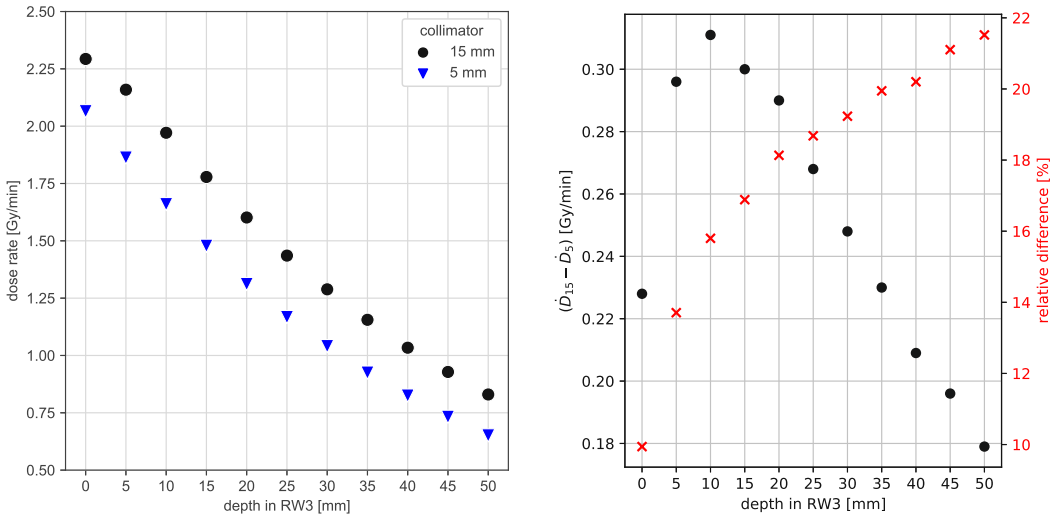

(a) dose rates **(b)** differences between apertures

Figure 5.2.7.: Dose rates measured in RW3 using 5 mm and 15 mm secondary apertures (a) and differences between the secondary apertures (b). An air gap of 50 mm was established between the SC and the first RW3 slab. Relative standard deviations were $\leq 0.25\,\%$.

and 0.06 were found for secondary apertures of 5 mm, 10 mm and 15 mm respectively. In relative terms, the FWHMs for all apertures increased by approximately 27 % from 0–70 mm depth, corresponding to a linear increase of FWHM by 3.9 %/10mm. Comparing the profiles in figure 5.2.8 for the same apertures, larger dose fluctuations were identified in proximity of the surface. This behavior was reflected in terms of the homogeneity indices (HIs), which decreased with increasing depths for all used apertures (table 2.1). The highest HI of 1.12 was found for the 5 mm aperture measured at the surface and reduced to 1.08 at 70 mm depth. Scatter radiation from the SC could be a potential cause of the increased dose fluctuations in the surface region. Furthermore, the amount of material behind the films is not consistent (e.g. 70 mm RW3 slabs behind the first and 3 mm behind the last film), which may result in variable contributions of backscattered radiation. To further investigate this matter, an equivalent measurement with an air gap of 50 mm should be conducted, potentially with additional slabs behind the last film, to account for backscattering. Maximum flatness values of 3.3 % at the surface and 5.1 % at a depth of 70 mm were found (table 2.1). The flatness of all evaluated profiles increased for depths of 70 mm compared to 0 mm.

The LDPs shown in figure 5.2.9 demonstrate a non negligible transmission through the collimation setup, measured directly behind the SC. No transmission was found for lateral positions between −23 mm and 23 mm, indicating that the secondary brass collimator of 46 mm diameter and 20 mm thickness prevents any transmission. Furthermore, this shows that the connection of the SC and the tube successfully prevents any leakage radiation.

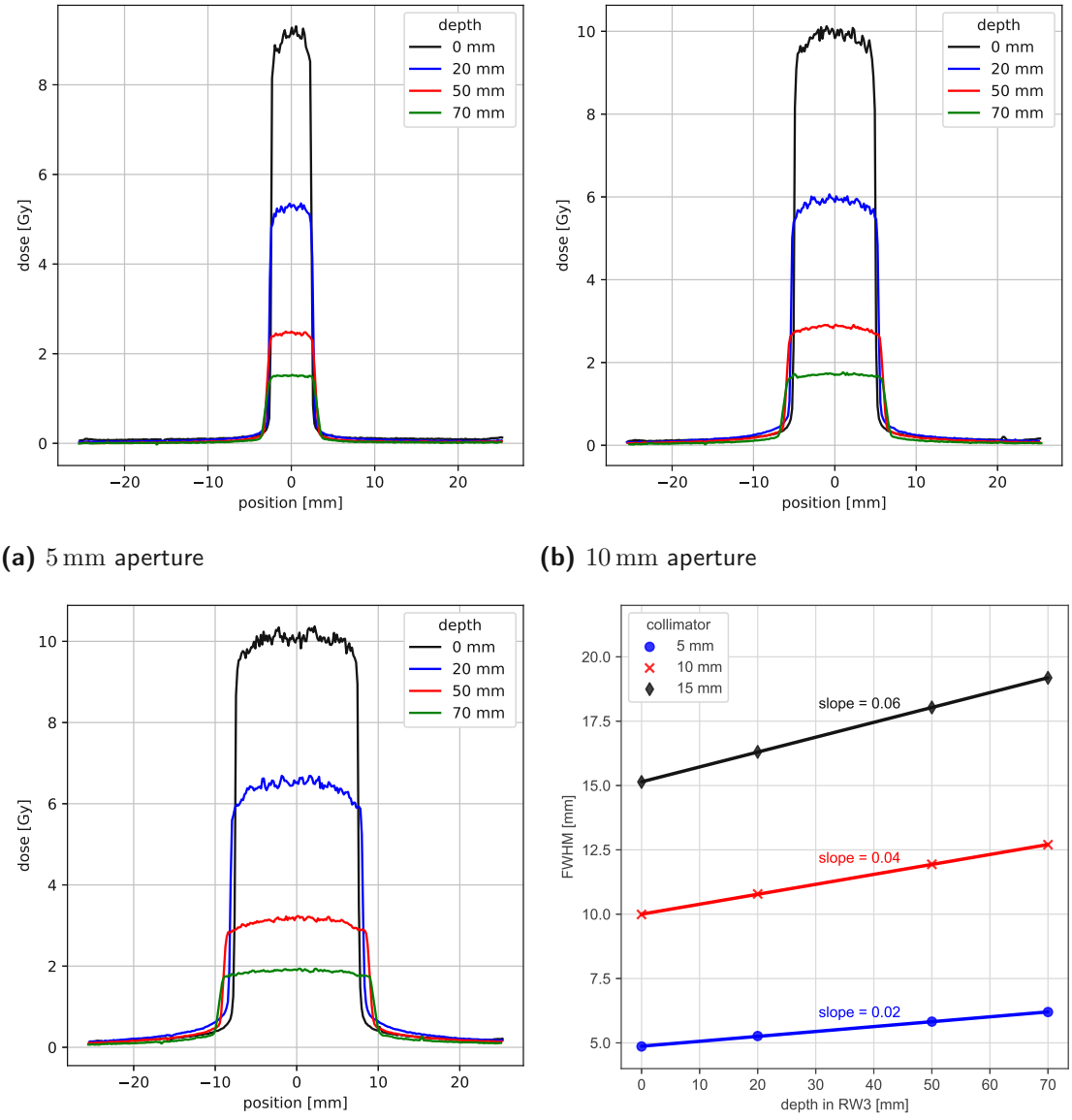

(a) 5 mm aperture

(b) 10 mm aperture

(c) 15 mm aperture

(d) FWHM

Figure 5.2.8.: LDPs with variable apertures at multiple depths of RW3 material for 180 s irradiation time. The FWHM was calculated for all profiles and showed a linear dependence between the slope s and the aperture diameter d as $s = 0.004 * d$ within the investigated range.

Table 2.1.: HI and flatness within the central beam region for all apertures and multiple depths in RW3.

aperture diameter [mm]	depth in RW3 [mm]	flatness [%]	HI [a.u.]
5	0	3,3	1,119
	20	4,4	1,102
	50	2,3	1,082
	70	5,1	1,077
10	0	3,2	1,108
	20	3,8	1,103
	50	3,2	1,090
	70	3,9	1,092
15	0	3,3	1,108
	20	4,7	1,110
	50	4,9	1,102
	70	5,0	1,094

However, the transmission values start increasing just beyond the SC, until the maximum transmission of approximately 5 % occurs at a distance of 50 mm around the central beam axis. For irradiation of mice passing through the snout or eyes, the found transmission may be negligible, as the width of the animals is typically less than that of the SC. However for irradiation from the side, the transmission may lead to significant doses distant from the intended target within the animal. This issue necessitates technical adaption of the collimation setup. A potential origin of the issue may be transmission through the tube, close to the PC.

It should be noted that a dose of 33 Gy, as found for the film investigated in figure 5.2.9b, exceeds the recommended dose range of EBT3 films. Nevertheless the results of both films agreed within 1 % in terms of the resulting dose rate, indicating that EBT3 films are still viable in this dose range for 200 keV X-rays.

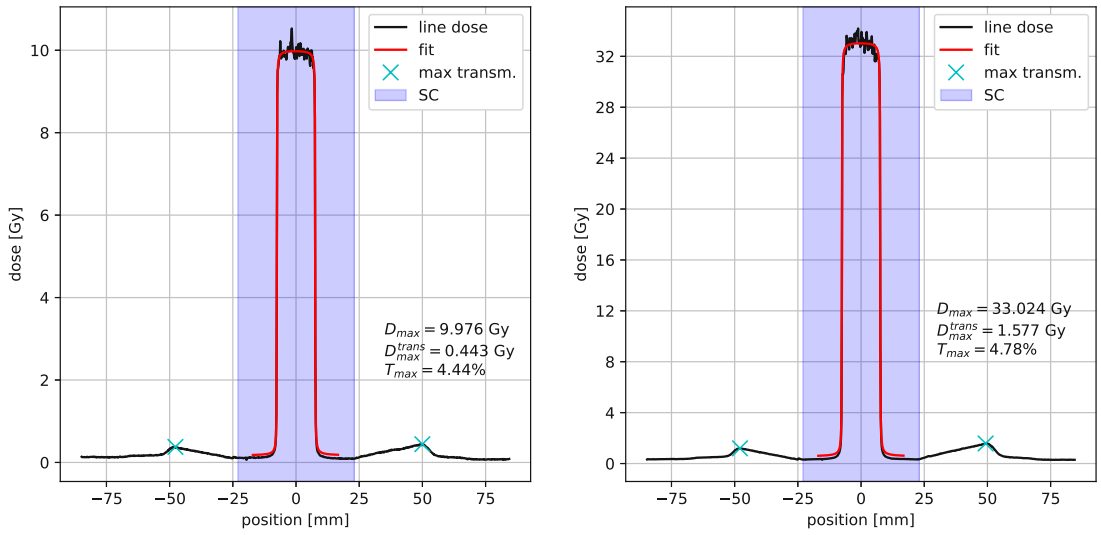

(a) 180 s irradiation time

(b) 600 s irradiation time

Figure 5.2.9.: LDPs for determination of transmission and leakage after 180 s and 600 s irradiation time. A transmission of approximately 5 % was found at a distance of 50 mm around the central beam axis. The size of the secondary collimator (SC) is indicated in blue.

6. Conclusion and Outlook

A small field dosimetry phantom (SFDP) for X-ray as well as ion beams and an X-ray collimation system were developed in the frame of this thesis.

The suitability of the designed SFDP in combination with water-equivalent RW3 slabs for dosimetric measurements with different detectors and EBT3 films in proton and photon beams could be shown by measurements. Thus a convenient substitute for commercially available water and water-equivalent phantoms for small field dosimetry could be presented.

Prior to the design of the final X-ray collimation system, essential insight was gained from the dosimetric evaluation of the constructed prototype setup. Based on the dosimetric parameters acquired with the prototype setup, the final system was manufactured from brass employing a 20 mm thick primary collimator and a 140 mm long tube, in order to reduce scatter radiation and to mount interchangeable, 20 mm thick secondary collimators. The established setup provides the possibility to irradiate variable small field sizes for pre-clinical in-vivo experiments and for dosimetric investigations employing dedicated phantoms. Depth dose curves, dose rates and lateral dose profiles for the collimation system were measured using the small field dosimetry phantom and laid a first basis for the creation of a beam model within the treatment planning system (TPS) µ-RayStation (RaySearch Laboratories, Stockholm, Sweden). The evaluated data showed that the collimation system provides dose rates of approximately 2.6 Gy min^{-1} at a distance of 30 mm of the secondary collimator, using a 15 mm aperture in 200 keV X-ray beams.

Due to varying measurement geometries and X-ray tube configurations, a direct comparison to commercially available systems can not be drawn. However, reported therapeutic dose rates for commercial devices are mostly in the region of 1–3 Gy min^{-1} [85, 87–90], with maximal achievable dose rates of 4 Gy min^{-1} [33]. Thus, sufficient dose rates for small animal irradiation, comparable to those of commercially available systems were obtained with the developed X-ray collimation system. Commercial systems, such as the small animal radiation research platform (SARRP) (Xstrahl Ltd., Camberley, UK), typically employ sophisticated collimators mounted to a gantry, which enables irradiation in arcs around the target. Since the designed X-ray collimation system should mimic the available ion beam irradiation geometry and serve for reference irradiation, a system for horizontal beams was sufficient. Even though the collimation system is simpler as compared to commercial systems, the measured lateral beam profiles exhibit similar characteristics. While measurements at a depth of 0 mm of RW3 (i.e. at the surface) revealed a flatness of 3.2 % and 3.3 % for apertures of 10 mm and 15 mm, respectively, similar results of 3.1 % were reported for the SARRP in a comparable geometry using a 12 mm aperture in a 220 keV X-ray beam [90].

The mounting mechanism of the secondary collimators within the designed setup prevents leakage and transmission radiation in the central region. However, transmission of up to 5 % was found at a distance of 50 mm from the central beam axis, which is most likely a result of divergent radiation transmitted through the collimator tube. Further investigation of the transmission issue regarding its origin, relevance for the irradiation of small animals and potential technical adaptions are necessary and need to be performed in future studies.

A major challenge with the available X-ray irradiation cabinet, as compared to other systems, is accurate positioning. A number of solutions, dedicated to irradiation of small animals, offer image guidance capabilities, which guarantees precise positioning down to the submillimeter scale [60, 85, 91]. To improve and simplify positioning within the available system, a laser alignment system will be added to the interior of the irradiation cabinet. Since the entire experimental setup had to be aligned 'by hand' so far, this upgrade is crucial to reduce potential uncertainties regarding positioning, especially when working with animals.

Furthermore, an optimal arrangement of the X-ray positioning table and couch with respect to the collimation system has to be evaluated, improved and finalised. Additionally, a suitable isocenter has to be defined within the irradiation cabinet. A library of secondary collimators with apertures of different sizes and potentially shapes will be introduced to cover all field sizes and shapes necessary for the first pre-clinical experiments.

When all adaptions are finalised, a beam model for the final X-ray irradiation setup will be created within the TPS. This commissioning process for the TPS comprises aspects as the definition of the irradiation geometry (including collimators), characterization of the output X-ray spectrum, as well as measurements of dose rates, depth dose profiles and lateral dose profiles. Subsequently, dedicated verification measurements have to be conducted, to ensure that the dose distribution simulated by the TPS is in agreement with the deposited physical dose.

Several challenges, especially in the context of alignment in particle beams still remain. The introduced SFDP currently covers various dosimetric aspects. To additionally cover aspects regarding positioning, the SFDP will be complemented by a dedicated insert to verify the alignment between the imaging and irradiation isocenter. This alignment insert will employ steel spheres with a diameter of 2 mm, that obscure small regions of the beam, which can be visualized with radiochromic films inserted into the holder. Combined with a collimator that resembles a crosshair and indicates the center of the passive beam modifier (PBM), accurate alignment of the PBM and the SFDP can be verified by analyzing the irradiated EBT3 films and their resulting coloration pattern. Furthermore, the spheres result in regions of high contrast in 2D or 3D X-ray images generated by the on-board imaging system and will thereby aid X-ray based image registration with digial reconstructed radiograph (DRR) images.

Prior to pre-clinical experiments involving animals, the developed workflow (outlined in section 1.5) needs to undergo rigorous end-to-end testing for photon beam (X-ray), as well as ion beams. Over the course of the end-to-end tests, the entire procedure comprising

imaging, treatment planning and dose delivery has to be assessed with suitable detectors and phantoms, such that precise and reliable irradiation is guaranteed. A special focus will be set on timing and the challenges that come with anaesthesia of the animals.

Once the remaining technical adaptions and end-to-end testing are concluded, first pre-clinical irradiation experiments comparing the effects of reference X-ray beams and proton (or carbon ion) beams can begin. The comparison of effects resulting from beams with low and high ionization densities has the potential to improve our understanding of the underlying radiobiological mechanisms and thus hopefully facilitates advancement in the field of radiation therapy.

A. Small Field Dosimetry Phantom

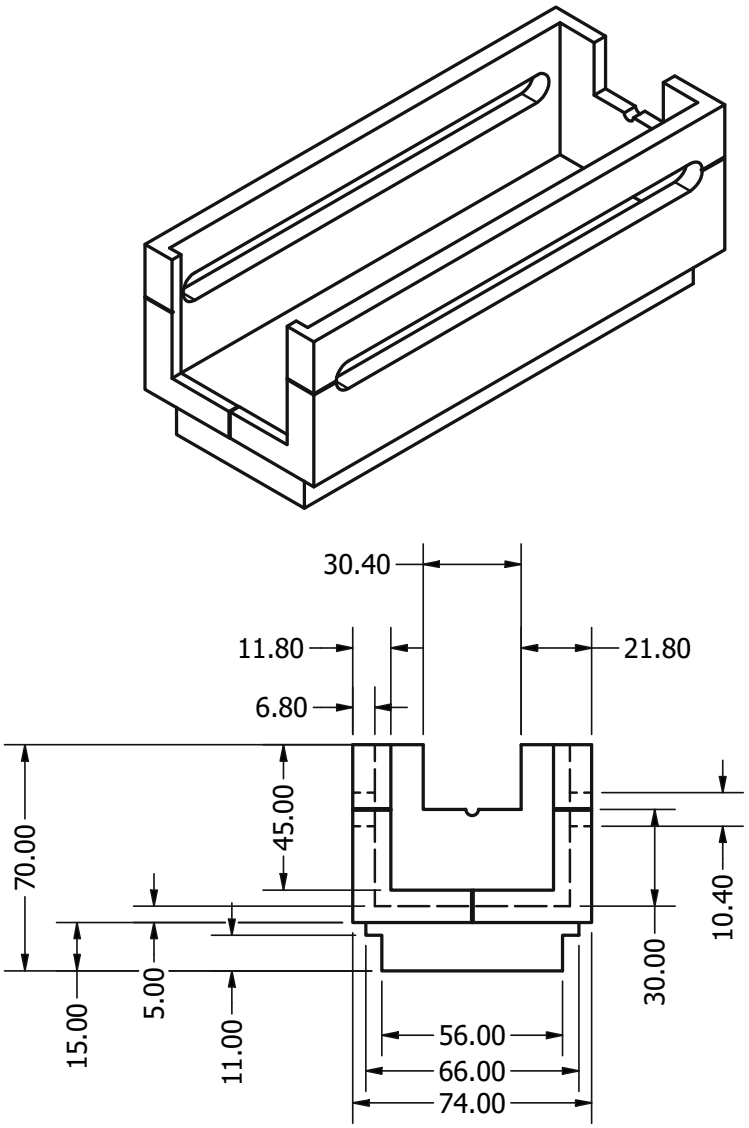

Figure A.0.1.: Phantom front view. Dimensions in mm.

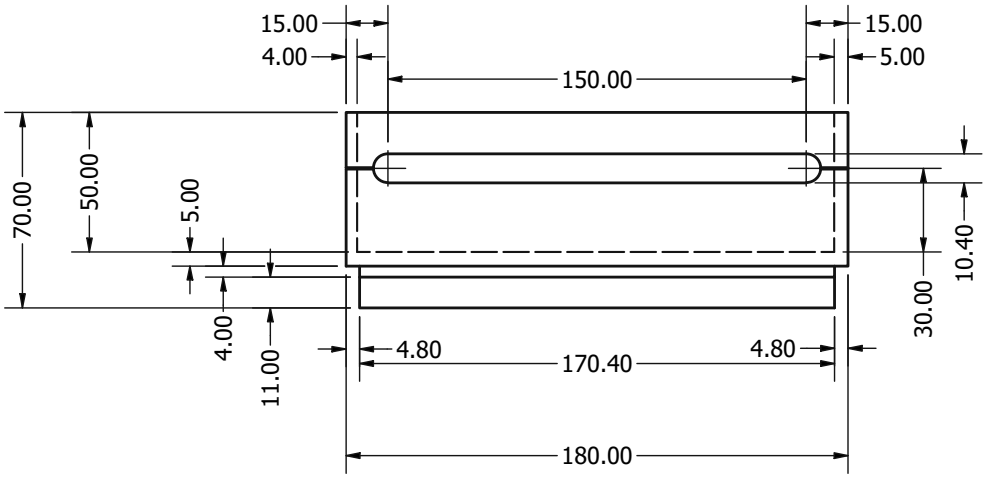

Figure A.0.2.: Phantom side view. Dimensions in mm.

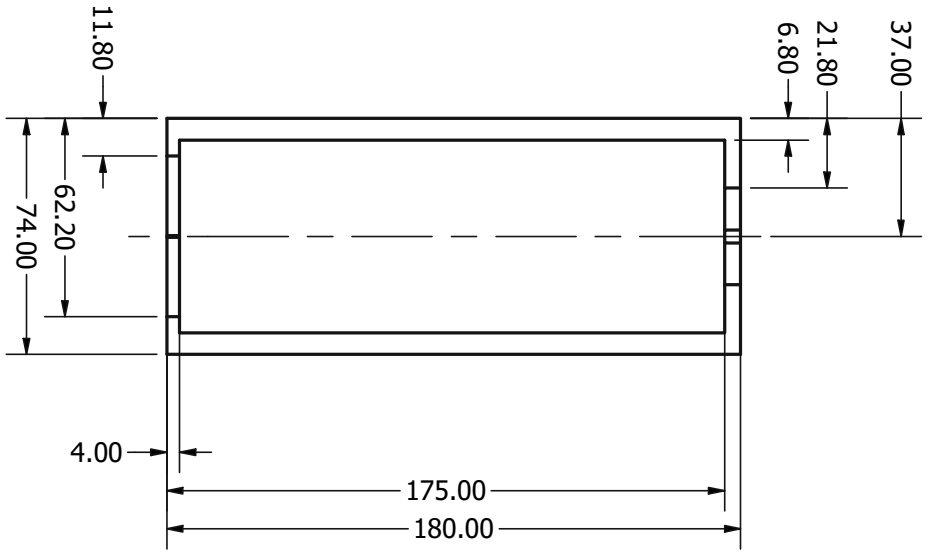

Figure A.0.3.: Phantom top view. Dimensions in mm.

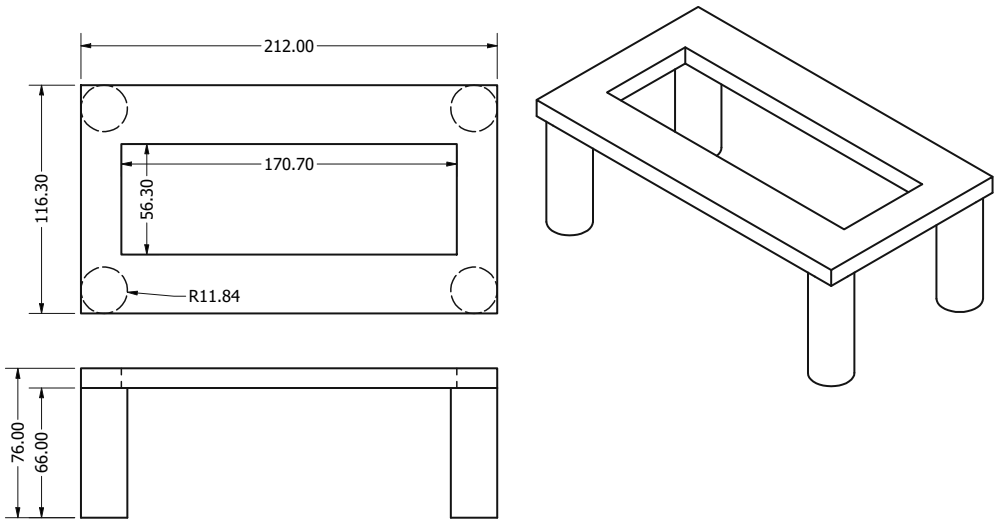

Figure A.0.4.: Pedestal for the SFDP. Dimensions in mm.

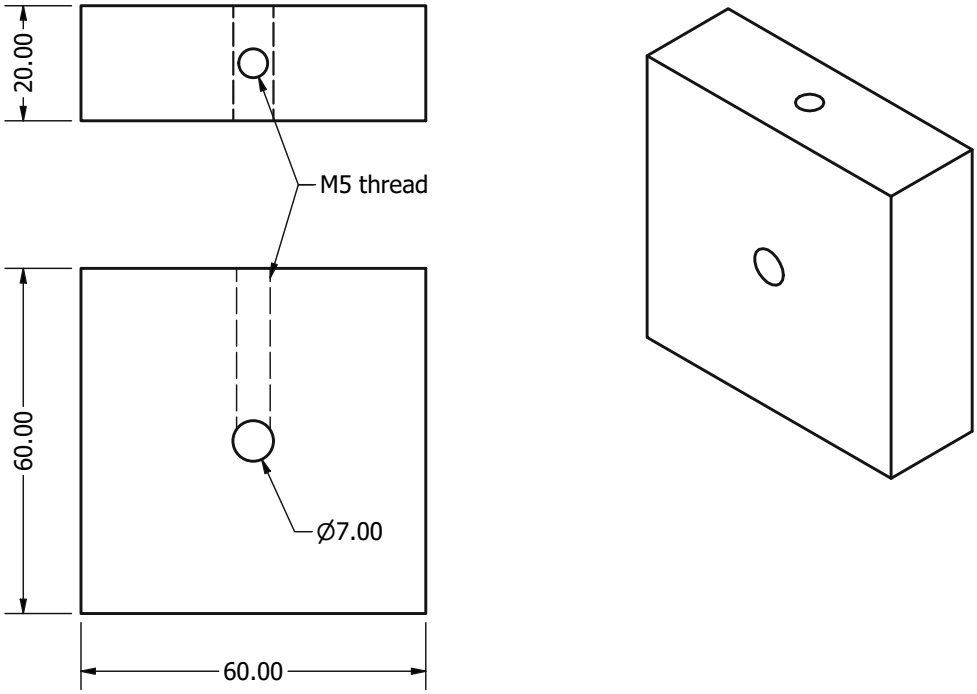

Figure A.0.5.: Holder for the microDiamond detector. A plastic screw can be inserted from the top to fix the detector in the holder. Dimensions in mm.

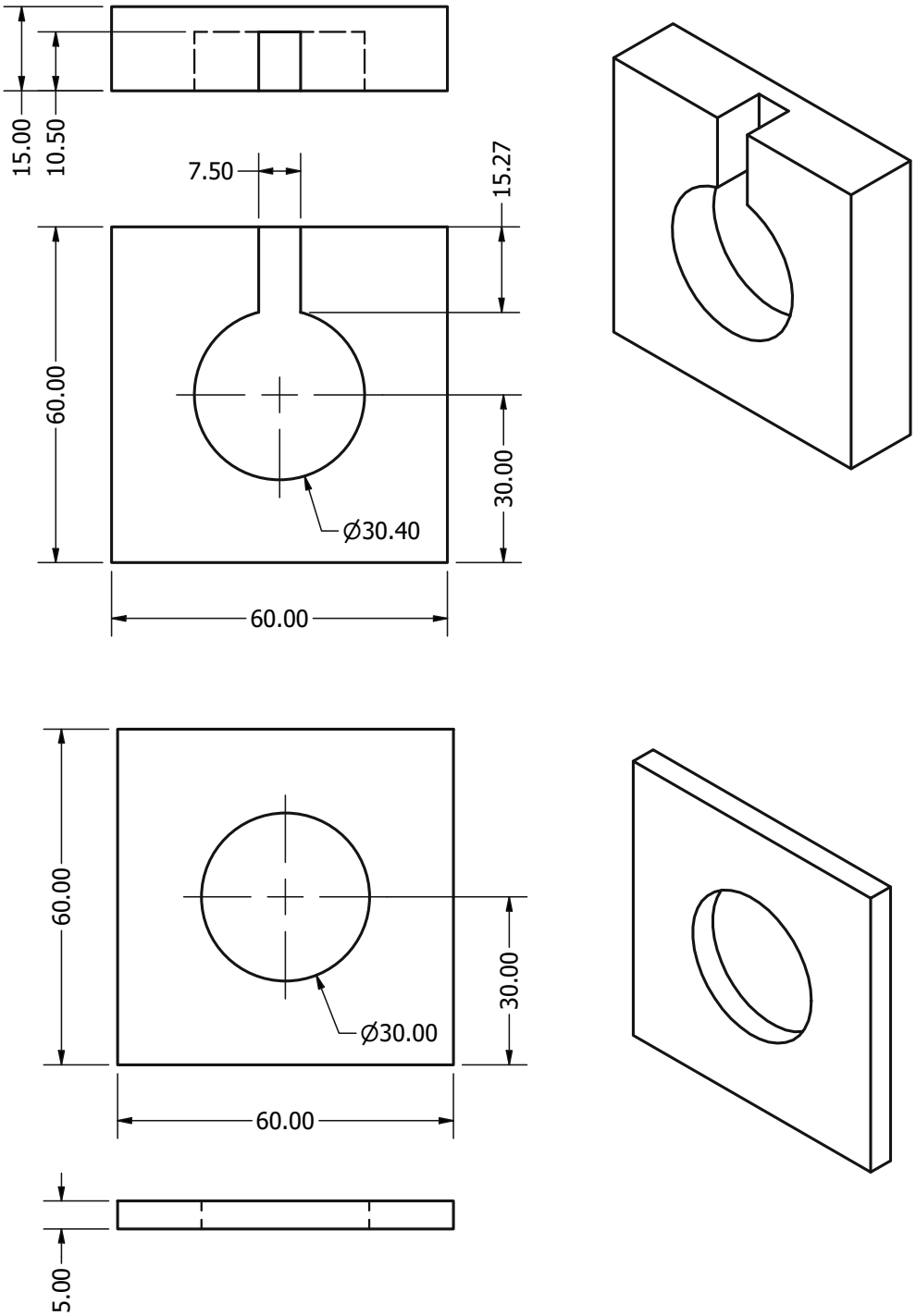

Figure A.0.6.: Holder for the Advanced Markus Chamber. The detector is fixed by 'sandwiching' it between the two slabs. Dimensions in mm.

B. Collimation System

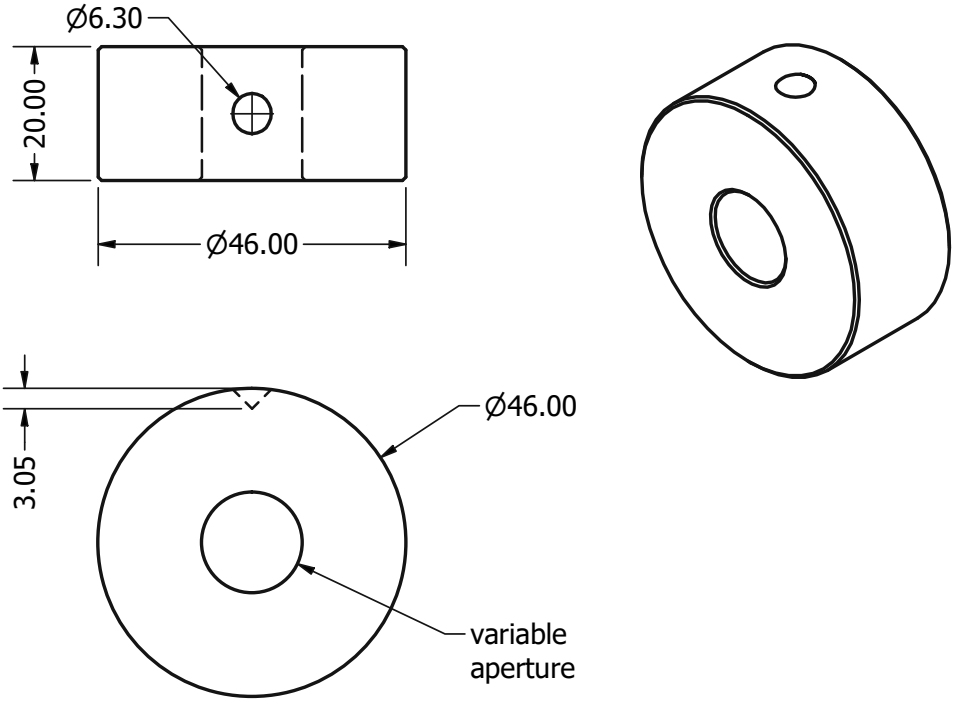

Figure B.0.1.: Secondary collimator. Dimensions in mm.

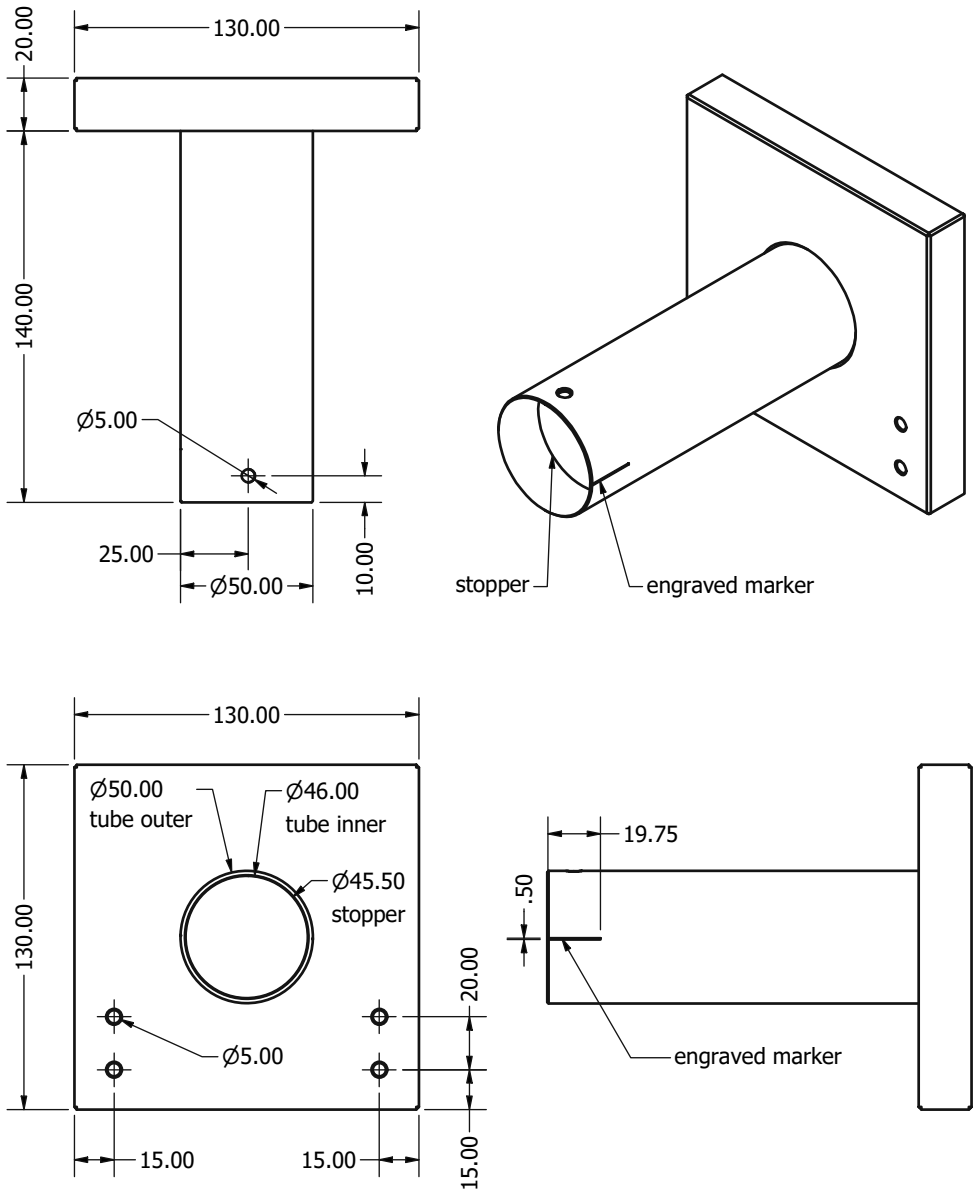

Figure B.0.2.: Primary collimator and tube. Dimensions in mm.

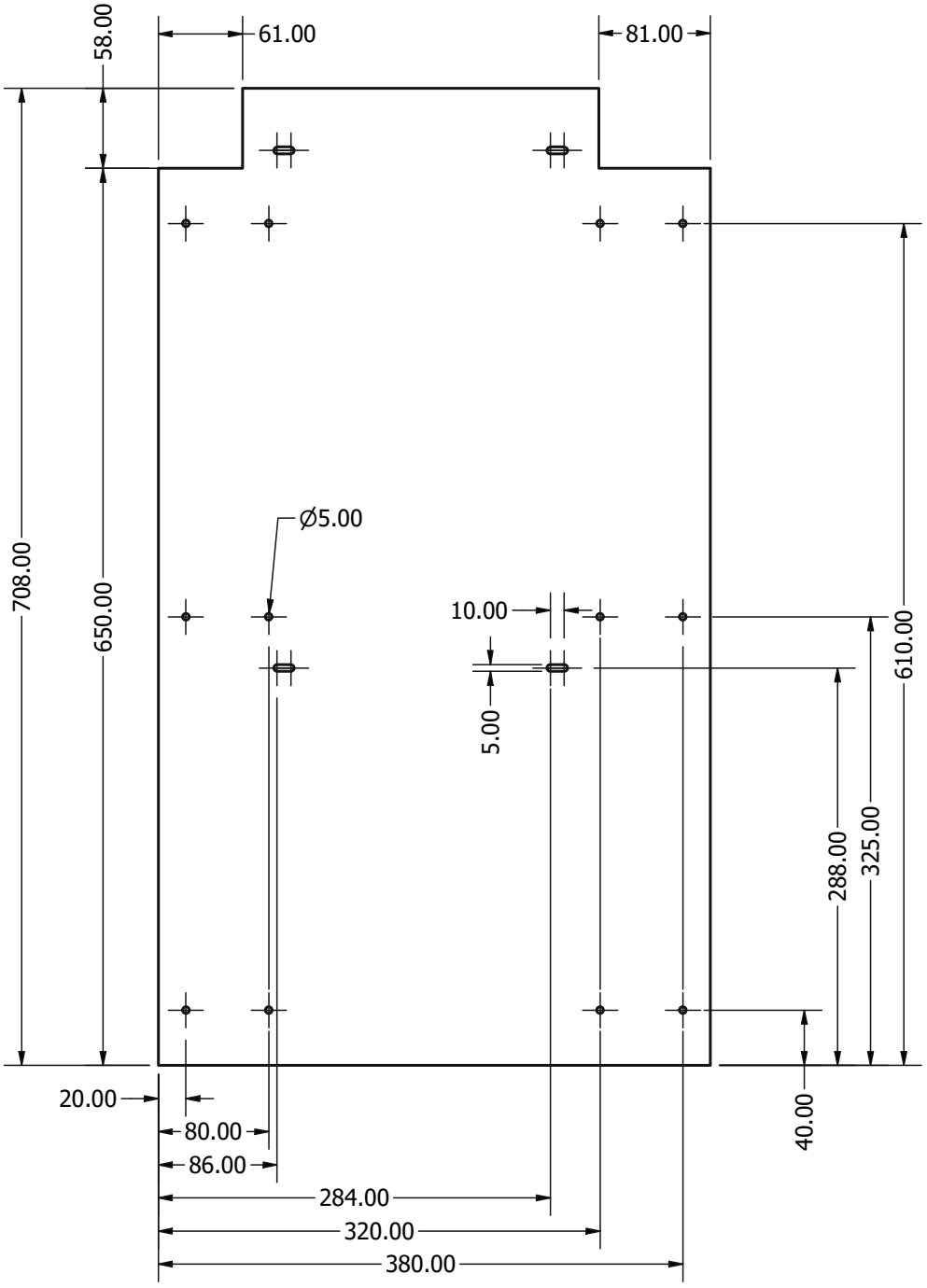

Figure B.0.3.: Top view of base plate to mount collimator setup. Dimensions in mm.

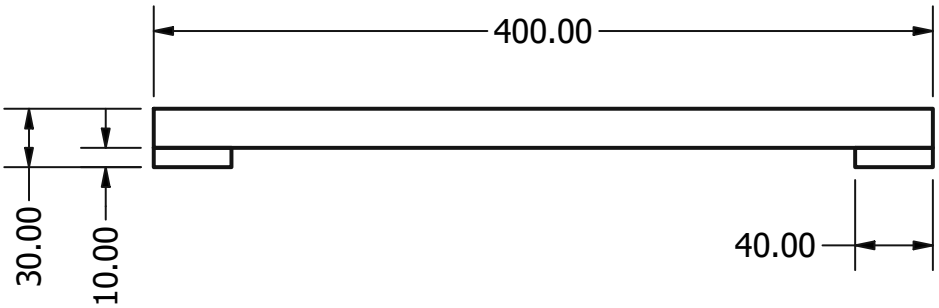

Figure B.0.4.: Rear view of base plate to mount collimator setup. Dimensions in mm.

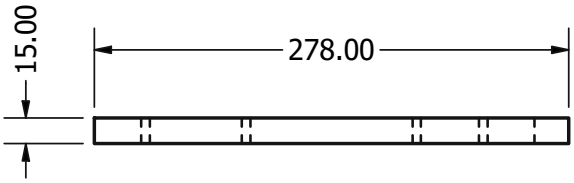

Figure B.0.5.: Rear view of mounting plate for collimator setup. Dimensions in mm.

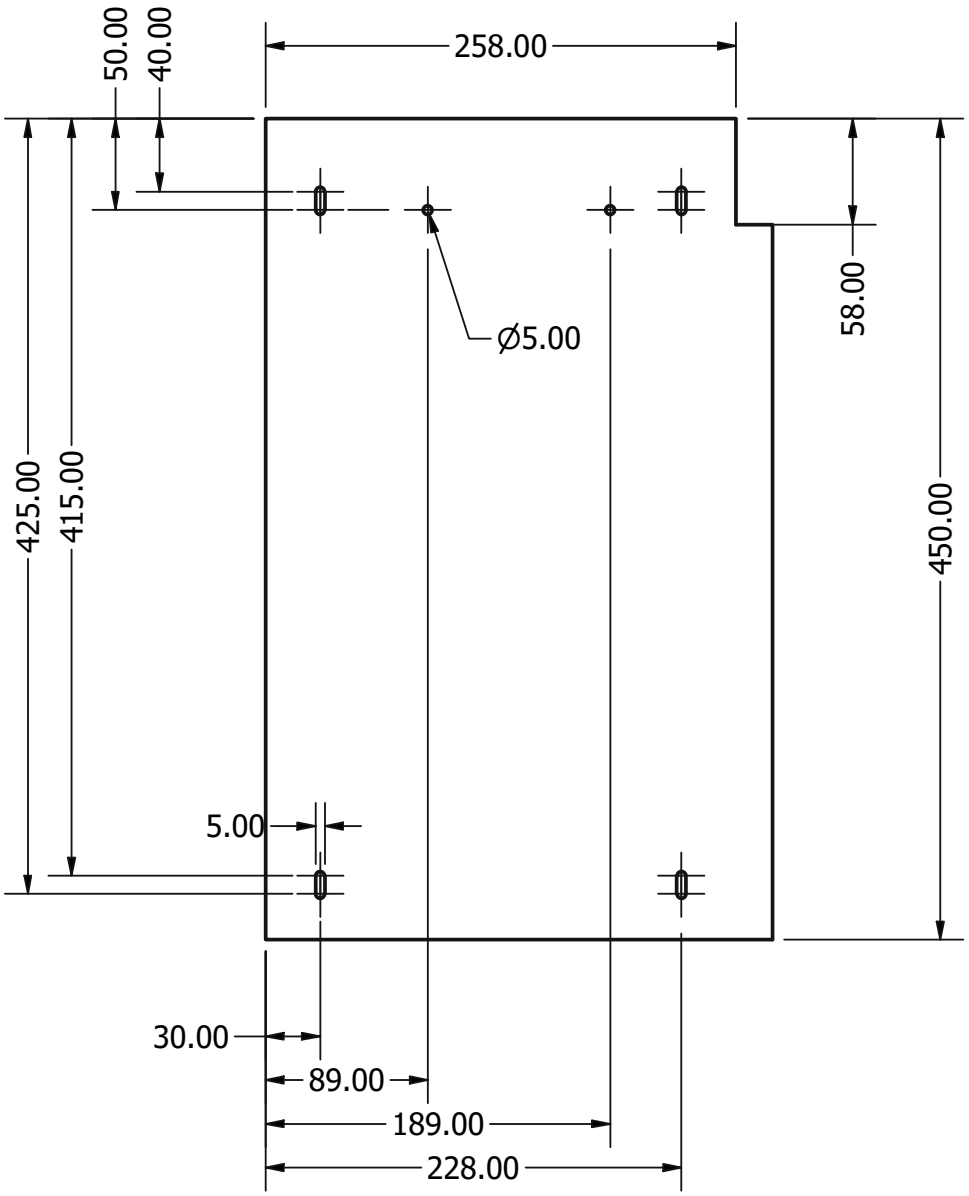

Figure B.0.6.: Top view of mounting plate for collimator setup. Dimensions in mm.

List of Figures

Bibliography

[1] H. Murshed. *Fundamentals of Radiation Oncology: Physical, Biological, and Clinical Aspects*. Academic Press, 2019.

[2] G. A. Roth et al. "Global, Regional, and National Age-Sex-Specific Mortality for 282 Causes of Death in 195 Countries and Territories, 1980–2017: A Systematic Analysis for the Global Burden of Disease Study 2017". In: *The Lancet* 392 (2018), pp. 1736–1788. DOI: 10.1016/S0140-6736(18)32203-7.

[3] H. Ritchie and M. Roser. "Causes of Death". In: *Our World in Data* (2018).

[4] J. Ferlay, M. Colombet, I. Soerjomataram, D. M. Parkin, M. Piñeros, A. Znaor, and F. Bray. "Cancer Statistics for the Year 2020: An Overview". In: *International Journal of Cancer* (2021). DOI: 10.1002/ijc.33588.

[5] H. Sung, J. Ferlay, R. L. Siegel, M. Laversanne, I. Soerjomataram, A. Jemal, and F. Bray. "Global Cancer Statistics 2020: GLOBOCAN Estimates of Incidence and Mortality Worldwide for 36 Cancers in 185 Countries". In: *CA: a cancer journal for clinicians* 71 (2021), pp. 209–249. DOI: 10.3322/caac.21660.

[6] *Cancer Tomorrow: Statistics of the International Agency for Research on Cancer (IARC)*. URL: https://gco.iarc.fr/tomorrow/en (visited on 03/19/2022).

[7] M. Beyzadeoglu, G. Ozyigit, and C. Ebruli. *Basic Radiation Oncology*. Springer Science & Business Media, 2010.

[8] International Atomic Energy Agency. *Radiotherapy in Cancer Care: Facing the Global Challenge*. 2017.

[9] W. C. Roentgen. *Über Eine Neue Art von Strahlen*. Sitzungsbericht der Würzburger Physikalischmedicinischen Gesellschaft. 1895.

[10] W. D. Coolidge. "Cathode-Ray and Roentgen-ray Work in Progress." In: *Am J Roentgenol & Radium Therapy* 19 (1928), pp. 313–321.

[11] E. D. Courant. "Early Milestones in the Evolution of Accelerators". In: *Reviews of Accelerator Science and Technology* 01 (2008), pp. 1–5. DOI: 10.1142/S1793626808000022.

[12] H. Coutard. "PRINCIPLES OF X RAY THERAPY OF MALIGNANT DISEASES". In: *The Lancet* 224 (1934), pp. 5–8. DOI: 10.1016/S0140-6736(00)90085-0.

[13] H. B. Hewitt. "Rationalizing Radiotherapy: Some Historical Aspects of the Endeavour". In: *The British Journal of Radiology* 46 (1973), pp. 917–926. DOI: 10.1259/0007-1285-46-550-917.

[14] E. M. McMillan. "The Origin of the Synchrotron". In: *Physical Review* 69 (1946), pp. 534–534. DOI: 10.1103/PhysRev.69.534.2.

[15] J. Thariat, J.-M. Hannoun-Levi, A. Sun Myint, T. Vuong, and J.-P. Gérard. "Past, Present, and Future of Radiotherapy for the Benefit of Patients". In: *Nature Reviews. Clinical Oncology* 10 (2013), pp. 52–60. DOI: 10.1038/nrclinonc.2012.203.

[16] E. B. Podgorsak. *Radiation Oncology Physics: A Handbook for Teachers and Students*. International Atomic Energy Agency, 2005.

[17] J. E. Tepper. *Gunderson and Tepper's Clinical Radiation Oncology*. Elsevier, 2020.

[18] R. R. Wilson. "Radiological Use of Fast Protons". In: *Radiology* 47 (1946), pp. 487–491. DOI: 10.1148/47.5.487.

[19] J. H. Lawrence, C. A. Tobias, J. L. Born, R. K. McCOMBS, J. E. Roberts, H. O. Anger, B. V. Low-Beer, and C. B. Huggins. "Pituitary Irradiation with High-Energy Proton Beams: A Preliminary Report". In: *Cancer Research* 18 (1958), pp. 121–134.

[20] Y. Matsumoto, N. Fukumitsu, H. Ishikawa, K. Nakai, and H. Sakurai. "A Critical Review of Radiation Therapy: From Particle Beam Therapy (Proton, Carbon, and BNCT) to Beyond". In: *Journal of Personalized Medicine* 11 (2021), p. 825. DOI: 10.3390/jpm11080825.

[21] *PTCOG - Patient Statistics*. URL: https://www.ptcog.ch/index.php/patient-statistics (visited on 03/20/2022).

[22] S. Deycmar, E. Faccin, T. Kazimova, P. A. Knobel, I. Telarovic, F. Tschanz, V. Waller, R. Winkler, C. Yong, D. Zingariello, and M. Pruschy. "The Relative Biological Effectiveness of Proton Irradiation in Dependence of DNA Damage Repair". In: *The British Journal of Radiology* 93 (2020), p. 20190494. DOI: 10.1259/bjr.20190494.

[23] R. Mohan and D. Grosshans. "Proton Therapy - Present and Future". In: *Advanced Drug Delivery Reviews* 109 (2017), pp. 26–44. DOI: 10.1016/j.addr.2016.11.006.

[24] J. S. Loeffler and M. Durante. "Charged Particle Therapy–Optimization, Challenges and Future Directions". In: *Nature Reviews. Clinical Oncology* 10 (2013), pp. 411–424. DOI: 10.1038/nrclinonc.2013.79.

[25] F. J. Vernimmen and K. Rock. "Technological Progress in Radiation Therapy for Brain Tumors". In: *Journal of Cancer Therapy* 5 (1 2013), pp. 38–43. DOI: 10.4236/jct.2014.51005.

[26] W. D. Newhauser and R. Zhang. "The Physics of Proton Therapy". In: *Physics in Medicine and Biology* 60 (2015), R155–R209. DOI: 10.1088/0031-9155/60/8/R155.

[27] T. Suckert, S. Nexhipi, A. Dietrich, R. Koch, L. A. Kunz-Schughart, E. Bahn, and E. Beyreuther. "Models for Translational Proton Radiobiology-From Bench to Bedside and Back". In: *Cancers* 13 (2021), p. 4216. DOI: 10.3390/cancers13164216.

[28] H. Paganetti. "Mechanisms and Review of Clinical Evidence of Variations in Relative Biological Effectiveness in Proton Therapy". In: *International Journal of Radiation Oncology, Biology, Physics* 112 (2022), pp. 222–236. DOI: 10.1016/j.ijrobp.2021.08.015.

[29] C. R. Peeler, D. Mirkovic, U. Titt, P. Blanchard, J. R. Gunther, A. Mahajan, R. Mohan, and D. R. Grosshans. "Clinical Evidence of Variable Proton Biological Effectiveness in Pediatric Patients Treated for Ependymoma". In: *Radiotherapy and Oncology: Journal of the European Society for Therapeutic Radiology and Oncology* 121 (2016), pp. 395–401. DOI: 10.1016/j.radonc.2016.11.001.

[30] M. Durante. "New Challenges in High-Energy Particle Radiobiology". In: *The British Journal of Radiology* 87 (2014), p. 20130626. DOI: 10.1259/bjr.20130626.

[31] J. Eulitz, B. Lutz, P. Wohlfahrt, A. Dutz, W. Enghardt, C. Karpowitz, M. Krause, E. G. C. Troost, and A. Lühr. "A Monte Carlo Based Radiation Response Modelling Framework to Assess Variability of Clinical RBE in Proton Therapy". In: *Physics in Medicine & Biology* 64 (2019), p. 225020. DOI: 10.1088/1361-6560/ab3841.

[32] E. Bahn, J. Bauer, S. Harrabi, K. Herfarth, J. Debus, and M. Alber. "Late Contrast Enhancing Brain Lesions in Proton-Treated Patients With Low-Grade Glioma: Clinical Evidence for Increased Periventricular Sensitivity and Variable RBE". In: *International Journal of Radiation Oncology, Biology, Physics* 107 (2020), pp. 571–578. DOI: 10.1016/j.ijrobp.2020.03.013.

[33] F. Tillner, P. Thute, R. Bütof, M. Krause, and W. Enghardt. "Pre-Clinical Research in Small Animals Using Radiotherapy Technology – a Bidirectional Translational Approach". In: *Zeitschrift für Medizinische Physik* 24 (2014), pp. 335–351. DOI: 10.1016/j.zemedi.2014.07.004.

[34] T. Ogata, T. Teshima, K. Kagawa, Y. Hishikawa, Y. Takahashi, A. Kawaguchi, Y. Suzumoto, K. Nojima, Y. Furusawa, and N. Matsuura. "Particle Irradiation Suppresses Metastatic Potential of Cancer Cells". In: *Cancer Research* 65 (2005), pp. 113–120.

[35] H. J. Lee Jr, J. Zeng, and R. Rengan. "Proton Beam Therapy and Immunotherapy: An Emerging Partnership for Immune Activation in Non-Small Cell Lung Cancer". In: *Translational Lung Cancer Research* 7 (2018).

[36] B. F. Koontz, F. Verhaegen, and D. De Ruysscher. "Tumour and Normal Tissue Radiobiology in Mouse Models: How Close Are Mice to Mini-Humans?" In: *The British Journal of Radiology* 90 (2017), p. 20160441. DOI: 10.1259/bjr.20160441.

[37] T. Suckert, J. Müller, E. Beyreuther, B. Azadegan, A. Brüggemann, R. Bütof, A. Dietrich, M. Gotz, R. Haase, M. Schürer, F. Tillner, C. von Neubeck, M. Krause, and A. Lühr. "High-Precision Image-Guided Proton Irradiation of Mouse Brain Sub-Volumes". In: *Radiotherapy and Oncology: Journal of the European Society for Therapeutic Radiology and Oncology* 146 (2020), pp. 205–212. DOI: 10.1016/j.radonc.2020.02.023.

[38] F. Verhaegen, P. Granton, and E. Tryggestad. "Small Animal Radiotherapy Research Platforms". In: *Physics in Medicine and Biology* 56 (2011), R55–83. DOI: 10.1088/0031-9155/56/12/R01.

[39] K. Parodi, W. Assmann, C. Belka, J. Bortfeldt, D.-A. Clevert, G. Dedes, R. Kalunga, S. Kundel, N. Kurichiyanil, P. Lämmer, J. Lascaud, K. Lauber, G. Lovatti, S. Meyer, M. Nitta, M. Pinto, M. J. Safari, K. Schnürle, J. Schreiber, P. G. Thirolf, H.-P. Wieser, and M. Würl. "Towards a Novel Small Animal Proton Irradiation Platform: The SIRMIO Project". In: *Acta Oncologica (Stockholm, Sweden)* 58 (2019), pp. 1470–1475. DOI: 10.1080/0284186X.2019.1630752.

[40] M. Stock, D. Georg, A. Ableitinger, A. Zechner, A. Utz, M. Mumot, G. Kragl, J. Hopfgartner, J. Gora, T. Böhlen, L. Grevillot, P. Kuess, P. Steininger, H. Deutschmann, and S. Vatnitsky. "The Technological Basis for Adaptive Ion Beam Therapy at MedAustron: Status and Outlook". In: *Zeitschrift für Medizinische Physik* 28 (2018), pp. 196–210. DOI: 10.1016/j.zemedi.2017.09.007.

[41] R. Schöfbeck. "Couch and Table Design for High-Precision x-Ray Irradiations". Project Thesis. Vienna University of Technology, 2021.

[42] E. B. Podgorsak. *Radiation Physics for Medical Physicists*. Springer Science & Business Media, 2010.

[43] S. Gruber, K. Frings, P. Kuess, and W. Dörr. "Protective Effects of Systemic Dermatan Sulfate Treatment in a Preclinical Model of Radiation-Induced Oral Mucositis". In: *Strahlentherapie Und Onkologie* 194 (2018), pp. 675–685. DOI: 10.1007/s00066-018-1280-8.

[44] P. Kuess, E. Bozsaky, J. Hopfgartner, G. Seifritz, W. Dörr, and D. Georg. "Dosimetric Challenges of Small Animal Irradiation with a Commercial X-ray Unit". In: *Zeitschrift Fur Medizinische Physik* 24 (2014), pp. 363–372. DOI: 10.1016/j.zemedi.2014.08.005.

[45] E. Mara, M. Clausen, S. Khachonkham, S. Deycmar, C. Pessy, W. Dörr, P. Kuess, D. Georg, and S. Gruber. "Investigating the Impact of Alpha/Beta and LETd on Relative Biological Effectiveness in Scanned Proton Beams: An in Vitro Study Based on Human Cell Lines". In: *Medical Physics* 47 (2020), pp. 3691–3702. DOI: 10.1002/mp.14212.

[46] P. Mayles, A. E. Nahum, and J.-C. Rosenwald. *Handbook of Radiotherapy Physics: Theory and Practice*. Taylor & Francis, 2007.

[47] *Radiation Biology: A Handbook for Teachers and Students*. Training Course Series. Vienna: INTERNATIONAL ATOMIC ENERGY AGENCY, 2010.

[48] N. Bohr. "II. *On the Theory of the Decrease of Velocity of Moving Electrified Particles on Passing through Matter*". In: *The London, Edinburgh, and Dublin Philosophical Magazine and Journal of Science* 25 (1913), pp. 10–31. DOI: 10.1080/14786440108634305.

[49] H. Bethe. "Zur Theorie des Durchgangs schneller Korpuskularstrahlen durch Materie". In: *Annalen der Physik* 397 (1930), pp. 325–400. DOI: 10.1002/andp.19303970303.

[50] F. Bloch. "Zur Bremsung rasch bewegter Teilchen beim Durchgang durch Materie". In: *Annalen der Physik* 408 (1933), pp. 285–320. DOI: 10.1002/andp.19334080303.

[51] M. Durante and H. Paganetti. "Nuclear Physics in Particle Therapy: A Review". In: *Reports on Progress in Physics* 79 (2016), p. 096702. DOI: 10.1088/0034-4885/79/9/096702.

[52] *Absorbed Dose Determination in External Beam Radiotherapy: An International Code of Practice for Dosimetry Based on Standards of Absorbed Dose to Water*. International Atomic Energy Agency, 2000.

[53] L. Lindborg and A. Waker. *Microdosimetry: Experimental Methods and Applications*. CRC Press, 2017.

[54] H. Paganetti. "Relative Biological Effectiveness (RBE) Values for Proton Beam Therapy. Variations as a Function of Biological Endpoint, Dose, and Linear Energy Transfer". In: *Physics in Medicine and Biology* 59 (2014), R419–472. DOI: 10.1088/0031-9155/59/22/R419.

[55] H. Paganetti, E. Blakely, A. Carabe-Fernandez, D. J. Carlson, I. J. Das, L. Dong, D. Grosshans, K. D. Held, R. Mohan, V. Moiseenko, A. Niemierko, R. D. Stewart, and H. Willers. "Report of the AAPM TG-256 on the Relative Biological Effectiveness of Proton Beams in Radiation Therapy". In: *Medical Physics* 46 (2019), e53–e78. DOI: 10.1002/mp.13390.

[56] A. Darafsheh. *Radiation Therapy Dosimetry: A Practical Handbook*. CRC Press, 2021.

[57] M. G. Stabin. *Radiation Protection and Dosimetry: An Introduction to Health Physics*. Springer Science & Business Media, 2007.

[58] S. Devic. "Radiochromic Film Dosimetry: Past, Present, and Future". In: *Physica Medica* 27 (2011), pp. 122–134. DOI: 10.1016/j.ejmp.2010.10.001.

[59] E. Y. León-Marroquín, D. J. Mulrow, R. Khan, and A. Darafsheh. "Spectral Analysis of the EBT3 Radiochromic Films for Clinical Photon and Electron Beams". In: *Medical Physics* 46 (2019), pp. 973–982. DOI: 10.1002/mp.13330.

[60] J. Wong, E. Armour, P. Kazanzides, I. Iordachita, E. Tryggestad, H. Deng, M. Matinfar, C. Kennedy, Z. Liu, T. Chan, O. Gray, F. Verhaegen, T. McNutt, E. Ford, and T. L. DeWeese. "A High Resolution Small Animal Radiation Research Platform (SARRP) with x-Ray Tomographic Guidance Capabilities". In: *International journal of radiation oncology, biology, physics* 71 (2008), pp. 1591–1599. DOI: 10.1016/j.ijrobp.2008.04.025.

[61] A. F. Resch, P. D. Heyes, H. Fuchs, N. Bassler, D. Georg, and H. Palmans. "Dose- Rather than Fluence-averaged LET Should Be Used as a Single-parameter Descriptor of Proton Beam Quality for Radiochromic Film Dosimetry". In: *Medical Physics* 47 (2020), pp. 2289–2299. DOI: 10.1002/mp.14097.

[62] S. Devic, J. Seuntjens, E. Sham, E. B. Podgorsak, C. R. Schmidtlein, A. S. Kirov, and C. G. Soares. "Precise Radiochromic Film Dosimetry Using a Flat-Bed Document Scanner". In: *Medical Physics* 32 (2005), pp. 2245–2253. DOI: 10.1118/1.1929253.

[63] S. Devic, N. Tomic, and D. Lewis. "Reference Radiochromic Film Dosimetry: Review of Technical Aspects". In: *Physica medica* 32 (2016), pp. 541–556. DOI: 10.1016/j.ejmp.2016.02.008.

[64] R. Behling. *Modern Diagnostic X-Ray Sources: Technology, Manufacturing, Reliability*. CRC Press, 2015. DOI: 10.1201/b18655.

[65] *Diagnostic Radiology Physics*. Non-Serial Publications. Vienna: International Atomic Energy Agency, 2014.

[66] U. Linz. *Ion Beam Therapy: Fundamentals, Technology, Clinical Applications*. Springer Science & Business Media, 2011.

[67] H. Paganetti. *Proton Therapy Physics, Second Edition*. CRC Press, 2018.

[68] A. W. Chao and K. H. Mess. *Handbook of Accelerator Physics and Engineering*. World Scientific, 2013.

[69] M. Durante and J. S. Loeffler. "Charged Particles in Radiation Oncology". In: *Nature Reviews. Clinical Oncology* 7 (2010), pp. 37–43. DOI: 10.1038/nrclinonc.2009.183.

[70] M. Kowaliuk, E. Bozsaky, S. Gruber, P. Kuess, and W. Dörr. "Systemic Administration of Heparin Ameliorates Radiation-Induced Oral Mucositis—Preclinical Studies in Mice". In: *Strahlentherapie Und Onkologie* 194 (2018), pp. 686–692. DOI: 10.1007/s00066-018-1300-8.

[71] J. Kowaliuk, S. Sarsarshahi, J. Hlawatsch, A. Kastsova, M. Kowaliuk, A. Krischak, P. Kuess, L. Duong, and W. Dörr. "Translational Aspects of Nuclear Factor-Kappa B and Its Modulation by Thalidomide on Early and Late Radiation Sequelae in Urinary Bladder Dysfunction". In: *International Journal of Radiation Oncology, Biology, Physics* 107 (2020), pp. 377–385. DOI: 10.1016/j.ijrobp.2020.01.028.

[72] S. Sarsarshahi, Z. Madjd, E. Bozsaky, J. Kowaliuk, P. Kuess, M. H. Ghahremani, and W. Doerr. "An Evaluation of the Effect of Bortezomib on Radiation-Induced Urinary Bladder Dysfunction". In: *Strahlentherapie Und Onkologie: Organ Der Deutschen Rontgengesellschaft ... [et Al]* 195 (2019), pp. 934–939. DOI: 10.1007/s00066-019-01497-8.

[73] G. G. Poludniowski and P. M. Evans. "Calculation of X-Ray Spectra Emerging from an x-Ray Tube. Part I. Electron Penetration Characteristics in x-Ray Targets". In: *Medical Physics* 34 (2007), pp. 2164–2174. DOI: 10.1118/1.2734725.

[74] G. G. Poludniowski. "Calculation of X-Ray Spectra Emerging from an x-Ray Tube. Part II. X-ray Production and Filtration in x-Ray Targets". In: *Medical Physics* 34 (2007), pp. 2175–2186. DOI: 10.1118/1.2734726.

[75] G. Poludniowski, G. Landry, F. DeBlois, P. M. Evans, and F. Verhaegen. "SpekCalc: A Program to Calculate Photon Spectra from Tungsten Anode x-Ray Tubes". In: *Physics in Medicine and Biology* 54 (2009), N433–438. DOI: 10.1088/0031-9155/54/19/N01.

[76] *National Institute of Standards and Technology (NIST): X-ray Transition Energies for Tungsten*. URL: https://physics.nist.gov/cgi-bin/XrayTrans/search.pl?element=W&trans=All&lower=50000&upper=80000&units=eV (visited on 01/17/2022).

[77] PTW-Freiburg. *User Manual microDiamond Type 60019*. 2013.

[78] PTW-Freiburg. *User Manual Advanced Markus Chamber Ionization Chamber Type 34045*. 2013.

[79] A. Niroomand-Rad, S.-T. Chiu-Tsao, M. P. Grams, D. F. Lewis, C. G. Soares, L. J. Van Battum, I. J. Das, S. Trichter, M. W. Kissick, G. Massillon-JL, P. E. Alvarez, and M. F. Chan. "Report of AAPM Task Group 235 Radiochromic Film Dosimetry: An Update to TG-55". In: *Medical Physics* 47 (2020), pp. 5986–6025. DOI: 10.1002/mp.14497.

[80] L. Langgartner. "Calibration of GafChromic EBT3 Radiochromic Films for Medium Energy X-rays". Project Thesis. Vienna University of Technology, 2022.

[81] R. Dreindl, D. Georg, and M. Stock. "Radiochromic Film Dosimetry: Considerations on Precision and Accuracy for EBT2 and EBT3 Type Films". In: *Zeitschrift Fur Medizinische Physik* 24 (2014), pp. 153–163. DOI: 10.1016/j.zemedi.2013.08.002.

[82] G. Van Rossum and F. L. Drake. *Python 3 Reference Manual*. Scotts Valley, CA: CreateSpace, 2009.

[83] S. Khachonkham, R. Dreindl, G. Heilemann, W. Lechner, H. Fuchs, H. Palmans, D. Georg, and P. Kuess. "Characteristic of EBT-XD and EBT3 Radiochromic Film Dosimetry for Photon and Proton Beams". In: *Physics in Medicine and Biology* 63 (2018), p. 065007. DOI: 10.1088/1361-6560/aab1ee.

[84] T. Kataria, K. Sharma, V. Subramani, K. P. Karrthick, and S. S. Bisht. "Homogeneity Index: An Objective Tool for Assessment of Conformal Radiation Treatments". In: *Journal of Medical Physics* 37 (2012), pp. 207–213. DOI: 10.4103/0971-6203.103606.

[85] R. Clarkson, P. E. Lindsay, S. Ansell, G. Wilson, S. Jelveh, R. P. Hill, and D. A. Jaffray. "Characterization of Image Quality and Image-Guidance Performance of a Preclinical Microirradiator". In: *Medical Physics* 38 (2011), pp. 845–856. DOI: 10.1118/1.3533947.

[86] M. Newville, R. Otten, A. Nelson, A. Ingargiola, T. Stensitzki, D. Allan, A. Fox, F. Carter, Michał, R. Osborn, D. Pustakhod, lneuhaus, S. Weigand, Glenn, C. Deil, Mark, A. L. R. Hansen, G. Pasquevich, L. Foks, N. Zobrist, O. Frost, A. Beelen, Stuermer, azelcer, A. Hannum, A. Polloreno, J. H. Nielsen, S. Caldwell, A. Almarza, and A. Persaud. *LMFIT: Non-Linear Least-Square Minimization and Curve-Fitting for Python (1.0.3)*. Zenodo, 2021. DOI: 10.5281/zenodo.5570790.

[87] M. Ghita, S. J. McMahon, H. F. Thompson, C. K. McGarry, R. King, S. O. S. Osman, J. L. Kane, A. Tulk, G. Schettino, K. T. Butterworth, A. R. Hounsell, and K. M. Prise. "Small Field Dosimetry for the Small Animal Radiotherapy Research Platform (SARRP)". In: *Radiation Oncology* 12 (2017), p. 204. DOI: 10.1186/s13014-017-0936-3.

[88] Y. He, Y. Peng, Y. Chang, J. Zhu, Z. Li, K. Huang, and S. Pan. "Utilizing the Faxitron MultiRad 225 X-ray Irradiation System for the Construction of Mouse Chronic Whole Brain Radiation Model". In: *Journal of Radiation Research* 62 (2021), pp. 966–975. DOI: 10.1093/jrr/rrab086.

[89] E. Tryggestad, M. Armour, I. Iordachita, F. Verhaegen, and J. W. Wong. "A Comprehensive System for Dosimetric Commissioning and Monte Carlo Validation for the Small Animal Radiation Research Platform". In: *Physics in Medicine and Biology* 54 (2009), pp. 5341–5357. DOI: 10.1088/0031-9155/54/17/017.

[90] M. Jermoumi, H. Korideck, M. Bhagwat, P. Zygmanski, G. Makrigiogos, R. Berbeco, R. Cormack, and W. Ngwa. "Comprehensive Quality Assurance Phantom for the Small Animal Radiation Research Platform (SARRP)". In: *Physica medica* 31 (2015), pp. 529–535. DOI: 10.1016/j.ejmp.2015.04.010.

[91] R. Pidikiti, S. Stojadinovic, M. Speiser, K. H. Song, F. Hager, D. Saha, and T. D. Solberg. "Dosimetric Characterization of an Image-Guided Stereotactic Small Animal Irradiator". In: *Physics in Medicine and Biology* 56 (2011), pp. 2585–2599. DOI: 10.1088/0031-9155/56/8/016.

Abbreviations

AAPM American Association of Physicists in Medicine.

ABS acrylonitrile butadiene styrene.

CAD computer-aided design.

CSDA continuous slowing down approximation.

CT computed tomography.

DDP depth dose profile.

DRR digial reconstructed radiograph.

DVH dose volume histogram.

EBRT External Beam Radiotherapy.

FWHM full width at half maximum.

HI homogeneity index.

HVL half value layer.

IAEA International Atomic Energy Agency.

IBT ion beam therapy.

IGRT image guided radiation therapy.

IMRT intensity modulated radiation therapy.

IR irradiation room.

LDP lateral dose profile.

LEM local effect model.

LET linear energy transfer.

LQM linear-quadratic model.

MedAustron MedAustron Ion Therapy Center.

MKM microdosimetric-kinetic model.

MRI magnetic resonance imaging.

OAR organ at risk.

PBM passive beam modifier.

PC primary collimator.

PET positron emission tomography.

PTCOG Particle Therapy Co-Operative Group.

PV pixel value.

RBE relative radiobiological effectiveness.

ROI region of interest.

RT radiation therapy.

SARRP small animal radiation research platform.

SC secondary collimator.

SFDP small field dosimetry phantom.

SOBP spread-out Bragg peak.

SPECT single-photon emission computed tomography.

TPS treatment planning system.

WED water equivalent depth.

X-ray photon beam.